UNIVERSITÀ
DEGLI STUDI
DI PADOVA

Sede amministrativa: Università degli Studi di Padova

Dipartimento di Fisica e Astronomia "Galileo Galilei"

SCUOLA DI DOTTORATO DI RICERCA IN FISICA
INDIRIZZO ASTROFISICO TEORICO
CICLO XXVIII

POLARIZED EMISSION FROM HIGHLY-MAGNETIZED NEUTRON STARS

Direttore della scuola : Ch.mo Prof. Andrea Vitturi
Supervisore : Ch.mo Prof. Roberto Turolla

Dottorando : Roberto Taverna

Abstract

The study of magnetars, the anomalous X-ray pulsars (AXPs) and the soft gamma repeaters (SGRs), and of X-ray Dim Isolated Neutron Stars (XDINSs) is of particular relevance, since these objects exhibit the strongest magnetic fields ever observed in the universe ($10^{13} - 10^{15}$ G) and represent the only laboratories where physics in the presence of such strong magnetic fields can be tested. Until now, these peculiar neutron stars have been investigated through spectroscopic and timing measurements, which led to validate the theoretical models developed to explain their phenomenology, as in the case of the "twisted magnetosphere" model for magnetars or the different surface emission models for XDINSs. Nevertheless, this kind of analysis alone is far from providing complete information. In this respect, X-ray polarimetry may disclose an entirely new approach in the study of highly magnetized neutron stars. Radiation emitted in the presence of strong magnetic fields, in fact, is expected to be highly polarized; polarization measurements provide two additional observables, the linear polarization fraction and the polarization angle, that can unambiguously determine the model parameters also when spectral analysis alone fails. The polarization signal that an observer at infinity would collect, however, do not necessary coincide with model predictions for the polarization at the surface, due to the effects of quantum electrodynamics in the highly magnetized vacuum around the star, coupled with the rotation of the Stokes parameters in the plane perpendicular to the line of sight, induced by the non-uniform magnetic field. In this thesis I present the results of the numerical codes I developed to simulate the polarization pattern, both at the surface and as observed at infinity, of the radiation emitted from highly magnetized, isolated neutron stars, using as templates the bright AXP 1RXS J170849.0-400910 and the XDINS RX J1856.5-3754. I demonstrate that polarization measurements can indeed provide key information about the physical and geometrical properties of these sources, allowing to directly test theoretical models. This work is also relevant in view of the launch of new-generation X-ray polarimeters, currently under development, like the X-ray Imaging Polarimeter Explorer (XIPE). For this reason, I also compare theoretical models with XIPE simulated observations, in order to show how polarization measurements can be used to extract the values of magnetospheric parameters and viewing angles.

Sommario

Lo studio delle magnetars, anomalous X-ray pulsars (AXPs) e soft gamma repeaters (SGRs), e delle X-ray Dim Isolated Neutron Stars (XDINSs) è di particolare rilevanza, dal momento che questi oggetti mostrano i più forti campi magnetici mai osservati nell'universo ($10^{13} - 10^{15}$ G) e rappresentano i soli laboratori dove la fisica in presenza di campi magnetici così forti può essere testata. Fino ad ora, queste particolari stelle di neutroni sono state studiate attraverso misure spettroscopiche e di timing, che hanno portato a corroborare i modelli teorici formulati per spiegare la loro fenomenologia, come nel caso del "twisted magnetosphere" model per le magnetars o dei diversi modelli di emissione superficiale per le XDINSs. Cionondimeno, questa analisi da sola non riesce a fornire informazioni complete. A questo riguardo, la polarimetria X può svelare un approccio completamente nuovo nello studio delle stelle di neutroni altamente magnetizzate. La radiazione emessa in presenza di forti campi magnetici, infatti, è attesa essere altamente polarizzata; le misure di polarizzazione forniscono due osservabili aggiuntivi, la frazione di polarizzazione lineare e l'angolo di polarizzazione, che possono determinare senza ambiguità i parametri dei modelli anche quando la sola analisi spettrale si dimostra insufficiente. Il segnale di polarizzazione che un osservatore riceve all'infinito, tuttavia, non coincide necessariamente con ciò che i modelli predicono per la polarizzazione alla superficie, a causa degli effetti dell'elettrodinamica quantistica nel vuoto fortemente magnetizzato attorno alla stella, accoppiato con la rotazione dei parametri di Stokes nel piano perpendicolare alla linea di vista, indotta dal campo magnetico non uniforme. In questa tesi presento i risultati dei codici numerici che ho sviluppato per simulare il pattern di polarizzazione, sia alla superficie che all'infinito, della radiazione emessa da stelle di neutroni isolate altamente magnetizzate, usando come modelli la luminosa AXP 1RXS J170849.0-400910 e la XDINS RX J1856.5-3754. Dimostrerò che le misure di polarizzazione possono effettivamente fornire informazioni cruciali sulle proprietà fisiche e geometriche di queste sorgenti, permettendo di testare direttamente i modelli teorici. Questo lavoro è inoltre rilevante in vista del lancio di polarimetri X di nuova generazione, attualmente in fase di sviluppo, come l'X-ray Imaging Polarimetry Explorer (XIPE). Per questa ragione, confronterò i modelli teorici con osservazioni simulate di XIPE, allo scopo di mostrare come le misure di polarizzazione possono essere utilizzate per estrarre i valori dei parametri relativi alla magnetosfera e gli angoli di vista.

Acknowledgements

First and foremost I would like to thank my Ph.D. supervisor, Professor Roberto Turolla. It has been a great honour to be his Ph.D. student: I immensely appreciate all of his teachings and advice he gave me during these three years, that have been definitely the best years I spent at the university. I also thank him for the possibilities he gave me to attend schools and conferences in Italy and abroad. The great professionalism and the enthusiasm he conveyed to me have grown day after day my passion for research; he is for me a great role model as man and as physicist.

Particular thanks to Professor Luciano Nobili for his joy and dedication, for his tremendous skill in developing numerical codes and also for all his extremely clear notes: he helped me very much in improving my work during the Ph.D. course.

I would like also to thank Professor Silvia Zane, for many contributions, illuminant discussions and useful comments, especially during the writing of the latest works we published. I thank also Denis González Caniulef for the useful discussions, in particular during the period he spent in Padova, and the help he gave me.

I must thank particularly Professor Giorgio Matt and Dr. Fabio Muleri, Paolo Soffitta and Enrico Costa, who welcomed me during some visits at the INAF-IASF institute in Rome and accompanied me during the trip in Stockholm in 2014, where I held my first talk during a conference abroad. Many thanks also for the contributions and suggestions that Fabio, Paolo and Enrico gave for publications on which we worked together.

I also thank Dr. Sergei Popov for the discussions we made in the period he spent in the Physics Department of Padova during 2015.

I have to thank with immense gratitude my parents, who have always supported me and believed in me, and always stay close to me even in the most difficult moments. I hope I have made them proud of me.

Many thanks also to my brother Alessandro and my dearest friend Andrea, who endured me with patience, helped me with English and made happy my days in Padova with pizzas, crépes, films and the listening of really good music.

And finally I would like to thank my cousins Andrea, Estefi and my aunt Giuliana, for all the fun saturday evenings spent playing Muchkin, Liliana and Anna for all their advice, Jacopo, Annabella and all my friends, especially André, Jorge, Vincent and Noël, who I met during the years of my Ph.D. and with which I still am in touch.

Contents

Introduction

Neutron stars (NSs) are magnetized, fast rotating compact objects that are born in the core-collapse supernova (SN) explosion of massive stars ($10 \lesssim M/M_{\odot} \lesssim 25$), which are supported against their own gravity by the pressure of degenerate neutrons. First evisaged theoretically in the early thirties (Baade & Zwicky, 1934), NSs were identified observationally in 1967, when the first radio pulsars was discovered (Hewish et al., 1968; Pacini, 1968).

Radio pulsars (PSRs), characterized by the emission of (regular) radio pulses, are (relatively) abundant (more than 2400 are presently known, see the ATNF online pulsar catalog[1]) and quite easily detected with ground-based radio telescopes. This made them the archetypal NSs and for more than two decades PSRs have been the only known manifestation of isolated neutron stars (INSs). It was only at the beginning of the '90s, mainly thanks to high-energy observations, that the existence of different classes of isolated NS sources, with properties much diverse from that of standard radio pulsars, started to emerge (see e.g. Kaspi, 2010; Harding, 2013). Among these, the "magnetar candidates" are the most extreme and are believed to host the strongest magnetic fields in the present universe, higher than the quantum electron critical field ($B_{\rm Q} \sim 4.4 \times 10^{13}$ G) and up to 1000 times those typical of the PSRs. Even if their observational appearance is almost opposite to that of the magnetars, the so-called X-ray Dim Isolated Neutron Stars (XDINSs) are suspected to share with the former very strong magnetic fields and, possibly, to represent a later stage of the evolution of magnetars.

Magnetars, observationally identified with soft gamma repeaters (SGRs) and anomalous X-ray pulsars (AXPs), form a class of ultra-magnetized, NS X-ray sources, characterized by the fact that their activity does not appear to be powered by rotational energy losses, as in standard PSRs, but is rather sustained by the magnetic energy stored in their huge (internal) field. They show a number of peculiar properties: emission of short, energetic X-ray bursts, quite long rotational periods and large spin-down rates, as compared to ordinary radio pulsars; three SGRs have been also observed to emit giant flares, hyperenergetic events in which peak luminosities up to $\approx 10^{47}$ erg s^{-1} have been recorded (see e.g. Mereghetti, 2008; Rea & Esposito, 2011; Turolla & Esposito, 2013, for reviews). The spectrum of magnetar persistent X-ray emission is well fitted by the superposition of a thermal, blackbody component and a power-law tail (see Mereghetti, 2008; Turolla et al., 2015, for reviews). Nevertheless, in the case of magnetar transients, i.e. in sources which become detectable only during occasional flux enhancements (up to 1000 times the quiescent level, duration ≈ 1 yr), the spec-

[1] http://www.atnf.csiro.au/people/pulsar/psrcat

trum is nearly thermal, and modelled by one or more blackbody component(s) (see e.g. Rea & Esposito, 2011).

The magnetar model (Duncan & Thompson, 1992) has been quite successful in explaining the observational properties of magnetar bursting and persistent emission. In particular, according to the "twisted magnetosphere" model developed by Thompson et al. (2002), the external magnetic field of a magnetar acquires a toroidal component, becoming "twisted", as a consequence of the crustal deformations induced by the internal magnetic stresses. Since twisted fields are non-potential, currents must flow along the closed magnetic field lines, and the density of charged particles (mainly electrons and positrons) in the star magnetosphere is high enough to produce a large optical depth to resonant cyclotron scattering (RCS). The multiple scatterings that photons emitted from the star surface undergo on the moving charges fill the non-thermal tail of the spectrum, as confirmed by Monte Carlo calculations performed by Fernàndez & Thompson (2007) and Nobili, Turolla & Zane (2008a,b). Although current RCS models rely on a number of simplifying assumptions, mainly a "globally twisted" magnetosphere and rather ad hoc space and velocity distributions of the scattering charges (see Fernàndez & Thompson, 2007; Nobili, Turolla & Zane, 2008a), their systematic application to fit the observed spectra of SGRs and AXPs gave good results, allowing to infer the values of the magnetospheric parameters. However, spectral analysis alone is not bound to provide complete information, due to an inherent degeneracy in the RCS model parameters, so that different observational techniques are required to solve this issue.

The XDINSs (also known as the "Magnificent Seven" or M7) are, instead, seven close-by objects, possibly cradled in the young stellar clusters forming the Gould Belt (Popov et al., 2003), with estimated distances $\lesssim 500$ pc (Posselt et al., 2008). Similarly to AXPs and SGRs, also XDINSs are characterized by magnetic fields in general stronger than those inferred for rotation powered pulsars, with slower rotation and larger spin-down rates. Unlike magnetars, however, they exhibit a purely thermal spectrum, with no evidence for high-energy, power-law components or bursting activity; with the only exception of the XDINS RX J1856.5-3754, some broad absorption features have been detected and explained as transition lines in atmospheric layers or proton cyclotron lines. Optical counterparts, with magnitudes $\gtrsim 25$ have been identified to a varying degree of confidence for all the Seven, on the basis of proper motion measurements or positional coincidence (see e.g. Turolla, 2009; Kaplan et al., 2011). The optical flux appears to exceed the extrapolation of the X-ray blackbody at low energies by a factor $\sim 5 - 50$ and deviations from a Rayleigh-Jeans distribution have been reported in some sources (notably RX J2143.0+0654, see Kaplan et al., 2011). Several models have been developed to explain the nature of the surface emission from XDINSs. Thermal radiation can be reprocessed in a gaseous atmospheric layer (see e.g. Potekhin, 2014, for a review), or a phase transition can occur, owing to the strong magnetic fields and sufficiently low temperature, leaving the star surface bare (Lai & Salpeter, 1997; Lai, 2001; Burwitz et al., 2003; Turolla et al., 2004; Medin & Lai, 2007, see also Turolla 2009; Potekhin 2014). Nevertheless, no conclusive results have been obtained so far, due to the poor knowledge of the internal magnetic field structure and, consequently, of the surface temperature distribution in these objects.

X-ray radiation emitted from the surface of magnetars and XDINSs is expected to

be strongly polarized in two normal modes, the ordinary and the extraordinary mode, defined by the direction of the photon polarization vector with respect to that of the local magnetic field. In fact, photon interactions with charge particles in the presence of strong mangetic fields tend to favour one of the modes with respect to the other (see e.g. Gnedin & Pavlov, 1974). Moreover, magnetic scattering can influence the polarization state of photons propagating in a magnetized plasma (Harding & Daugherty, 1991; Lloyd, 2003) or in the magnetosphere of a magnetar (Nobili, Turolla & Zane, 2008a). Eventually, when photons propagate freely in vacuo quantum electrodynamics (QED) strongly affects polarization, locking the photon mode to the local magnetic field direction within the "adiabatic region" (the so-called "vacuum polarization", see e.g. Heyl & Shaviv, 2002), somehow amplifying the observable polarization signal at infinity (Heyl et al., 2003; Taverna et al., 2015).

Polarization measurements can open an entirely new approach for the determination of the physical and geometrical properties of highly magnetized NSs. Actually, radio and optical polarimetry has been already used to derive the orientation of the magnetic and rotation axes of radio pulsars (Manchester & Taylor, 1977; Lyne & Manchester, 1988). The discovery over the last two decades of an increasing number of X-ray bright INSs, like the magnetars and the XDINSs (despite their name they are quite bright), renewed the interest in possible polarization measurements at X-ray energies in NS sources. Although the first efforts made in the past to measure polarization in the X-rays (mainly with the OSO-8 and INTEGRAL satellites, see Weisskopf et al., 1978; Hughes et al., 1984; Dean et al., 2008) did not lead to conclusive results, the new-generation X-ray polarimeters like XIPE[2], IXPE (Weisskopf et al., 2013) and PRAXyS (Jahoda et al., 2015), recently selected for the study phase of the ESA M4 and NASA SMEX programmes, respectively, promise to improve current instrumental techniques, with a dramatic increase in sensitivity over an energy range $\sim 1-30$ keV (see Bellazzini et al., 2013).

X-ray polarimetry can indeed remove the spectral degeneracy in magnetar RCS models (Taverna et al., 2014), allowing to unambiguously measure the physical and geometrical parameters that characterize the magnetosphere. Furthermore, since the expected polarization pattern is different whether the emission comes from a gaseous atmosphere (van Adelsberg & Lai, 2006) or a condensed surface (Potekhin et al., 2012), the study of the polarization pattern of radiation emitted from XDINSs can provide key insight about the nature of strongly magnetized NS surface and ultimately probe the properties of matter in strong magnetic fields (Gonzàlez Caniulef et al., 2016). Polarization measurements can also be crucial in understanding the mechanisms that give rise to magnetar bursting activity: albeit these events have short durations, the polarimetric analysis of a sufficiently large sample of bursts (like that emitted by SGR 1900+14 in 2006 March, see Israel et al., 2008) can help in developing a complete model for magnetar burst emission, which is still to come.

Comparing the observed polarization properties of a NS source with theoretical expectations is not straightforward; this is due to the combined effects of QED and geometry. In fact, the Stokes parameters, that are used to conveniently express the polarization observables (i.e. the polarization fraction and the polarization angle), are

[2]http://www.isdc.unige.ch/xipe

defined with respect to a specific reference frame, which is in general different for each photon according to the direction assumed by the stellar magnetic field at the emission point. Hence, when the contributions of all photons are added together, in order to derive the polarization of the entire radiation, care must be taken to rotate them, so that they are referred to the same frame, which coincides with the frame in the focal plane of the detector. This effect, together with vacuum polarization, determines the polarization pattern that an observer at infinity would measure, which could be dramatically different from that predicted by theoretical models (see Taverna et al., 2015). Comparison of the "intrinsic", i.e. those at emission, and the observed polarization properties in highly magnetic NSs can provide the first observational evidence of vacuum polarization, an effect predicted more than 80 years ago (Heisenberg, 1936) but never experimentally tested; this will directly probe QED in the strong-field limit.

In this thesis I present a comprehensive study of the polarization properties of the radiation emitted by INSs, focusing in particular on magnetars and XDINSs. The main observational features of INSs and the phenomenology of AXPs and SGRs are described in chapter 1, together with the theoretical framework of the magnetar and the XDINS surface emission models. In chapter 2 I discuss the polarization evolution of the radiation emitted by NSs endowed with ultra-strong magnetic fields; I also introduce the Stokes parameters and the polarization observables relative to single photons and the entire radiation. The relation between the intrinsic and the observed polarization patterns in the simple case of a thermally emitting INS, endowed with a dipolar magnetic field, is presented in chapter 3, using a specific ray-tracing code. The Monte Carlo code used to simulate the polarization signal of magnetar persistent emission, together with the numerical results, is described in chapter 4. In chapter 5 I present the expected polarization pattern of the radiation emitted by a typical XDINS, both for the magnetized atmosphere and condensed surface emission models, showing how polarization measurements can discriminate between them. A description of the new-generation polarimetric techniques is provided in chapter 6 with some observational simulations that show how physical and geometrical properties of magnetar magnetospheres can be extracted from polarization measurements of their persistent X-ray emission. In chapter 7 I present a preliminary model for magnetar burst emission, based on the propagation of ordinary and extraordinary photons through the magnetized plasma emitted during magnetar bursts. Finally, chapter 8 contains the conclusions.

Chapter 1

Physics of strongly magnetized neutron stars

Neutron stars are observed across the enitre electromagnetic spectrum, from the radio band to very high-energy gamma rays. After a short general introduction, in this chapter I focus in particular on some classes of neutron stars that show the most peculiar observational properties and that are believed to host the most powerful magnetic fields in the universe. I also discuss some results obtained so far and describe the theoretical models developed to explain the observed phenomenology.

1.1 Neutron star basics

Soon after the observational discovery by Hewish et al. (1968), neutron stars (NSs) were identified with radio pulsars (PSRs), that exhibit regular pulsations in the radio band. Although existence of several different types of NS sources have been confirmed by observations, the number of detected radio PSRs is by far the largest. In a sense, radio PSRs are the archetypal NSs and the toolkit used to derive their properties have been, and still are, applied (rather acritically) also to the other NS classes.

The energy that sustains PSR emission is supplied by their fast rotation (this is why they are also called "rotation powered"), via the braking operated by their intense magnetic field, that is usually assumed to be dipolar. A rotating dipole emits electromagnetic energy according to the Larmor formula:

$$\dot{E}_{\rm rad} = -\frac{2}{3c^3}|\ddot{\boldsymbol{m}}|^2 = -\frac{B_{\rm pol}^2 R_{\rm NS}^6 \Omega^4 \sin^2\xi}{6c^3}\,, \tag{1.1}$$

where $\ddot{\boldsymbol{m}}$ is the second time derivative of the magnetic dipole moment, $B_{\rm pol}$ is the magnetic field strength at the magnetic poles, ξ is the angle between the dipole axis and the star spin axis, $R_{\rm NS}$ is the stellar radius and $\Omega = 2\pi/P$ the star angular frequency. The spin period P of PSRs (typically in the range $\approx 0.01 - 1$ s) is measured from the pulsations they show in the radio band. By equating $\dot{E}_{\rm rad}$ given by equation (1.1) with the rotational energy losses $\dot{E}_{\rm rot} = I\Omega\dot{\Omega}$ (where I the stellar moment of inertia) it results

$$\frac{\dot{\Omega}}{\Omega^3} = -\frac{B^2 R_{\rm NS}\sin^2\xi}{6Ic^3}\,; \tag{1.2}$$

as it can be seen from the minus sign at the right-hand side, the rotational motion of the star slows down. Solving the previous equation for $B_{\rm pol}$ and taking typical values of the star parameters (mass $M_{\rm NS} = 1.4\,M_\odot$ and radius $R_{\rm NS} = 10$ km, so that $I \approx 10^{45}$ g cm^2), one obtains

$$B_{\rm sd} \equiv B_{\rm pol} = \sqrt{\frac{6Ic^3}{4\pi^2 R_{\rm NS}^6 \sin^2\xi}\,P\dot{P}} \approx 3.2\times10^{19}\sqrt{P\dot{P}}\ {\rm G} \tag{1.3}$$

with $\dot{P}$ the spin-down rate, that for PSRs is in the range $\approx 10^{-16}-10^{-12}$ s s^{-1}. Equation (1.3) gives the intensity of the stellar magnetic field, assuming that all the rotational loss $\dot{E}_{\rm rot}$ is converted in radiation power $\dot{E}_{\rm rad}$.

Integrating, instead, equation (1.2) over the time, starting from the star birth $t = 0$ up to the current time $t = t_{\rm c}$, one has

$$\frac{1}{\Omega^2(t_{\rm c})} = \frac{2B^2 R_{\rm NS}^6 \sin^2\xi}{6Ic^3}\,t_{\rm c}\,, \tag{1.4}$$

where the magnetic field has been considered as constant and, since the star slows down, it has been assumed $\Omega(0) \gg \Omega(t_{\rm c})$. Then, from equations (1.2) and (1.4) and solving for $t_{\rm c}$ one obtains

$$\tau_{\rm c} \equiv t_{\rm c} = \frac{1}{2}\frac{P}{\dot{P}}\,, \tag{1.5}$$

that is called the "characteristic age" of the star. Actually $\tau_{\rm c}$ is a good approximation of the real star age (that can be evaluated through different methods, e.g. from the kinamatics or the cooling properties of the source) if indeed the spin period of the star at birth is much smaller than that today.

P and $\dot{P}$ play a fundamental role in characterizing the NS properties (see equations 1.3 and 1.5) and the Galactic NS population is usually represented in the $P-\dot{P}$ diagram, shown in Figure 1.1. Rotation powered PSRs, the most abundant population, fill the central region of the plot, while the "millisecond" PSRs are placed at the bottom-left corner, at small values of P and $\dot{P}$. Magnetars and other "peculiar" classes of isolated NSs (see next section) are instead in the opposite corner, at large P and $\dot{P}$. Since $B_{\rm sd} \propto \sqrt{P\dot{P}}$ and $\tau_{\rm c} \propto P/\dot{P}$, the lines of constant magnetic field and age are also plotted in the $P - \dot{P}$ diagram. If the star magnetic field does not decay, a NS evolves moving along the constant $B_{\rm sd}$ line towards larger values of the period, much in the same way as a normal star evolves along a track in the Hertzprung-Russel diagram.

1.2 Isolated neutron stars

In this section I focus in particular on the group of isolated neutron stars (INSs) for which, at variance with conventional radio PSRs, X-ray emission is not powered by rotational energy losses. Beside magnetars, that will be discussed in detail in the following section, the group includes X-ray dim isolated neutron stars (XDINSs), central compact objects (CCOs) and rotating radio transients (RRATs). A list of the confirmed and candidate INSs is reported in Mereghetti (2011, table 1).

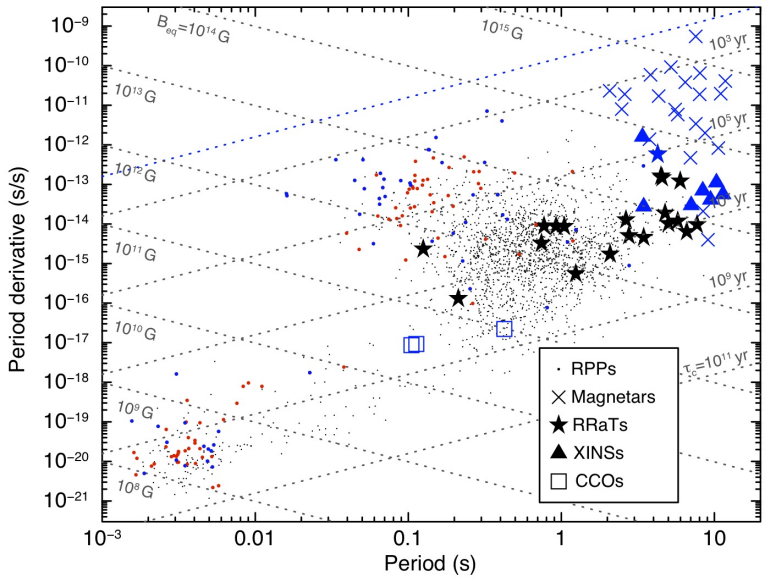

Figure 1.1: Isolated neutron star population in the period − period derivative plane ($P - \dot{P}$ diagram). The various types of NSs are highlighted with different symbols: rotation powered PSRs (dots), magnetars (crosses), RRATs (stars), XDINSs (triangles) and CCOs (squares). In red are indicated the sources for which the emission has been observed both in the X-ray and radio bands, while in blue those observed in the X-rays only. The dotted lines represent the loci of the points with constant magnetic field (negative slope) and constant characteristic age (positive slope).

1.2.1 X-ray dim isolated neutron stars

XDINSs (also known as The Magnificent Seven, see Haberl, 2007; Turolla, 2009, for reviews) are seven close objects, firstly discovered by the ROSAT All Sky Survey. Due to their small distance ($\lesssim 500$ pc), XDINSs are considered the optimal candidates to constrain the still unknown NS equation of state, since good estimates of their radii and/or masses could be obtained. Emission is peaked in the X-rays (X-ray to optical flux ratio $\approx 10^4 - 10^5$), with luminosities $L_{\rm X} \approx 10^{30} - 10^{32}$ erg s^{-1}, sinusoidal light curves (pulsed fractions $\approx 1.3 - 20\%$) and soft, quasi thermal spectra ($T \approx 40 - 110$ eV), well fitted by one or two blackbody components (see e.g. Mereghetti, 2011). A peculiar spectral property is the absence of high-energy tails or other components related to non-thermal emission processes. Broad absorption features, explained as atomic transitions in atmospheric layers, have been observed in many sources (see e.g. Kaplan & van Kerkwijk, 2006), even if the occurrence of some of these lines at energies above ≈ 0.5 keV make the association with bound-bound transitions in a hydrogen atmosphere unlikely. An alternative explanation is that such features can be proton cyclotron lines, as confirmed at least in the case of RX J0720.4-3125 (see e.g. Borghese et al., 2015). Only for the XDINS RX J1856.5-3754 the spectrum appears featureless, suggesting the possibility that radiation is emitted directly from the bare star surface, resulting from magnetic condensation mechanism (as discussed in section 1.5).

Timing observations allowed to measure rotational periods $P \approx 3 - 11$ s and period derivatives $\dot{P} \approx 10^{-14} - 10^{-13}$ s s^{-1}, quite large compared with those of common rotation powered PSRs. These values, which place the XDINSs in a well-defined region of the $P - \dot{P}$ diagram (see Figure 1.1), lead to relatively high surface magnetic field strengths $B_{\rm sd} \approx 10^{13}$ G. Characteristic ages result in the range $\tau_{\rm c} \approx 1 - 4$ Myr (see Kaspi, 2010), although kinematic age measurements give lower values (~ 0.4 Myr, see Turolla, 2009; Mereghetti, 2011, and references therein). The lack of radio emission suggests that XDINSs may be rotation powered PSRs with an unfavourable beaming geometry (Kondratiev et al., 2009). Standard cooling curves, however, predict X-ray luminosities too low for the inferred age. A possible explanation can be related to their unusually strong magnetic field, the dissipation of which can act as an additional source of heating. This scenario, in particular, would strengthen the idea of a connection between XDINSs and magnetars: the former would be old, evolved magnetars, for which the magnetic field has substantially decayed.

1.2.2 Central compact objects

CCOs are INSs located at the center of supernova remnants (SNRs). The estimated ages of the SNRs (few tens kyrs) indicate that they are young (see de Luca, 2008; Halpern & Gotthelf, 2010, for reviews). Only for three CCOs a direct measurement of the spin period P has been possible, from X-ray pulsations, and all the measured values are compatible with those of young NSs: $P = 0.424$ s for 1E 1207.4-5209, 0.112 s for RX J0822.0-4300 and 0.105 s for CXOU J185238.6+004020. Unexpectedly, very small time derivatives has been found for these sources, ranging in between $\dot{P} \approx 10^{-18} - 10^{-16}$ ss^{-1} (see Viganò & Pons, 2012, and references therein). As a result, in all the three cases the inferred value of the spin down magnetic field is in the range $B_{\rm sd} \approx 10^{10} - 10^{11}$

G, the lowest ever estimated for INSs. In addition, for the three CCOs above, the characteristic ages τ_c are of order $\approx 10 - 100$ Myr, clearly exceeding the age of the corresponding SNR; this in particular suggests that their initial rotation periods were very close to the current ones. All these evidences led to explain CCOs as "anti-magnetars": the slow rotational motion at birth would prevent the magnetic field amplification, at variance with the case of magnetars (see §1.4.1).

The spectra of these sources are thermal, well fitted by two blackbodies with measured temperatures $T_1 \approx 0.16 - 0.4$ keV and $T_2 \approx 0.3 - 0.8$ keV (Mereghetti, 2011). This can be interpreted as an indication of a non-uniform temperature distributions on the surface. However, the associated emitting areas are quite small ($R_1 \approx 0.4 - 4$ km and $R_2 \approx 0.06 - 0.8$ km), contrary to what one expects for low-field NSs; so, to have larger radii, atmospheric models were invoked (see e.g. Ho & Heinke, 2009). Recently, in order to explain the peculiar properties of CCOs, alternative models have been formulated involving the fallback of supernova debris on the surface of the newborn NS (see Ho, 2011; Viganò & Pons, 2012; Torres-Forné et al., 2015). According to these models, the actual magnetic field of these objects (which is expected to be stronger than the inferred values of $B_{\rm sd}$) is buried into the crust and can reemerge when the accretion flux will stop. A possible confirmation of this theory could be given by polarization measurements: in fact, the arise of a quite strong magnetic field would modify the polarization state of X-ray photons emitted from the star, increasing the overall polarization degree (see chapters 2 and 3).

1.2.3 Rotating radio transients

The discovery of RRATs (see Keane & McLaughlin, 2011, for a review) has been possible thanks to the Parkes Multibeam Survey. These INSs emit short radio bursts, with duration $\approx 2 - 30$ ms at intervals ranging between some tens and some thousands of seconds, but no direct observations of the rotational period have been made. The available estimates $P \approx 0.4 - 7$ s were inferred from the largest common divisors of the time intervals between radio bursts (Mereghetti, 2011). The spin down rate, instead, has been determined only for a few of the ~ 100 RRATs discovered so far (see the RRAT online catalog[1]), leading to dipolar magnetic field strengths $\gtrsim 10^{13}$ G.

Since their positions in the P-$\dot{P}$ diagram are quite scattered (see figure 1.1), the definition of RRATs as an independent group of INSs is still uncertain. Initially they have been interepreted as extreme manifestations of rotation powered PSRs, also owing to their detection only as transient radio sources. Nevertheless, their strong spin down magnetic fields and the emission of frequent bursts seem to suggest some similarities with magnetars. In particular, one of these objects, PSR J1819-1458, was indeed observed to emit also in the X-rays (McLaughlin et al., 2007; Camero-Arranz et al., 2013), with luminosity $\approx 10^{32} - 10^{33}$ erg s^{-1}, nearly sinusoidal light curve (pulsed fraction about 35%) and a thermal spectrum characterized by a temperature ~ 130 eV, with an unusual absorption feature at ~ 1 keV. Initially explained with the presence of a surrounding nebula powered by the star rotational energy (see e.g. Rea et al., 2012), it was soon clear that the X-ray emission detected from PSR J1819-1458 has relatively

[1] http://astro.phys.wvu.edu/rratalog/

little in common with conventional pulsar wind nebulae (PWNe). In fact, the small spin down luminosity $\dot{E}_{\rm rot}$ of the source would imply an extremely high efficiency, compared with those of observed PWNe, in converting rotational into radiative energy ($\sim 20\%$, see Kaspi, 2010; Mereghetti, 2011). Thus, the idea that, also in this case, high-intensity magnetic fields can provide an additional energy source is strongly attractive. In this respect, Miller et al. (2011) tried to explain the 1 keV absorption feature in terms of a proton cyclotron line, obtaining a value of $B \approx 2 \times 10^{14}$ G, as strong as in magnetars. However, also alternative hypotheses have been explored, as for example a shock due to a high-velocity translational motion (see Mereghetti, 2011).

1.3 Magnetar phenomenology

A magnetar is a particular kind of NS endowed with a ultra-strong magnetic field and characterized by the emission of repeated bursts in the hard-X/soft-gamma ray bands (see Mereghetti, 2008; Turolla et al., 2015, for reviews). For hystorical reasons, these sources have been observationally identified within two different groups, the soft gamma-ray repeaters (SGRs) and the anomalous X-ray pulsars (AXPs).

The short, energetic bursts detected from SGRs led initially to associate them to gamma-ray bursts (GRBs). However, the fact that repeated events were detected from the same sources (whereas GRBs never repeat) excluded this association, and the further detection of pulsations in SGR burst tails confirmed that they are NSs. AXPs, instead, were immediately identified with X-ray emitting NSs, although right from the start it was realized that they were "anomalous"; i.e. they showed an unexpectedly high luminosity, that clearly exceeds the rotational energy loss rate $\dot{E}_{\rm rot}$. The attempts to explain this phenomenlogy in terms of accretion or wind nebulae failed very soon once the research for companion stars or surrounding plasma did not give any positive result. In the last years a great number of properties shared among AXPs and SGRs was revealed, including the discovery of short bursts emitted also by AXPs; thus, nowadays the scenario for which AXPs and SGRs are different manifestations of an unique type of INSs (the magnetars) is commonly accepted.

SGRs and AXPs are among the INSs that exhibit the longest rotational periods, in the $2-12$ s range, and period derivatives $\dot{P}$ between $10^{-13}-10^{-11}$ s s^{-1} (see the McGill Online Magnetar Catalog[2]), setting magnetars in a well-defined region of the $P-\dot{P}$ diagram (see Figure 1.1). This leads to very high values of the spin-down magnetic field, $B_{\rm sd} \approx 10^{14}-10^{15}$ G, while, correspondingly, the characteristic ages are in between $\sim 1-10^3$ kyr.

In the remaining discuss of this section I describe the most important emission properties that characterize magnetars.

1.3.1 Persistent X-ray emission

Magnetar persistent emission has been well-studied especially in the X-ray band, in which SGRs and AXPs show a luminosity $L_{\rm X} \approx 10^{33}-10^{36}$ erg s^{-1}. As mentioned before, this is some orders of magnitude greater than the spin-down luminosity $\dot{E}_{\rm rot}$,

[2]http://www.physics.mcgill.ca/~pulsar/magnetar/main.html

that is $\approx 10^{32}$ erg s^{-1} for the measured values of P and $\dot{P}$. Therefore, magnetar emission can not be powered by rotation, contrary of what happens for radio pulsars: Duncan & Thompson (1992) and Paczynski (1992) first proposed that SGR/AXP activity is sustained by the magnetic energy stored in the (internal) magnetic field.

Pulsed fraction in the soft X-ray band ($0.5 - 10$ keV) are for many sources in the $\approx 10 - 20\%$ range, with pratically sinusoidal pulse profiles characterized by single or double peak shapes. Persistent spectra at these energies are typically thermal, fitted by a blackbody curve with temperature ≈ 0.5 keV, with the addition of a non-thermal tail that in general follows a steep power law with spectral index $\sim 2 - 4$ (see e.g. the left-hand panels of Figure 1.2). There are, however, several examples in which a two blackbody fit works well in all the soft X-ray band, especially in the case of transients (see §1.3.4), suggesting that the surface emission can be characterized by a non-uniform temperature distribution. While thermal components reflect the cooling emission coming from the surface, power law tails arise most probably in the magnetosphere, where scattering between thermal photons and the charged particles that flow along the closed magnetic field lines can boost the photon energy (see §1.4.4 for a complete discussion). Some fits involving atmospheric models have been also proposed (see Turolla et al., 2015, and references therein), even if the presence of an atmospheric layer above the surface of a magnetar is considered quite unlikely, due to magnetospheric activity, e.g. the returning currents that bombard the surface with high-energy charged particles (see §1.4.2 for more details).

Observations with INTEGRAL, RXTE and Suzaku satellites pointed out also a hard X-ray ($\gtrsim 20$ keV) component in the spectrum of a number of objects (see Turolla et al., 2015, and references therein). These high-energy tails are well fitted by a power law, characterized by a spectral index ($\approx 1 - 2$) in general different from that of the soft X-ray tails. With the advent of the NuSTAR satellite in 2012, with an energy range $3 - 79$ keV, it has been possible to better investigate the hard X-ray emission of magnetars, allowing in particular to locate the energy at which the soft and the hard tails match (see e.g. Figure 1.2). The non-thermal process that gives rise to this hard spectral component is still unknown: according to the models that have been developed so far, two mechanisms are believed the most likely. Hard X-ray emission observed from magnetars could originate by thermal bremsstrahlung or synchrotron emission due to the returning currents on the star surface (Thompson & Beloborodov, 2005). Alternatively, the hard non-thermal tail could be explained by the same Compton scattering process between thermal photons and charged particles that produces the softer one. While the soft tail is obtained by considering mildly relativistic scattering particles (i.e. with Lorentz factors $\gamma \sim 1$, see Nobili, Turolla & Zane, 2008a), the harder one can be reproduced by taking into account scatterings on highly relativistic electrons (see Beloborodov, 2013). Actually, as shown by Nobili, Turolla & Zane (2008b), scattering on mildly relativistic particles only can reproduce both the soft and hard tails in the case of comparable photon indices ($\Gamma_{\rm s} \simeq \Gamma_{\rm h}$), provided that QED effects and electron recoil are considered in the scattering cross section.

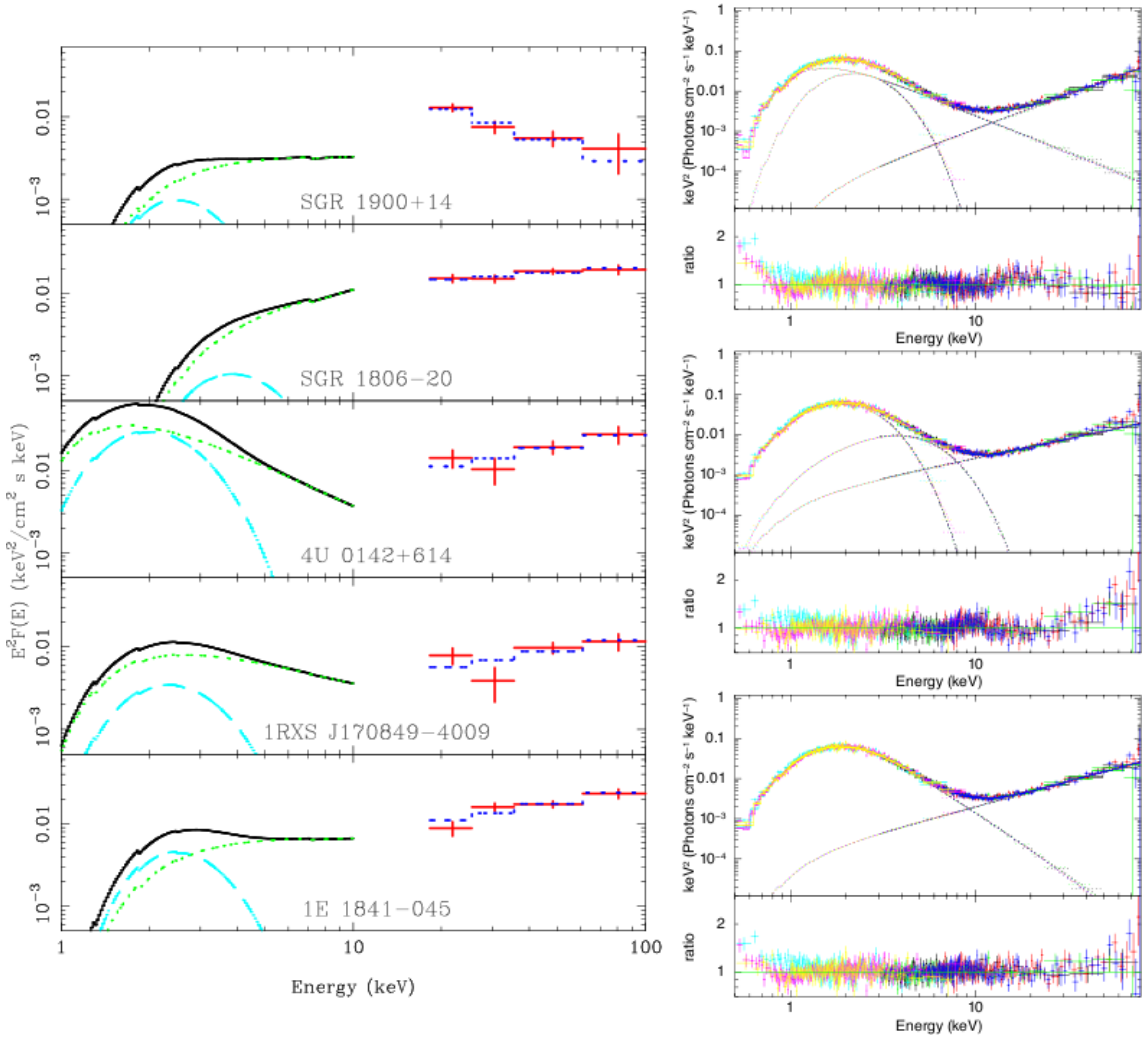

Figure 1.2: Magnetar X-ray spectra. Left-hand panels: XMM spectra (black solid lines) and INTEGRAL (red points with error bars) from different magnetar sources (Götz et al., 2006). The fitting curves are also shown: blackbody (cyan, dashed lines) plus absorbed power law (green, dotted lines) below 10 keV and power law (violet, dotted lines) above 20 keV. Right-hand panels: spectra of the AXP 4U 0142+0614 from different Swift-XRT (cyan, yellow, magneta points with error bars) and NuSTAR (black, red, blue points with error bars) observations, fitted by blackbody+powerlaw+powerlaw (top panel), blackbody+blackbody+powerlaw (middle panel) and comptonized blackbody+powerlaw (bottom panel) models (Tendulkar et al., 2015). The data-to-model ratios are also shown.

1.3.2 Optical/IR and radio emission

Magnetar emission has been certainly best investigated in the X-ray band; nevertheless observations have been carried out also at different wavelengths, to explore possible counterparts. Most results have been obtained in the optical/near IR band, even if the detected fluxes at these energies are remarkably low. Moreover, for the AXP 4U 0142+614 it was possible to obtain also the optical/IR spectrum, that shows a peculiar IR flattening, i.e. the photon counts in the IR band are in excess with respect to the blackbody that fits the optical continuum (Hulleman et al., 2000, 2004). Albeit observed in 4U 0142+614 only, this IR excess can possibly be present in the spectra of other (fainter) sources, still unobserved

The origin of optical/IR emission is still not entirely understood. It has been proposed that it can arise in the magnetosphere, due again to processes involving charged particles that stream along the closed magnetic field lines. The discovery by Israel et al. (2005) of a correlation between the optical/IR component and the hard X-ray one may support this scenario, that, if confirmed by future observations, could easily explain also the IR excess mentioned above. Another hypothesis is that optical/IR emission is generated from a fallback disk (see e.g. Perna et al., 2000; Turolla et al., 2015, and references therein). In fact, multi-color blackbodies with temperatures between 700 and 1200 K fit the spectrum of 4U 0142+614 (apart from the IR excess), a characteristic signature of the presence of a disk around the source.

Although for long time magnetars were believed to be radio quiet, in the last years radio counterparts have been observed for a handful of transients sources, the AXP XTE J1810-197 being the first ever detected (Camilo et al., 2006). However radio emission observed in magnetars shows quite different features from that of PSRs. In fact, it is associated to the source outbursting events (see the next sub-section for more details), and is characterized by a flat spectrum. Nevertheless, similarly to PSRs the X-ray luminosity of most of the radio-active magnetars is compatible or smaller than $\dot{E}_{\rm rot}$, (Rea et al., 2012). This suggests that the mechanisms responsible of the radio emission in transient magnetars could have the same origin as in PSRs.

1.3.3 Bursting activity

Emission of short bursts as well as of more energetic flares is the most characterizing feature of AXPs and SGRs; it was indeed the detection of one of these extreme events that led to the discovery in 1979 of SGR 0526-66, the first source afterwards identified as a magnetar (see e.g. Mazets et al., 1982). Magnetar bursts can be classified into three different types of phenomena, according to duration and luminosity: short bursts, intermediate flares and giant flares (see Turolla et al., 2015, for a complete review).

Short bursts are the most common events, observed in both AXPs and SGRs. They are characterized by generally symmetric light curves, with either single or multiple peaks (see Figure 1.3), a duration between 0.01 and 1 s, luminosities $\approx 10^{36} - 10^{42}$ erg s^{-1} and a total released energy $\approx 10^{36} - 10^{41}$ erg. A few events are followed by an extended tail, with duration ranging from some tens to some hundreds of seconds and modulated at the rotation period of the star (see Figure 1.4). Although initially longer bursts were considered as typical of AXPs and the shorter ones of SGRs (see

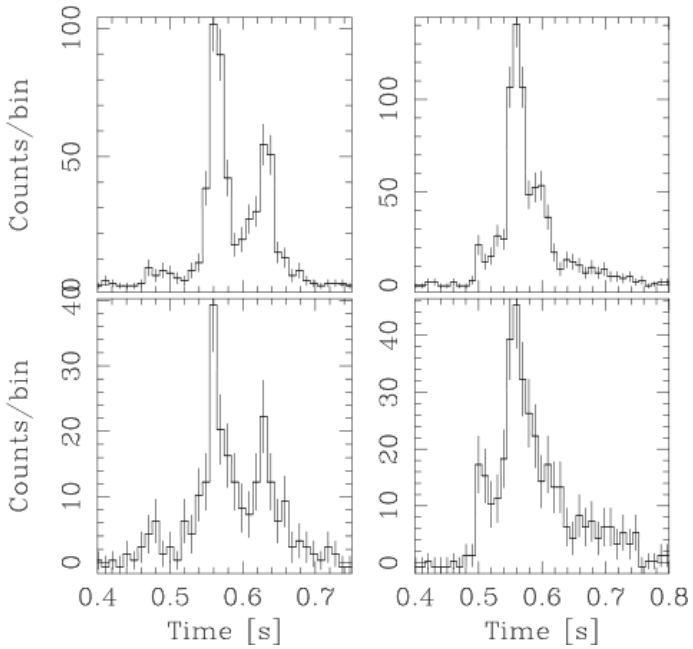

Figure 1.3: Light curves of two short bursts collected from SGR 1806-20 by the INTEGRAL satellite, in the soft ($E \approx 15 - 40$ keV, top panels) and in hard ($E \approx 40 - 100$ keV, bottom panels) energy bands (Götz et al., 2004).

Mereghetti, 2008), several sources have then been observed to emit both types of bursts, confirming the unified scenario for AXPs and SGRs. Spectra are over the entire energy range $1 - 100$ keV, well represented by a double blackbody model, with temperatures $T_1 \approx 2 - 7$ keV and $T_2 \approx 7 - 12$ keV respectively. Alternatively, also an optically thin thermal bremsstrahlung model, with temperature $T \approx 30 - 40$ keV can give a good fit, provided that the absorption is greater than that of the underlying persistent emission (see Mereghetti, 2008; Israel et al., 2008). This may support the idea that bursts are accompanied by the emission of a plasma fireball that remains trapped in the magnetosphere (see chapter 7).

Intermediate flares differ from short bursts essentially for the amount of released energy, that is some orders of magnitude greater ($10^{41} - 10^{43}$ erg). Light curves and spectral properties are rather similar to those of the more common short bursts. Intermediate flares mostly appear to be organized in two phases, both generally longer than in short bursts: an initial peak, with duration between half and a few seconds, followed by a longer tail (thousands of seconds), pulsating at the star spin period. Some sources have been observed to undergo the so-called "burst storms", i.e. periods of intense bursting activity, characterized by the emission of a great number of short bursts and intermediate flares. The "burst forest" emitted by SGR 1900+14 between 2001 and 2006, has been among the first cases reported (see Figure 1.4) and provided sufficient statistics to study in more detail the spectral properties of bursts (see Israel et al., 2008).

Finally, giant flares are the most powerful, albeit rare, events ever observed from compact objects, second only to GRBs and blazars. This kind of phenomenon has

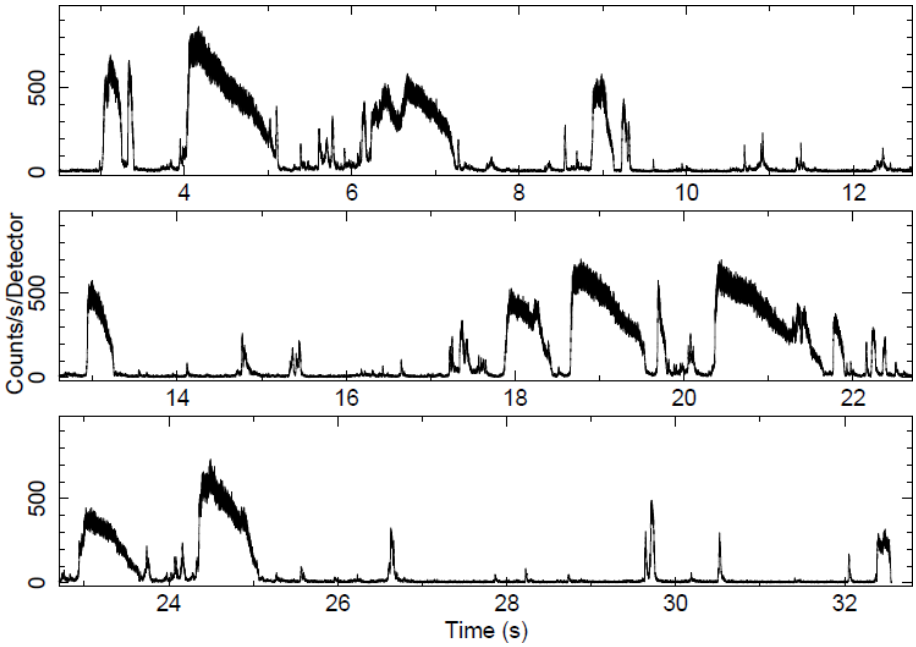

Figure 1.4: Sub-sample of the light curve obtained by SWIFT during "burst forest" emitted by SGR 1900+14 in March 2006. Different types of short bursts and some intermediate flares are visible (Israel et al., 2008).

been seen so far only in three SGRs (see Figure 1.5): SGR 0526-66 (Mazets et al., 1979), located in the large Magellanic cloud; SGR 1900+14 (Hurley et al., 1999); and SGR 1806-20 (Hurley et al., 2005); the latter emitted is the brightest giant flare ever observed so far. The total energy released during one of these events lies in the range $10^{44} - 10^{47}$ erg, the greatest part of which is in the strong initial spike, with very short duration ($\approx 0.1 - 1$ s) and peak luminosities up to 10^{47} erg s^{-1}. In all the three observed case the spike has been followed by a $\approx 100 - 1000$ s pulsating tail. The initial peak and the tail show different spectra. During the peak the spectrum is quite hard, with photons detected up to an energy ≈ 2 MeV. Due to the short duration, as well as to the small number of events, the identification of a good fitting model is rather difficult, even if a blackbody curve with variable temperature between 170 and 230 keV gives a good result (see Turolla et al., 2015, and references therein). In the case of the tail, instead, the spectrum is more similar to that of the burst tails, well fitted by an optically thin thermal bremsstrahlung model with temperature of some tens of keV (see e.g. Mereghetti, 2008). In the giant flare aftermath of SGR 1806-20, radio emission has been detected, probably originated in the shocked material emitted during the giant flare itself. In any case, this radio emission is not akin to the radio counterparts of transients described above, since the two phenomena have different origin.

The mechanisms that trigger magnetar bursting activity are still not completely known. The most reliable hypothesis is strictly related to the magnetic field topology. In particular, as extensively explained in §1.4.2, the presence of a not negligible toroidal component makes it possible for charged particles to fill the magnetosphere, and fast

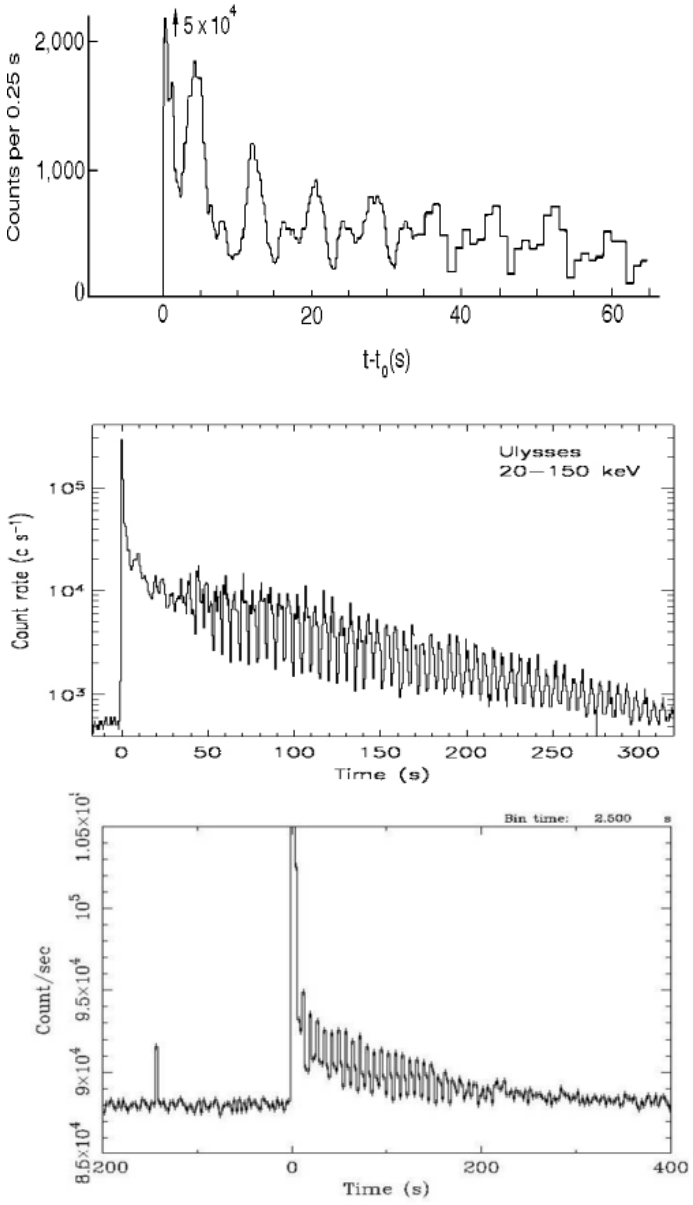

Figure 1.5: Light curves of the three giant flares observed up to now from SGR 0526-66 (top panel), SGR 1900+14 (middle panel) and SGR 1806-20 (bottom panel, Mereghetti, 2008, see also references therein).

accelerations of these particles, due to spontaneous magnetic field reconnections, can release the enormous energy amounts observed in short bursts and giant flares. The causes that lead to such reconfigurations are still subject to debate. Strong stresses exterted on the conductive crust by the internal magnetic field could induce a plastic deformation of the surface, causing a fracture of the crust that triggers the burst. Alternatively, the magnetic field reconfiguration can be due to a core instability in the interior of the star (Thompson & Duncan, 1995). In this latter case, however, the superconductivity that models infer for the core would prevent the formation of such instability, except in the case of an internal magnetic field with intensity $\gtrsim 10^{16}$ G, that would suppress superconductivity (see Turolla et al., 2015). If this were the trigger mechanism of giant flares, such exceptional request could explain why so few events has been observed so far.

1.3.4 Transients

Within the magnetar population, a remarkable class is that of transients (see Turolla et al., 2015, for an updated list), characterized by a strong variability in their X-ray emission. In fact, some sources show outbursts, i.e. sudden enhancements of the X-ray flux up to a factor of 1000 with respect to the value in the quiescence phase, during a period of ≈ 1 yr, frequently associated with burst emission. In some cases, outburts were key in revealing previously undetected sources, with a quiescence emission too faint to be observed. Repeated outbursts have been also observed from a few sources.

As outlined in sub-section 1.3.1, a common property of transients is that their spectra, during the outburst phase, are often well fitted by the superposition of two blackbodies, with temperatures $0.3-0.9$ keV, generally higher than those in quiescence (when detected). This suggests that the magnetospheric processes acting in transients are somehow different from persistent magnetars. In the case of transients it has been proposed that the external magnetic field develops a local toroidal component, i.e. involving only a bundle of magnetic field lines. Since the density of charged particles is much lower than in the case of persistent sources, scatterings of thermal photons are less frequent and power law tails are barely populated. Moreover, since the transmission of the toroidal component from the internal to the external field occurs essentially through crustal deformation (see §1.4.2), this could also explain why the transient outbursts are usually observed in correspondence to an active bursting phase.

Very recently, Tiengo et al. (2013) have shown that the mangetic field intensity in these local magnetospheric structures can be very strong. It is the case of SGR 0418+5729, a transient source characterized by a particularly low dipole magnetic field ($B_{\rm sd} \simeq 6.1 \times 10^{12}$ G), but showing the bursting activity typical of magnetars. Since its characteristic age results ≈ 36 Myr, it has been thought that this source could be an old magnetar, for which the magnetic field has considerably decayed. In the X-ray spectrum measured during an outburst phase in 2009, a clearly visible absorption line was detected, and interpreted in terms of a proton cyclotron line. This requires a magnetic field strength $\approx 10^{15}$ G, fully in the magnetar range, that is indeed expected to be localized in a small-scale magnetic structure. Similar properties are shown also by another source, Swift J1822.3-1606, for which the spin-down magnetic field intensity is $\approx 10^{13}$ G. However, the result obtained for SGR 0418+5729 may be the first direct

estimate of the strong magnetic fields of magnetars up to now.

1.4 Magnetar model

In this section I describe some theoretical aspects of magnetars, including short discussions about the formation scenarios, the physics of the magnetosphere and the interactions between the thermal photons emitted from the star surface with the magnetospheric charges. These elements are useful for theoretical simulations (described in the next chapters) aimed at reproducing magnetar spectral and polarization properties.

1.4.1 Formation scenarios

The issue of the magnetar formation is strictly related to the mechanism that produces their ultra strong magnetic fields. According to the first model developed by Duncan & Thompson (1992), internal magnetic fields with strength up to 10^{16} G can arise in newborn, fast rotating NSs due to $\alpha - \omega$ dynamo effects, which act in the presence of both convective motion and differential rotation. In order to explain within this scenario the observed features of SGRs and AXPs, their initial spin periods should be $\lesssim 3$ ms (Thompson & Duncan, 1993). This implies very energetic SN events, with $\approx 10^{52}$ erg transferred from the proto-NS to the SN ejecta through magnetic breaking; moreover, the spatial velocity of the compact object is expected to be $\approx 10^3$ km s^{-1}, i.e. up to a factor 3 greater than that of standard PSRs. No evidences of such energetic events have been found so far (Vink & Kuiper, 2006; Vink, 2008) and, although some models predict that high spatial velocities can be prevented invoking the superposition of magnetic dipole and quadrupole radiation (see e.g. Kojima & Kato, 2011), no spatial velocities significantly larger then those detected for other NSs have been measured (see e.g. Helfand et al., 2007).

A second scenario, proposed by Ferrario & Wickramasinghe (2008), envisages the formation of magnetar fields starting from massive progenitors endowed with magnetic fields $\approx 10^3$ G, that are amplified in the collapse of the core through magnetic flux conservation. According to this model, which is called the "fossil-field" scenario, such magnetic fields can be present in OB stars with masses between 20 and 45 $M_\odot$, despite the fact that, in the common evolutionary scenario, stars with this mass should give origin to black holes (BHs). Nevertheless, for some SGRs and AXPs located in young open clusters, the association with high-mass progenitors is strongly supported by observations (see Turolla et al., 2015, and references therein). In any case, the number of objects that this model predicts is too low compared with the total number of magnetars observed so far, and the actual population is expected to be even larger, as the discovery of many of transients indicates. The problem can be partially solved by invoking different channels of formation: for instance, Popov & Prokhorov (2006, see also Bogomazov & Popov 2009) suggested that tidal synchronization mechanisms in close binary systems can increase the predicted formation rate of magnetars, ensuring the fast rotation of the collapsing star.

A different scenario, that involves the dynamical evolution of binary systems, has been recently proposed by Clark et al. (2014), from the observation of the young open

cluster Westerlund 1, where the AXP CXOU J1647-45 is located. By studying the age of the cluster and the mass of its stars, it has been placed a lower limit on the mass of the stars that have already experienced a SN explosion (and so potentially magnetar progenitors), resulting in $M_{\rm i} \gtrsim 40\,M_{\odot}$ (see Muno et al., 2006, and references therein). Searching for fast runaway stars, eventually ejected in the SN explosion of the magnetar progenitor, Clark et al. (2014) state to have identified in the Wolf-Rayet star WD1-5 the pre-SN companion of CXOU J1647-45. According to their model, the magnetar progenitor would have lost a substantial amount of mass in its Wolf-Rayet phase, and the common envelope phase could have prevented the spindown of the core. Therefore, this scenario would explain the mechanism for which such massive stars did not evolve in a BH, giving rise, instead, to magnetars.

1.4.2 Twisted magnetosphere

The huge internal magnetic field of magnetars is believed to be highly wound up. In fact, purely poloidal fields have been shown to be unstable (see e.g. Tayler, 1973; Flowers & Ruderman, 1977; Van Assche et al., 1981), so a toroidal component should be present and, in the case of magnetars, it is of the same order, or stronger, than the poloidal one (Braithwaite, 2009). Regardless of its still largely unexplored geometry (see §1.3.1), the internal field can influence the conductive surface, where the external magnetic field lines are anchored, by exerting an intense Lorentz force. In normal NSs, this force can be balanced by the rigidity of the crust, that depends on its composition and structure (Reisenegger & Goldreich, 1992). However, for ultra strong magnetic fields ($\approx 10^{14} - 10^{15}$ G, as in the case of magnetars), the internal stresses are strong enough to displace single surface elements, deforming the crust and giving rise to the so-called "starquakes" (see §1.3.3). In this way, starting from a purely dipolar configuration, also the external field will acquire a toroidal component, becoming twisted (Thompson et al., 2002). Twists are most likely localized into bundles of field lines, anchored in the regions which underwent a relative displacement (Beloborodov, 2009). However, the model formulated by Thompson et al. (2002) and adopted in this work is based on the simplifying assumption of a global twist (see Figure 1.6).

For a purely dipolar field (as in the case of standard PSRs, see §1.1), the potential field configuration implies $\boldsymbol{\nabla} \times \boldsymbol{B} = 0$, so that no currents can flow along the closed field lines and charged particles can stream only along the open field lines (the Goldreich-Julian currents, see Goldreich & Julian, 1969). The twisted magnetic field of magnetars, instead, is non potential, implying that

$$\boldsymbol{\nabla} \times \boldsymbol{B} = \frac{4\pi}{c} \boldsymbol{j}_{\rm B}\,. \tag{1.6}$$

Hence charged particles must populate the magnetosphere, flowing also along the closed field lines and corotating with the star at the same angular velocity $\boldsymbol{\Omega}$. In fact, neglecting all the non-electromagnetic forces (i.e. centrifugal, gravitational and collisional terms) with respect to the electromagnetic ones, the force equilibrium equation takes the form

$$\rho \boldsymbol{E} + \frac{\boldsymbol{j}_{\rm B} \times \boldsymbol{B}}{c} = 0\,, \tag{1.7}$$

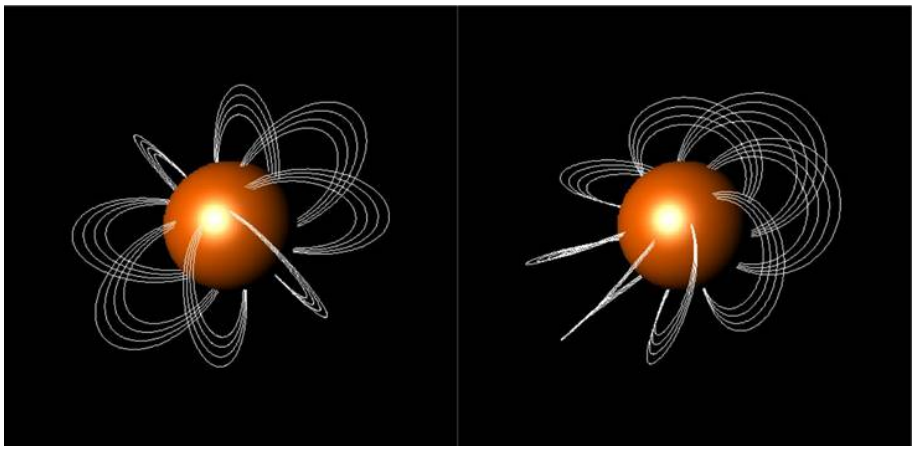

Figure 1.6: Closed magnetic field lines drawn in the case of a dipolar (left-hand panel) and a globally twisted (right-hand panel) magnetic fields (Turolla et al., 2015).

where ρ is the charge density and $\boldsymbol{E} = -(\boldsymbol{\Omega} \times \boldsymbol{r}) \times \boldsymbol{B}/c$ is the electric field generated by the star rotation at the position $\boldsymbol{r}$. However, magnetars are slow rotators, as pointed out in section 1.3, and assuming a low-density plasma one can neglect also the first term of equation (1.7)[3]. So it reduces simply to $\boldsymbol{j}_{\rm B} \times \boldsymbol{B} = 0$, that constraints the current $\boldsymbol{j}_{\rm B}$ to flow parallel to the magnetic field. Using equation (1.6), one finally obtains the force-free condition:

$$(\boldsymbol{\nabla} \times \boldsymbol{B}) \times \boldsymbol{B} = 0\,. \tag{1.8}$$

A formal solution of equation (1.8) is given by

$$\boldsymbol{\nabla} \times \boldsymbol{B} = \alpha(\mathcal{P})\boldsymbol{B}\,, \tag{1.9}$$

where α is a function of the flux parameter $\mathcal{P}(r, \theta)$, which characterizes in turn the poloidal component of the twisted magnetic field. In fact, assuming an axisymmetric magnetosphere, one can write the external magnetic field as the sum of its poloidal and toroidal components

$$\boldsymbol{B} = \frac{\boldsymbol{\nabla}\mathcal{P} \times \hat{\phi}}{r \sin\theta} + B_\phi\, \hat{\phi}\,, \tag{1.10}$$

where r is the radial distance from the star, θ the magnetic colatitude and $\hat{\phi}$ is the unit vector in the azimuthal direction. Restricting to self-similar solutions (see Wolfson, 1995; Thompson et al., 2002), i.e. such that

$$\mathcal{P} = \frac{1}{2} B_{\rm pol} R_{\rm NS}^2 \left(\frac{r}{R_{\rm NS}}\right)^{-p} f(\mu) \tag{1.11}$$

and

$$\alpha(\mathcal{P}) = \frac{C^{1/2}}{R_{\rm NS}} \left(\frac{p+1}{p}\right)^{1/2} \left(\frac{2\,\mathcal{P}}{B_{\rm pol} R_{\rm NS}}\right)^{1/p}\,, \tag{1.12}$$

[3]Actually, taking into account the effects of slow rotation only induces an additional twist of the magnetic field lines closer to the light cylinder $R_{\rm lc} \equiv cP/2\pi$, where the closed field lines are forced to open; this translates in a modest increase of the charge density, by $\rho_{\rm rot} \sim [\boldsymbol{\Omega} \cdot (\boldsymbol{r} \times \boldsymbol{j}_{\rm B})]/c^2$ (see Thompson et al., 2002).

where $B_{\rm pol}$ is the field intensity at the magnetic poles and $\mu \equiv \cos\theta$, equation (1.9) gives

$$B_\phi = \frac{p}{p+1}\frac{\mathcal{P}\alpha(\mathcal{P})}{r\sin\theta}\,. \tag{1.13}$$

Substituting equations (1.11)–(1.13) in equation (1.10), one obtains the expression of the globally twisted magnetic field in polar components:

$$\boldsymbol{B} = \frac{1}{2}B_{\rm pol}\left(\frac{r}{R_{\rm NS}}\right)^{-2-p}\left[-\frac{{\rm d}f}{{\rm d}\mu}, \frac{pf}{\sin\theta}, \frac{f^{1+1/p}}{\sin\theta}\left(\frac{Cp}{p+1}\right)^{1/2}\right]. \tag{1.14}$$

Here the function $f(\mu)$ satisfies the Grad-Shafranov equation

$$(1-\mu^2)\frac{{\rm d}^2 f}{{\rm d}\mu^2} + p(p+1)f + Cf^{1+2/p} = 0 \tag{1.15}$$

with the three boundary conditions ${\rm d}f/{\rm d}\mu = 0$ at $\mu = 0$, ${\rm d}f/{\rm d}\mu = -2$ and $f(1) = 0$ at $\mu = 1$, so that $B_r = 0$ at the magnetic equator and $B = B_r = B_{\rm pol}$ at the magnetic pole. The eigenvalue C is then fully determined by the radial index p.

Using the field line parametric equations, one can define the twist angle $\Delta\phi$, which measures the displacement between the footpoints of a single field line:

$$\Delta\phi = \int_{\theta_1}^{\theta_2}\frac{B_\phi}{\sin\theta B_\theta}{\rm d}\theta\,, \tag{1.16}$$

with θ_1 and θ_2 the magnetic colatitudes of the two footpoints. For the globally twisted magnetic field (1.14) it results:

$$\Delta\phi_{\rm N-S} = 2\sqrt{\frac{C}{p(p+1)}}\lim_{\mu\to 1}\int_0^\mu \frac{f(\mu')^{1/p}}{1-\mu'^2}{\rm d}\mu'\,. \tag{1.17}$$

Equation (1.17) correctly reduces to $\Delta\phi_{\rm N-S} = 0$ for $p = 1$ ($C = 0$), that correspond to a purely dipolar field, while $\Delta\phi_{\rm N-S} \to \pi$ for the (unphysical) configuration of the split monopole, with $p = 0$.

1.4.3 Magnetospheric currents

A twist of the magnetic field requires currents flowing along the closed field lines, sustained by charged particles directly extracted from the star surface. However, if the twist were constant in time (and so $\partial\boldsymbol{B}/\partial t = 0$), the electric field would be orthogonal to the magnetic field, and there would be no force able to lift the charges against the huge gravitational force of the star ($g_{\rm NS} \approx 10^{14}$ cm s^{-2} for typical values). Hence the twist shall decay, providing an electric field component $E_\parallel$ parallel to the magnetic field, that is maintained by self-induction:

$$\frac{\partial \boldsymbol{E}_\parallel}{\partial t} = 4\pi(\boldsymbol{j}_{\rm B} - \boldsymbol{j})\,. \tag{1.18}$$

Thus, when the conduction current j is smaller than the required current $j_{\rm B}$, the electric field $E_\parallel$ increases, at the expenses of the magnetic energy:

$$\frac{\partial}{\partial t}\left(\frac{B_\phi^2}{8\pi}\right) = -E_\parallel j\,. \tag{1.19}$$

On the contrary, if j becomes greater than $j_{\rm B}$ the system respond reducing the electric field $E_\parallel$, in order to maintain the quasi-equilibrium condition $j \simeq j_{\rm B}$.

In the simple approximation of a NS with a light-element surface (see Thompson et al., 2002), one can assume that the current j is sustained by electrons and ions, flowing in opposite directions so as to ensure charge neutrality. As pointed out by Beloborodov & Thompson (2007), in these conditions the circuit along the single field line can be approximated with a relativistic double layer, in which electrons are accelerated by a potential drop Φ applied between the field line footpoints, up to Lorentz factors $\gamma_{\rm e} \approx 1 + e\Phi/m_{\rm e}c^2$ (with e the electron charge). Since in order to lift the charged particles against gravity extremely high values of Φ (and $E_\parallel$) are required ($\approx 10^{12}$ GeV), the corresponding Lorentz factor for the accelerated electrons comes out to be huge ($\gamma_{\rm e} \approx 10^9$) and the twist would decay very rapidly. However, such high values for Φ and $\gamma_{\rm e}$ are prevented by the occurrence of pair production. In fact, 1 keV thermal photons emitted from the star surface can be up-scattered by magnetospheric electrons at energies $\gtrsim 1$ MeV, above the threshold for the creation of electron-positron pairs. In the presence of sufficiently strong magnetic fields, this process already takes place for $\gamma_{\rm e} \approx 10^3$ (see e.g. Nobili, Turolla & Zane, 2011). Thus, the resulting pair plasma screens the self inducted electric field, so that the potential Φ can take much smaller values than those expected in the double layer approximation, avoiding the fast decay of the twist. The full model of magnetospheric currents including the presence of pairs (see e.g. Beloborodov & Thompson, 2007) is, however, too complicated to be used in spectral simulations. Moreover, electrons and positrons would flow at highly relativistic velocities, and no self-consistent solutions can be obtained considering a mildly relativistic pair plasma, while the model can reproduce the observed soft X-ray tails if charged particles are mildly relativistic (see §1.3.1). For these reasons hereafter calculations will be carried out in the electron-ion approximation.

An estimate of the twist decay time $t_{\rm dec}$ can be derived from the ratio $\Delta E_{\rm B}/L_{\rm X}$ (Thompson et al., 2002), with $\Delta E_{\rm B}$ the excess of energy of a twisted field over a dipolar one,

$$\Delta E_{\rm B} = E_{\rm B} - E_{\rm B}^{\rm dip} \simeq 1.4\times10^{44}\,\Delta\phi_{\rm N-S}^2 \left(\frac{B_{\rm pol}}{10^{14}\,{\rm G}}\right)^2 \left(\frac{R_{\rm NS}}{10\,{\rm km}}\right)^2 {\rm erg}\,, \tag{1.20}$$

and $L_{\rm X}$ the rate of dissipated energy assuming that the current j is sustained by electrons and ions lifted by a minimum voltage $e\Phi \sim g_{\rm NS}R_{\rm NS}m_{\rm p}$,

$$\begin{aligned} L_{\rm X} &= \frac{GM_{\rm NS}m_{\rm p}B_{\rm pol}c}{2e}\frac{pf(\pi/2)}{2+p}\left(\frac{B_\phi}{B_\theta}\right)_{\theta=\pi/2} \\ &\simeq 3\times10^{35}\left(\frac{B_{\rm pol}}{10^{14}\,{\rm G}}\right)\left(\frac{M_{\rm NS}}{1.4\,M_\odot}\right)\left(\frac{B_\phi}{B_\theta}\right)_{\theta=\pi/2} {\rm erg\,s^{-1}}\,, \end{aligned} \tag{1.21}$$

with $m_{\rm p}$ the proton mass. Interestingly, despite all the simplifications assumed, the dissipation rate obtained in the previous equation is comparable with the observed values for the magnetar persistent X-ray emission (see §1.3.1). Putting together equations (1.20) and (1.21) it results

$$t_{\rm dec} = \frac{\Delta E_{\rm B}}{L_{\rm X}} \simeq 40\,\Delta\phi^2_{\rm N-S} \left(\frac{L_{\rm X}}{10^{35}\,{\rm erg\,s^{-1}}}\right)^{-1} \left(\frac{B_{\rm pol}}{10^{14}\,{\rm G}}\right)^{2} \left(\frac{R_{\rm NS}}{10\,{\rm km}}\right)^{3} {\rm yr}\,. \tag{1.22}$$

Since the presence of an electron-positron plasma is needed to sustain the twist for a sufficiently long time, the value of $L_{\rm X}$ will be reduced considering pairs, and $\tau_{\rm dec}$ will correspondingly increase.

1.4.4 Resonant cyclotron scattering

Due to the currents that flow along the closed magnetic field lines, the charged particle density in the magnetosphere of a magnetar is much greater than for the other kind of NSs. In particular, once the magnetic field structure is known, the spatial density $n_{\rm e}$ of the magnetospheric particles follows from the requirement $j = j_{\rm B}$ (Nobili, Turolla & Zane, 2008a),

$$n_{\rm e} = \frac{p+1}{4\pi e}\left(\frac{B_\phi}{B_\theta}\right)\frac{B}{r|\langle\beta\rangle|}\,, \tag{1.23}$$

where $\langle\beta\rangle$ is the average charge velocity in units of the speed of light. Such an electron density is large enough to make the magnetosphere optically thick for resonant cyclotron scattering (RCS). Thermal photons of energy $E = \hbar\omega$ coming from the star surface will scatter onto the magnetospheric electrons as soon as the resonance condition is satisfied:

$$\omega = \omega_{\rm D} \equiv \frac{\omega_{\rm B}}{\gamma(1-\beta\cos\theta_{\rm Bk})}\,, \tag{1.24}$$

where $\omega_{\rm B} = eB/m_{\rm e}c$ is the electron rest-frame cyclotron frequency, $m_{\rm e}$ is the electron mass and $\theta_{\rm Bk}$ is the angle between the incident photon direction and the particle velocity β.

In fact, when the electron cyclotron energy $\hbar\omega_{\rm B}$ is comparable with both the Fermi energy $\epsilon_{\rm F}$ and characteristic thermal energy $k_{\rm B}T$, Landau quantization become important (Landau, 1930): electron motion perpendicularly to the magnetic field is restricted into a set of cylindrical Landau levels, while charges are free to stream parallel to it. In particular, since in the case of magnetars $\hbar\omega_{\rm B}$ quite exceeds both $\epsilon_{\rm F}$ and $k_{\rm B}T$, electrons can be considered to reside mainly in the ground Landau state and, in the interaction with resonant photons, they are excited to the first Landau level. Since the lifetime of an excited Landau level

$$\Delta t_{\rm L} \approx 3\times10^{-14}\left(\frac{B}{10^{11}\,{\rm G}}\right)^{-2}\,{\rm s}\,, \tag{1.25}$$

is very small for magnetar-like fields (Fernàndez & Davis, 2011), the absorption and reemission process is pratically istantaneous and can be considered as a single scattering process.

From the resonance condition, it follows that RCS for typical 1 keV photons occurs at $B \approx 10^{11}$ G. Deriving the intensity of the twisted magnetic field from equation (1.14) and solving for r, one can obtain an estimate of the distance $r_{\rm res}$ from the star at which the resonance condition for a photon of energy E is reached

$$r_{\rm res} = R_{\rm NS}\left[\frac{1}{2}\left(\frac{B_{\rm pol}}{10^{11}\,{\rm G}}\right)\left(\frac{E}{1\,{\rm keV}}\right)F(\theta,p)\right]^{1/2+p}, \tag{1.26}$$

where $F(\theta,p)$ is given by (see equation 1.14)

$$F(\theta,p) = \left[\left(\frac{{\rm d}f}{{\rm d}\mu}\right)^2 + \frac{p^2 f^2}{\sin^2\theta} + \frac{C p f^{2+2/p}}{(p+1)\sin^2\theta}\right]^{1/2}. \tag{1.27}$$

Considering for the sake of simplicity a dipolar topology, with a polar magnetic field strength $B_{\rm pol} \approx 10^{14}$ G, equation (1.26) returns a distance $r_{\rm res} \simeq 8\,R_{\rm NS}$. If the scattering centres are, instead, ions, a similar calculation leads to $r_{\rm res} \approx 2\,R_{\rm NS}$. Actually, ions are much heavier than electrons, so that they are lifted from the star surface at much smaller heights. Moreover, for the ultra strong magnetic field of magnetars, also the Landau quantization of ions should be taken into account (see Potekhin, 2014, and references therein). Therefore photons can resonantly scatter also onto ions, but the effects of these interactions on the spectrum are expected to be negligible, except for the occurrence of narrow absorption lines at the ion cyclotron energy (see e.g. Tiengo et al., 2013; Borghese et al., 2015). For this reason, the electron-ion model of the magnetospheric currents is called "uni-directional flow" model, referring only to the contribution of electrons, that stream from one magnetic pole to the other. On the other hand, models that take into account magnetospheric currents sustained by electron-positron pairs are called "bi-directional flow" models, since in this case the effects of both the species of particles, flowing along the closed field lines in opposite directions, are equally relevant.

As discussed in section 1.3.1, RCS has been invoked to explain the non-thermal components of magnetar X-ray spectra. Cooling photons undergo multiple scatterings in the magnetosphere, where their frequences match the resonance condition (1.24); thus, up-scattered photons fill the high-energy part of the spectrum, giving rise to the observed power-law tails. However RCS also influences the polarization state of seed photons. As it will be discussed in the next chapter, photons emitted from a magnetar are expected to be linearly polarized in two normal modes, ordinary (O) and extraordinary (X). When photons scatter off electrons, their polarization states can change. The full expression of the cross section is very complex, but it can be substantially simplified assuming a series of suitable approximations. First of all, considering mildly relativistic particles, the electron recoil can be neglected for photon energies E up to some tens of keV (see Nobili, Turolla & Zane, 2008a), and $\sigma_{\rm res}$ becomes the (non relativistic) magnetic Thomson cross-section. Furthermore, since electrons can be considered in the Landau ground state before scattering, calculations can be carried out in the limit of electrons initially at rest. Finally, near to the resonance the natural width $\Gamma = 4e^2\omega_{\rm B}^2/3m_{\rm e}c^3$ of the first cyclotron line is very small, and one can take the limit $\Gamma \to 0$ (Nobili, Turolla & Zane, 2008a):

$$\lim_{\Gamma\to 0}\frac{\Gamma}{(\omega-\omega_{\rm B})^2+\Gamma^2/4} = 2\pi\delta(\omega-\omega_{\rm B})\,. \tag{1.28}$$

Performing the calculation in the stellar rest frame, it comes out that the total cross sections for photons with different initial/final polarization states are given by

$$\begin{aligned} \sigma_{\mathrm{O-O}} &= \frac{1}{3}\sigma_{\mathrm{O-X}} = \frac{\pi^2 e^2}{2m_e c}\delta(\omega-\omega_{\mathrm{D}})\cos\vartheta \\ \sigma_{\mathrm{X-X}} &= 3\sigma_{\mathrm{X-O}} = \frac{3\pi^2 e^2}{2m_e c}\delta(\omega-\omega_{\mathrm{D}})\,, \end{aligned} \tag{1.29}$$

where $\cos\vartheta = (\cos\theta_{\mathrm{Bk}}-\beta)/(1-\beta\cos\theta_{\mathrm{Bk}})$ is the cosine of the angle between the incident photon propagation direction and the electron velocity in the stellar rest frame. As shown by equations (1.29), the probability that a photon resonantly scattered by a magnetospheric electron emerges in the extraordinary mode is greater than for the ordinary mode.

1.5 Models of surface emission

The properties of thermal radiation emitted by magnetized NSs are influenced by the state of their surface and magnetosphere. According to the standard scenario, NSs are covered by a thin layer of a gaseous atmosphere, with typical scale height ~ 10 cm and density $0.1-10$ g/cm^3 (see e.g. Zavlin, 2009). Its composition is determined by either the fall-back of debris coming from the surrounding SNR or accretion mechanisms, e.g. from stellar companions or the interstellar medium. In the case of INSs, where these accretion phenomena are stopped very soon after the star formation, the strong surface gravity ($g_{\mathrm{NS}} \approx 10^{14}$ cm s^{-2}) causes the settling of heavy elements within short timescales (Brown et al., 1998; Lloyd, 2003), so that the atmosphere can be considered as made by light elements. For the expected densities and temperatures the atmosphere is optically thick, so that surface emission can be substantially modified.

1.5.1 Atmospheric emission models

Modeling the structure of a NS magnetized atmosphere is based on the theory of the propagation in the magnetized plasma of electromagnetic waves, that, in the presence of strong magnetic fields, are polarized in two normal modes, the ordinary and the extraordinary one (see chapter 2). The starting point is the calculation of the opacities for the photons polarized in both modes, which depend in general on the atmospheric plasma properties and on the magnetic field geometry. Since the first complete work, by Gnedin & Pavlov (1974), several other methods have been developed for the study of both fully ionized (see e.g. Zavlin, 2009, and references therein) and partially ionized (see e.g. Potekhin et al., 2004; Ho & Lai, 2004; Ho et al., 2008) atmospheres. In the following, I will discuss the model by Lloyd (2003, see also Lloyd et al. 2003) for the simple case of a pure hydrogen, fully ionized atmosphere, described by a semi-infinite, plane parallel geometry.

The model atmosphere is characterized by the star surface gravity g_{NS} and effective temperature T_{eff}, as well as the stellar magnetic field strength and direction and the plasma composition. Since conductive transport and convection are inefficient at the typical atmospheric densities and in strong magnetic fields, the energy transport in a

magnetized NS atmosphere is due only to photons, and is described by the radiative transfer equation

$$\mu_{\rm k}\frac{{\rm d}I_\nu}{{\rm d}\tau_\nu} = I_\nu - S_\nu\,; \tag{1.30}$$

here $\mu_{\rm k} = \cos\theta_{\rm k}$ is the cosine of the angle between the photon propagation direction $\boldsymbol{k}$ and the surface normal $\boldsymbol{n}$, I_ν is the (total) specific intensity and ${\rm d}\tau_\nu$ is the infinitesimal optical depth. The source function S_ν contains all the information about the photon-plasma interactions: in the case of a fully ionized, light-element atmosphere these processes are chiefly free-free emission and absorption and (magnetic) Thompson scattering (see Zavlin, 2009, for further details).

Since the atmosphere is assumed to be in hydrostatic equilibrium,

$$\frac{{\rm d}P}{{\rm d}z} = -\rho g_{\rm NS}\,, \tag{1.31}$$

where z is the vertical coordinate (along the surface normal) and the total pressure P accounts for the contributions of radiation and plasma, assumed as an ideal gas:

$$P = P_{\rm rad} + P_{\rm plasma}\,. \tag{1.32}$$

Possible non-ideal effects, that can arise from the interactions between the atmospheric plasma components, are also taken into account; in the case at hand, of a fully ionized, pure hydrogen plasma, the typical non-ideal contribution is given by the Coulomb interaction:

$$P_{\rm plasma} = P_{\rm ideal} + P_{\rm Coul} = \left(N - \frac{1}{2}n_{\rm e}\right)k_{\rm B}T - \frac{2e^3}{3}\left(\frac{2\pi}{kT}\right)^{1/2}(\bar{\alpha}n_{\rm e})^{3/2}\,, \tag{1.33}$$

where N is the total number density, $n_{\rm e}$ is the electron number density, T is the plasma temperature and $\bar{\alpha} \approx 1$ is a parameter that weakly depends on the chemical composition (see Lloyd, 2003).

Finally, in the absence of heat sources or sinks, the total flux propagating through the atmosphere

$$F = \sigma_{\rm SB}T_{\rm eff}^4\,, \tag{1.34}$$

where $\sigma_{\rm SB}$ is the Stefan-Boltzmann constant, has to be conserved. This translates in the radiative equilibrium condition (i.e. the total flux gradient has to be zero), that can be expressed by integrating the radiative transfer equation (1.30) over all the photon frequencies and angles,

$$\int_0^\infty {\rm d}\nu \int_\Omega \left[\frac{1}{2}\alpha_\nu\left(I_\nu^{\rm out} + I_\nu^{\rm in}\right) - j_\nu^{\rm th}\right] = 0\,, \tag{1.35}$$

where α_ν is the (total) monochromatic absorption coefficient, $j_\nu^{\rm th}$ is the thermal monochromatic emissivity and $I_\nu^{\rm in}$ ($I_\nu^{\rm out}$) is the specific monochromatic intensity of the incoming (outcoming) photons. This set of equatons are eventually complemented by the equation of state for the fully ionized atmospheric medium. Further details about the model and its predictions are discussed in chapter 5.

1.5.2 Condensed surface emission models

Strong magnetic fields also modify the properties of matter. The typical scale B_0 above which the magnetic effects on matter become important is given by equating the electron cyclotron energy $\hbar\omega_B$ to the characteristic energy of a bound electron e^2/a_0:

$$B_0 = \frac{m_{\rm e}^2 e^3 c}{\hbar^3} = 2.3505 \times 10^9\,{\rm G}\,, \tag{1.36}$$

where $a_0 = \hbar/m_{\rm e}c\alpha_{\rm F}$ is the Bohr radius and $\alpha_{\rm F}$ is the fine structure constant. While in the weak field regime ($B \ll B_0$) an external magnetic field can be treated as a small perturbation to the electric forces that act inside the atoms (e.g. giving origin to the Zeeman level splitting), for magnetar-like field strengths the opposite holds and Coulomb forces behave as a perturbation. Due to the Landau quantization of the electron motion in the direction perpendicular to the magnetic field (see §1.4.4), atoms are stretched in cylindrical shapes along $\boldsymbol{B}$. Thus, for sufficiently low temperatures, they bind each other in molecular chains through covalent bonding, forming three-dimensional condensates (Lai, 2001; Zane et al., 2002b; Turolla et al., 2004; Medin & Lai, 2006).

This mechanism, called "magnetic condensation", was firstly exploited in NS models to explain the spectra of some peculiar sources belonging to the class of XDINSs (see Zane et al., 2002b). As pointed out in section 1.2, emission from XDINSs is characterized by a thermal spectrum, with some absorption lines explained with the presence of a gaseous atmosphere above the surface. Nevertheless, CHANDRA and XMM-Newton observations of the radiation emitted by the XDINS RX J1856.5-3754 revealed a purely thermal spectrum, without any absorption feature (Burwitz et al., 2001; Paerels et al., 2001; Zane et al., 2002a). Magnetic condensation can indeed explain this phenomenology: since XDINSs are quite magnetized NSs, if the temperature is smaller than a critical limit $T_{\rm crit}$ a phase transition can occur in the gaseous atmosphere, leaving bare the star surface. Thus the emission from the condensed surface is directly observed and no absorption features are expected. Actually, it has been suggested that some XDINSs may have a thin atmospheric layer above the condensed surface (different from the magnetized atmosphere discussed above), which is optically thick at the lower photon energies and optically thin at the higher ones (Suleimanov et al., 2009, see also Motch et al. 2003; Ho et al. 2007); nonetheless the effects of this kind of atmospheres are not discussed in the following.

The values of $T_{\rm crit}$ are in general different for different chemical compositions. Lai & Salpeter (1997, see also Lai 2001) firstly derived an estimate for $T_{\rm crit}$ in the case of hydrogen

$$T_{\rm crit}^{\rm H} \approx 0.1\,Q_\infty\,, \tag{1.37}$$

where the cohesive energy Q_∞ is given by

$$\begin{aligned} Q_\infty &\approx 194.1\left(\frac{B}{10^{12}\,{\rm G}}\right)^{0.37} - 4.4\left[\ln\left(\frac{B}{10^{12}\,{\rm G}}\right) - 6.05\right]^2 \\ &- \hbar\omega_{\rm p,p} - \frac{\hbar}{2}\left(\omega_{\rm B,p}^2 - \omega_{\rm p,p}^2\right)^{1/2} + \frac{1}{2}\hbar\omega_{\rm B,p}\,{\rm eV}\,, \end{aligned} \tag{1.38}$$

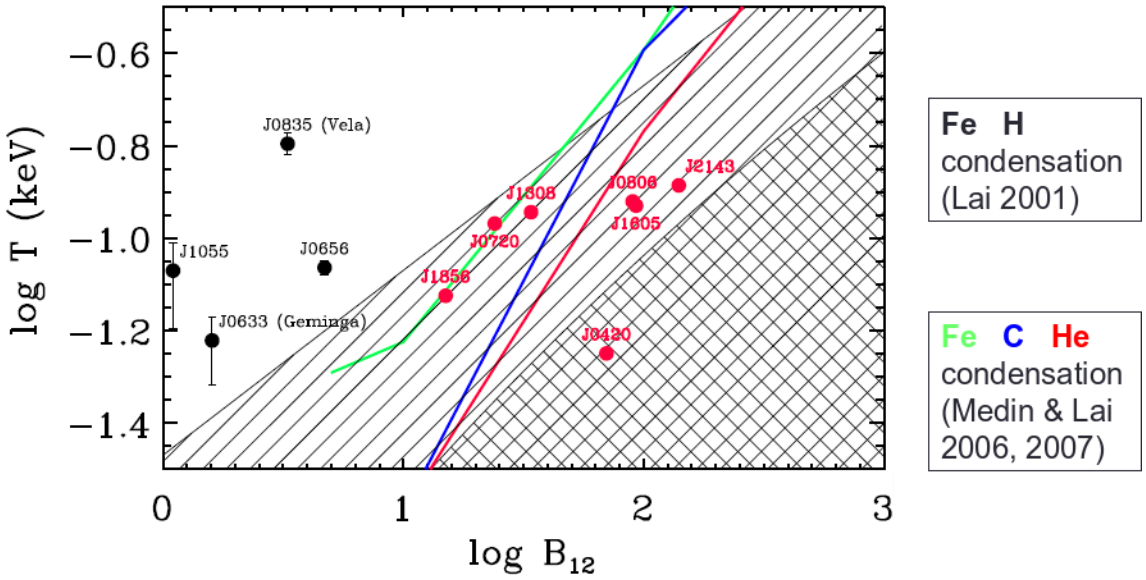

Figure 1.7: Temperature T as a function of the magnetic field strength $B_{12} = B/10^{12}$ G at which the magnetic condensation is allowed for iron (hatched region) and hydrogen (cross-hatched region), according to the model by Lai (2001). The color curves correspond to the models for $T_{\rm crit}(B_{12})$ developed by Medin & Lai (2006, 2007) for iron (green), carbon (blue) and helium (red). The black points with error bars represent the measured values of surface temperature and magnetic field strength for PSR J0835-4510 (Vela), PSR J0656-5449, PSR J0633+1746 (Geminga) and PSR J1055-6032. The red points correspond to the seven XDINSs: RX J0720.4-3125, RX J1308.6+2127 (RBS 1223), RX J1856.5-3754, RX J0806.4-4123, RX J0420.0-5022, RX J1605.3+3249 and RX J2143.0+0654 (RBS 1774).

with $\omega_{\rm B,p}$ and $\omega_{\rm p,p}$ the proton cyclotron and plasma frequencies, respectively. An expression for the critical temperature in the case of heavier elements is, instead, more complicated. A comprehensive study carried out by Medin & Lai (2006, 2007), provided estimates for helium, carbon and iron:

$$T_{\rm crit} \approx 0.08\, Q_{\rm s}\,, \tag{1.39}$$

where, for atomic numbers $Z \gtrsim 10$, the cohesive energy of the three-dimensional condensate $Q_{\rm s}$ satisfies the relation (see Turolla et al., 2004, and references therein)

$$Q_{\rm s} \lesssim Z^{9/5} \left(\frac{B}{10^{12}\,{\rm G}}\right)^{2/5} {\rm eV}\,. \tag{1.40}$$

Figure 1.7, shows the behavior of $T_{\rm crit}$ as a function of the magnetic field strength according to the models by Lai (2001) and Medin & Lai (2007) for different compositions. The location in the $B-T$ plane of some INSs is also shown. The seven XDINSs (red points) are located in the region of the plot in which magnetic condensation is allowed for the different chemical compositions considered by the models. In particular, RX J1856.5-3754 (the source that shows the featureless spectrum) is placed just

along the curve $T_{\rm crit}(B)$ predicted by the model of Medin & Lai (2006, 2007) for an iron condensate. On the other hand, for the four pulsars on the left (black points), the temperature appears too high for the given magnetic field in order to allow any phase transition, so that the presence of a gaseous atmospheric layer seems unavoidable.

Models for the emission from the condensed surface of a bare NS have been developed by different authors (see e.g. Brinkmann, 1980; Turolla et al., 2004; van Adelsberg et al., 2005; Pèrez-Azorìn et al., 2005). In the following I use the analytical expressions derived by Potekhin et al. (2012) to fit the emissivity J_ν of a condensed iron surface. This is in turn related to the total monochromatic intensity I_ν by

$$I_\nu = J_\nu B_\nu = \frac{2hJ_\nu}{c^2} \frac{\nu^3}{\mathrm{e}^{h\nu/k_{\rm B}T} - 1}\,, \tag{1.41}$$

where B_ν is the Planck function. Potekhin et al. (2012) calculated the total emissivity J_ν in two different approximations, "fixed ions" (in which the ion response to the electromagnetic waves is neglected) and "free ions" (Coulomb interaction between the ions in the lattice are neglected and they are free to move). In the former limit the total emissivity takes different values depending on whether the photon energy E is smaller or greater than the ion cyclotron energy $E_{\rm ci} = \hbar Z_{\rm i} eB/m_{\rm i}c$ (in the case of iron $E_{\rm ci} \approx 29.4\,[B/10^{13}\,{\rm G}]$ eV):

$$J_\nu = \begin{cases} J_{\rm A} & \text{for } E < E_{\rm ci} \\ J_{\rm B}(1 - J_{\rm C}) + \dfrac{J_{\rm C}}{1+L} & \text{for } E \geq E_{\rm ci} \end{cases}\,, \tag{1.42}$$

Instead, the fixed ion approximation corresponds to the limit $E_{\rm ci} \to 0$, so that J_ν becomes simplier:

$$J_\nu = \tilde{J}_{\rm B}(1 - \tilde{J}_{\rm C}) + \frac{\tilde{J}_{\rm C}}{1+L}\,. \tag{1.43}$$

The expressions of all the auxiliary functions $J_{\rm A}$, $J_{\rm B}$, $J_{\rm C}$, $\tilde{J}_{\rm B}$, $\tilde{J}_{\rm C}$ and L are given in Potekhin et al. (2012, section 2); they depend in general on the surface magnetic field intensity B, the angle $\theta_{\rm B}$ between the magnetic field direction and the local normal to the star surface at the emission point, and the polar angles $\theta_{\rm k}$, $\phi_{\rm k}$ that individuate the photon propagation direction with respect to the local normal. As an example, Figure 1.8 shows the behavior of the total emissivity in both the free-ions and fixed-ions approximations, for an iron condensed surface, with $B = 10^{13}$ G, $\theta_{\rm B} = 45°$, $\phi_{\rm k} = 0°$ and different values of $\theta_{\rm k}$. It can be seen that the emissivities in the two limits are quite the same at higher energies, while they deviate at lower ones.

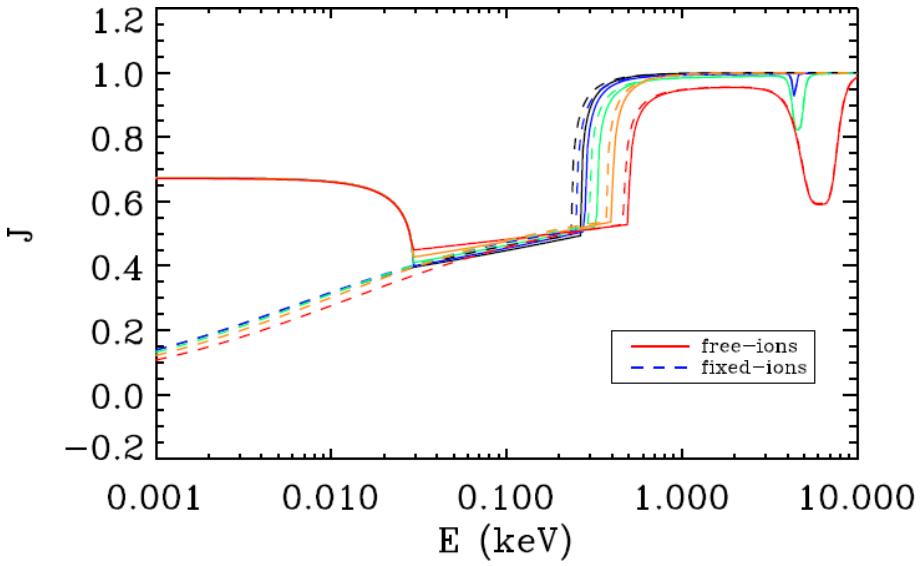

Figure 1.8: Total emissivity from an iron condensed surface obtained with the model developed by Potekhin et al. (2012) in the free ions (solid lines) and fixed ions (dashed lines) limits. Here the polar magnetic field strength is fixed at $B = 10^{13}$ G, $\theta_{\rm B} = 45°$, $\phi_{\rm k} = 0°$ and $\theta_{\rm k} = 0°$ (black), 15° (blue), 30° (green), 45° (orange) and 60° (red).

Chapter 2

Photon polarization in strong magnetic fields

Due to their strong magnetic fields, NSs emit highly polarized radiation. Polarization measurements can indeed improve our knowledge about these sources: in fact, in the case of some radio PSRs optical and radio polarimetry has been exploited to derive the incliniation of the rotation and magnetic axes with respect to the observer line-of-sight (Manchester & Taylor, 1977; Lyne & Manchester, 1988). No significant results, instead, have been obtained so far for the X-ray emission of strongly magnetized INSs like magnetars and XDINSs, due to the poor sensitivity of the past instrumentation. However, recent X-ray polarimetry missions, like XIPE [1] and IXPE [2], already selected for the study phase of the ESA M4 and NASA SMEX programmes, promise to open a new window in this field. In this chapter I describe the theoretical framework for the study of the polarization properties of magnetar and XDINS emission. This will be used in the next chapters for the construction of detailed models.

2.1 Polarization mode evolution

Photons emitted from the surface of high-B NSs and propagating through the magnetized plasma in their surroundings are expected to be linearly polarized in two normal modes: the ordinary mode (O), in which the electric field of the wave associated to the photon oscillates in the $\boldsymbol{k} - \boldsymbol{B}$ plane, with $\boldsymbol{k}$ the photon propagation direction and $\boldsymbol{B}$ the local magnetic field; and the extraordinary mode (X), in which, instead, the photon electric field oscillates perpendicularly to the $\boldsymbol{k} - \boldsymbol{B}$ plane. This holds, in particular, if the stellar magnetic field is strong enough to make the electron cyclotron energy, $\hbar\omega_{\rm B} \simeq 11.6\,(B/10^{12}\,{\rm G})\,{\rm keV}$, comparable or greater than the photon energy $\hbar\omega$ and in the further hypothesis that the latter is far enough away from the ion cyclotron energy $\hbar\omega_{\rm B,i}$ (Gnedin & Pavlov, 1974; Ho & Lai, 2003; Lai et al., 2010). It can be shown that, under these conditions, the X-mode opacity is strongly suppressed with respect to the

[1] http://www.isdc.unige.ch/xipe
[2] Weisskopf et al. (2013); Jahoda et al. (2015)

O-mode one according to

$$\kappa_{\rm X} \sim \left(\frac{\omega}{\omega_{\rm B}}\right)^2 \kappa_{\rm O}\,, \tag{2.1}$$

i.e. thermal surface radiation is probably more polarized in the X-mode. Nevertheless, the intrinsic polarization state of photons emitted from the star surface is not completely assessed as yet; in this respect, Beloborodov & Thompson (2007) noted that, in the case of magnetars, thermal emission from the surface regions heated by the returning currents should preferentially occur in the O-mode.

2.1.1 Dielectric and magnetic permeability tensors

Radiative processes that occur in the surface layers of a NS strongly influence the initial photon polarization state (as shown e.g. in §1.4.4 for RCS). However, in the presence of strong magnetic fields, polarization properties of photons can be modified also as they propagate in vacuo, thanks to the "vacuum polarization" effect. Ho & Lai (2003, see also Ginzburg 1970; Harding & Lai 2006) derived the full expression of the dielectric tensor $\boldsymbol{\epsilon}^{(\rm p)}$ for a cold, magnetized plasma composed by electrons and ions and traversed by an electromagnetic wave with electric field $\boldsymbol{E} = \boldsymbol{E}_0 {\rm e}^{-{\rm i}\omega t}$. They considered the electrons and ions interacting with a collision frequency $\nu_{\rm ei}$ and exchanging energy via radiative damping (with damping frequencies $\nu_{\rm re}$ and $\nu_{\rm ri}$, respectively). In a cartesian reference frame with the vertical axis chosen along $\boldsymbol{B}$, it results

$$\boldsymbol{\epsilon}^{(\rm p)} = \begin{bmatrix} \varepsilon & {\rm i}g & 0 \\ -{\rm i}g & \varepsilon & 0 \\ 0 & 0 & \Upsilon \end{bmatrix}\,, \tag{2.2}$$

where the expressions of ε, g and Υ are given by

$$\begin{aligned} \varepsilon \pm g &= 1 - \frac{1}{\omega}\frac{\omega_{\rm p}^2(\omega + {\rm i}\nu_{\rm ei}) + \omega_{\rm p,i}^2(\omega + {\rm i}\nu_{\rm re})}{(\omega + {\rm i}\nu_{\rm re} \pm \omega_{\rm B})(\omega + {\rm i}\nu_{\rm ri} \mp \omega_{\rm B,i}) + {\rm i}\omega\nu_{\rm ei}} \\ \Upsilon &\simeq 1 - \frac{1}{\omega}\left(\frac{\omega_{\rm p}^2}{\omega + {\rm i}(\nu_{\rm ei} + \nu_{\rm re})} - \frac{\omega_{\rm p,i}^2}{\omega + {\rm i}(\nu_{\rm ei} + \nu_{\rm ri})}\right)\,, \end{aligned} \tag{2.3}$$

with $\omega_{\rm p}$ and $\omega_{\rm p,i}$ the electron and ion plasma frequencies, respectively.

Vacuum polarization, instead, is an effect due to quantum electrodynamics (QED). Photons propagating in the strongly magnetized vacuum around NSs may convert into virtual electron-positron pairs; high-intensity external magnetic fields can polarize these pairs, modifying the components of the dielectric and magnetic permeability tensors of the vacuum, which would coincide with the unit tensor $\mathbb{1}$ otherwise. In particular, for photon energies far away from the electron rest energy it results (see Klein & Nigam, 1964; Adler, 1971)

$$\begin{aligned} \boldsymbol{\epsilon}^{(\rm v)} &= a\mathbb{1} + q\hat{\boldsymbol{B}}\hat{\boldsymbol{B}} \\ \bar{\boldsymbol{\mu}}^{(\rm v)} &= a\mathbb{1} + m\hat{\boldsymbol{B}}\hat{\boldsymbol{B}}\,, \end{aligned} \tag{2.4}$$

where $\bar{\boldsymbol{\mu}}$ indicates the inverse of the magnetic permeability tensor and $\hat{\boldsymbol{B}}$ is the local magnetic field unit vector. The coefficients a, q and m depend on the magnetic field intensity through the ratio $b = B/B_{\rm Q}$, where $B_{\rm Q} = m_{\rm e}^2 c^3/\hbar e \approx 4.414 \times 10^{13}$ G is the quantum critical field, i.e. the intensity for which the electron cyclotron energy equals the particle rest energy. Potekhin et al. (2004) derived some convenient fitting formulae that provide good approximations of a, q and m for any value of B:

$$\begin{aligned} a &\approx -\frac{2\alpha_{\rm F}}{9\pi} \ln\left(1 + \frac{b^2}{5}\frac{1 + 0.25487\, b^{3/4}}{1 + 0.75\, b^{5/4}}\right) \\ q &\approx \frac{7\alpha_{\rm F}}{45\pi} b^2 \frac{1 + 1.2\, b}{1 + 1.33\, b + 0.56\, b^2} \\ m &\approx -\frac{\alpha_{\rm F}}{3\pi} \frac{b^2}{3.75 + 2.7\, b^{5/4} + b^2}\,. \end{aligned} \tag{2.5}$$

In the weak field limit ($b \ll 1$) they reduce to the simple following expressions:

$$a = -2\delta\,, \qquad q = 7\delta\,, \qquad m = -4\delta\,, \tag{2.6}$$

where

$$\delta = \frac{\alpha_{\rm F}}{45\pi}\, b^2 \approx 3 \times 10^{-10} \left(\frac{B}{10^{11}\ {\rm G}}\right)^2\,. \tag{2.7}$$

Using expressions (2.6) in place of the full expressions gives a good approximation up to $B \approx 10^{14}$ G.

2.1.2 Vacuum resonance

The evolution of the photon electric field is governed by the wave equation

$$\boldsymbol{\nabla} \times (\bar{\boldsymbol{\mu}} \cdot \boldsymbol{\nabla} \times \boldsymbol{E}) = \frac{\omega^2}{c^2} \boldsymbol{\epsilon} \cdot \boldsymbol{E}\,. \tag{2.8}$$

According to Ho & Lai (see 2003), for $B \ll 5 \times 10^{16}$ G the total dielectric tensor $\boldsymbol{\epsilon}$ can be obtained by summing linearly the plasma and vacuum contributions (equations 2.2 and 2.4), resulting in

$$\boldsymbol{\epsilon} = \begin{pmatrix} \varepsilon' & {\rm i}g & 0 \\ -{\rm i}g & \varepsilon' & 0 \\ 0 & 0 & \Upsilon' \end{pmatrix}\,, \tag{2.9}$$

with $\varepsilon' = \varepsilon + a$ and $\Upsilon' = \Upsilon + a + q$. The inverse total magnetic permeability tensor $\bar{\boldsymbol{\mu}}$, instead, is still given by the second of equations (2.4). Solving the wave equation in a reference frame (x, y, z) with the z-axis along the photon propagation direction $\boldsymbol{k}$ and the x-axis in the plane that contains both $\boldsymbol{k}$ and $\boldsymbol{B}$, the unit vectors along which the electric field of O- and X-mode photons oscillates is

$$\hat{\boldsymbol{E}}_{\rm j} = \frac{1}{\sqrt{1 + K_{\rm j}^2 + K_{z,{\rm j}}}} \begin{pmatrix} {\rm i}K_{\rm j} \\ 1 \\ {\rm i}K_{z,{\rm j}} \end{pmatrix}\,, \tag{2.10}$$

where $K = -\mathrm{i}E_x/E_y$ is the mode ellipticity and $j = 0, 1$ for O-mode and X-mode photons respectively. It can be shown that the z component of $\boldsymbol{E}$ represents a longitudinal oscillation along the propagation direction, that does not propagate (Mèszàros, 1992). Moreover, since K_z results to be proportianal to the electron plasma frequency ω_p (which depends in turn on the plasma density ρ), in the limit of low densities $E_\mathrm{z} \simeq 0$ (see e.g. Ho & Lai, 2003). Hence, only the transverse modes, for which the photon electric field oscillates along the x and y directions, can be considered.

The ellipticity K is given by (see e.g. Ho & Lai, 2003; Harding & Lai, 2006)

$$K_\mathrm{j} = \beta_\mathrm{p} + (-1)^\mathrm{j}\sqrt{1 + \beta_\mathrm{p}^2 + \frac{m}{1+a}\sin^2\theta_\mathrm{Bk}}\,, \tag{2.11}$$

and it is fully determined by the polarization parameter β_p

$$\beta_\mathrm{p} = -\frac{\varepsilon'^2 - g^2 - \varepsilon'\Upsilon'(1+m/a)}{2g\Upsilon'}\frac{\sin^2\theta_\mathrm{Bk}}{\cos\theta_\mathrm{Bk}}\,, \tag{2.12}$$

with θ_Bk the angle between the photon propagation direction $\boldsymbol{k}$ and the local magnetic field $\boldsymbol{B}$. For general values of the photon energy $\hbar\omega$, it results $\beta_\mathrm{p} \gg 1$ so that $K_\mathrm{O} \sim 2\beta_\mathrm{p} \gg 1$ and $K_\mathrm{X} \sim 1/\beta_\mathrm{p} \ll 1$; hence, in this limit the two modes are linearly polarized in two mutually orthogonal directions, parallel and perpendicular to the $\boldsymbol{k} - \boldsymbol{B}$ plane, respectively. Nevertheless, at particular values of ω, $\beta_\mathrm{p} = 0$, so that $K_\mathrm{O}, K_\mathrm{X} \sim \pm 1$, i.e. photons are circularly polarized with different mode helicities. This is the so-called "vacuum resonance", that arises when the plasma and vacuum polarization effects compensate each other. In the limit of photon energies much smaller than the electron cyclotron energy and not too close to the ion cyclotron energy, the vacuum resonance occurs when

$$\omega = \frac{\omega_\mathrm{p}}{\sqrt{q+m}}\,, \tag{2.13}$$

that, with $\omega_\mathrm{p} = 4\pi n_\mathrm{e} e^2/m_\mathrm{e}$ (n_e is the electron number density), leads to a condition for the plasma density

$$\rho_\mathrm{V} \simeq 0.964\, Y_\mathrm{e}^{-1}\left(\frac{\hbar\omega}{1\,\mathrm{keV}}\right)^2\left(\frac{B}{10^{14}\,\mathrm{G}}\right)^2\lambda^{-2}\,\mathrm{g\,cm^{-3}}\,, \tag{2.14}$$

where Y_e is the plasma electron fraction and $\lambda \simeq 1$ is a slow varying function of B (see e.g. Harding & Lai, 2006). The polarization evolution of two photons, emitted with different modes from the NS surface and propagating close to the vacuum resonance, is sketched in Figure 2.1, where the photon energy is $\hbar\omega = 5$ keV, $\theta_\mathrm{Bk} = 45°$, $B_\mathrm{pol} = 10^{13}$ G and $Y_\mathrm{e} = 1$. For densities $\rho \gtrsim \rho_\mathrm{V}$, the plasma terms dominate and the normal modes are almost linearly polarized in the respective initial modes. As ρ decreases, the mode ellipticities approches 1, up to $\rho = \rho_\mathrm{V}$, where the modes are exactly circularly polarized (left-handed the ordinary photon and right-handed the extraordinary one). Crossing the vacuum resonance, the ordinary photon converts into an extraordinary one and vice versa, as long as their polarization becomes again linear at $\rho \lesssim \rho_\mathrm{V}$, where the vacuum polarization contributions dominate.

However, for magnetars and XDINSs, that are the main topic of this work, the density of the magnetospheric medium is well below the vacuum resonance. Also in

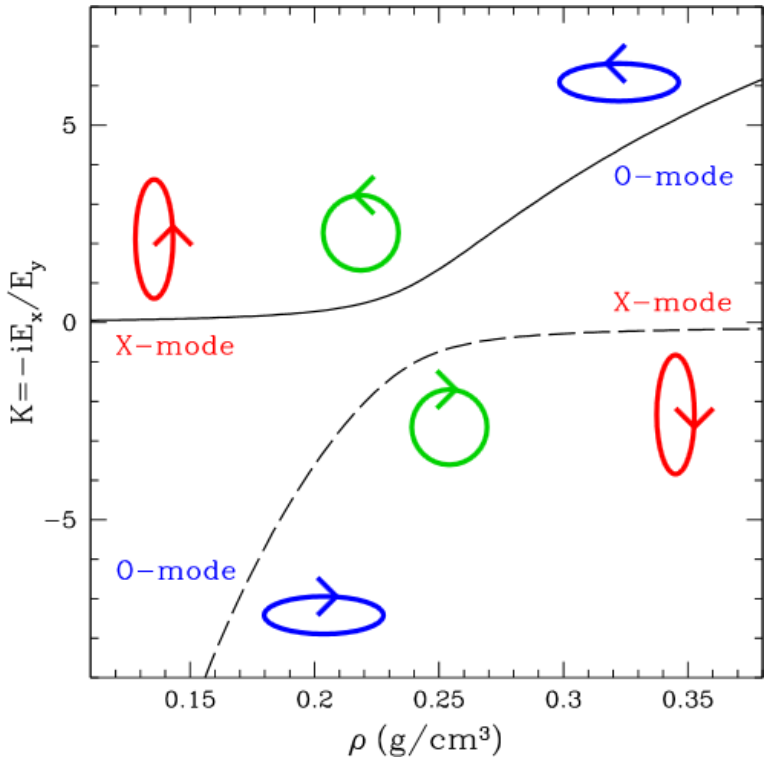

Figure 2.1: Mode ellipticity K, plotted as a function of the plasma density ρ close to the vacuum resonance, for two photons emitted in the O-mode (solid line) and in the X-mode (dashed line) respectively. Here $\hbar\omega = 5$ keV, $\theta_{\rm Bk} = 45°$, $B_{\rm pol} = 10^{13}$ G and $Y_{\rm e} = 1$ (Harding & Lai, 2006).

the cases in which the effects of gaseous atmospheres are discussed, only the radiation emerging from the photosphere is considered, so that it can be always taken $\rho \ll \rho_{\rm V}$ (see chapter 5). Moreover, as shown by Fernàndez & Davis (2011), the vacuum contributions to the dielectric tensor dominate with respect to the plasma ones up to $\sim 3000\, R_{\rm NS}$ under the typical conditions of magnetar and XDINSs magnetospheres. For these reasons, plasma contributions to the dielectric tensor will be neglected hereafter; photons emitted from the star surface will be always considered linearly polarized in either the O- or the X-mode, due to the effects of vacuum polarization.

2.2 Polarized radiative transfer in vacuo

In the reference frame (x, y, z) defined in the previous section, with the z-axis along the photon propagation direction $\boldsymbol{k}$ and the x-axis in the plane made by $\boldsymbol{k}$ and $\boldsymbol{B}$, the electric field associated with a photon of energy $\hbar\omega$ can be written as

$$\boldsymbol{E} = \boldsymbol{E}_0(z)\mathrm{e}^{-\mathrm{i}\omega t} = \boldsymbol{A}(z)\mathrm{e}^{\mathrm{i}(k_0 z - \omega t)}\,, \tag{2.15}$$

with

$$k_0 = \omega/c \simeq 5.1 \times 10^7 \left(\frac{\hbar\omega}{1\,\mathrm{keV}}\right)\ \mathrm{cm}^{-1} \tag{2.16}$$

and $\boldsymbol{A} = (A_x, A_y, A_z)$ is the electric field complex amplitude. In the limit of zero plasma density, the expressions for the mode unit vectors (2.10) simplifies to

$$\hat{\boldsymbol{E}}_{\rm O} = \begin{pmatrix} 1 \\ 0 \\ 0 \end{pmatrix} \qquad\qquad \hat{\boldsymbol{E}}_{\rm X} = \begin{pmatrix} 0 \\ 1 \\ 0 \end{pmatrix} , \tag{2.17}$$

so that for an O-mode (X-mode) photon emitted from the surface the only component of $\boldsymbol{A}$ different from zero will be A_x (A_y).

2.2.1 Vacuum polarization effects

Retaining only linear terms, the wave equation (2.8), where now $\boldsymbol{\epsilon} = \boldsymbol{\epsilon}^{(\rm v)}$, simplifies in the following equation system

$$\begin{aligned} \frac{{\rm d}A_x}{{\rm d}z} &= \frac{{\rm i}k_0\delta}{2}\left[MA_x + PA_y\right] \\ \frac{{\rm d}A_y}{{\rm d}z} &= \frac{{\rm i}k_0\delta}{2}\left[PA_x + NA_y\right] \\ A_{\rm z} &= -\frac{\epsilon_{zx}}{\epsilon_{zz}}A_x - \frac{\epsilon_{zy}}{\epsilon_{zz}}A_y\,. \end{aligned} \tag{2.18}$$

Here the adimensional coefficients M, N and P are suitable combinations of the dielectric and magnetic permeability tensor components; in the weak field limit ($b \ll 1$), they are given by (see e.g. Taverna et al., 2014)

$$\begin{aligned} M &= \frac{(7\hat{B}_x^2 + 4\hat{B}_y^2)\bar{\mu}_{xx} - 12\delta\hat{B}_x^2\hat{B}_y^2}{\bar{\mu}_{xx}\bar{\mu}_{yy} - 16\delta^2\hat{B}_x^2\hat{B}_y^2} \\ N &= \frac{(4\hat{B}_x^2 + 7\hat{B}_y^2)\bar{\mu}_{yy} - 12\delta\hat{B}_x^2\hat{B}_y^2}{\bar{\mu}_{xx}\bar{\mu}_{yy} - 16\delta^2\hat{B}_x^2\hat{B}_y^2} \\ P &= \frac{\left[3\bar{\mu}_{xx} - 4\delta\left(7\hat{B}_y^2 + 4\hat{B}_x^2\right)\right]\hat{B}_x\hat{B}_y}{\bar{\mu}_{xx}\bar{\mu}_{yy} - 16\delta^2\hat{B}_x^2\hat{B}_y^2}\,. \end{aligned} \tag{2.19}$$

The system (2.18) shows that a non-vanishing z component of the electric field arises due to vacuum polarization effects. As pointed out in section 2.1.2, this is a longitudinal oscillation, implying that these are not plane waves. Since it results $|A_z| \ll |A_x| \sim |A_y|$, i.e. the amplitude of this oscillation is vanishingly small and can be neglected.

Hence, the evolution of the polarization modes due to the QED effects is described by the first two differential equations of the system (2.18), from which it can be clearly seen that the typical length-scale $\ell_{\rm A}$ over which the complex amplitude varies is

$$\ell_{\rm A} \equiv \frac{2}{k_0\delta} \simeq 130\left(\frac{B}{10^{11}\,{\rm G}}\right)^{-2}\left(\frac{\hbar\omega}{1\,{\rm keV}}\right)^{-1}\,{\rm cm}\,, \tag{2.20}$$

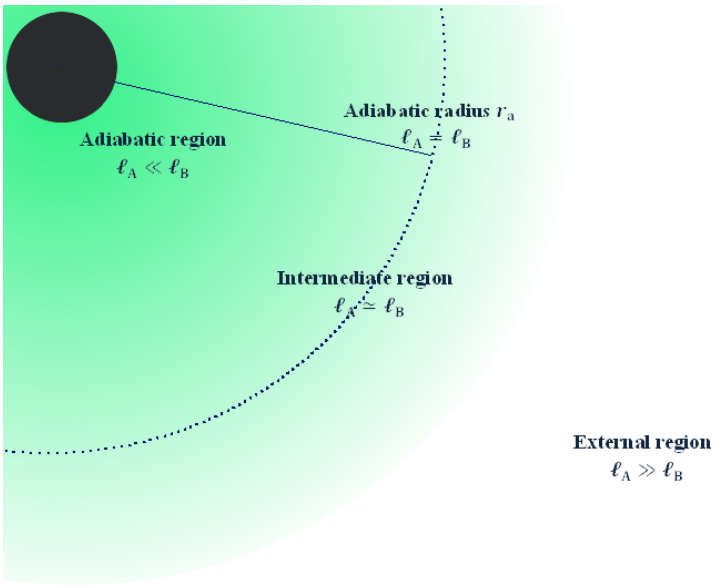

Figure 2.2: Representation of the three regions that characterize the polarization modes of photons propagating through the magnetized vacuum of high-B INSs (see text).The adiabatic radius r_a at which $\ell_A = \ell_B$ is also shown.

where equations (2.7) and (2.16) have been used. However, as the photon propagates, also the stellar magnetic field changes in both strength and direction, over a length-scale $\ell_B = B/|\boldsymbol{k} \cdot \boldsymbol{\nabla} B|$. In the general case of a twisted magnetic field with radial index p (see equation 1.14), it is $B \propto F(\theta, p) r^{-2-p}$, with $F(\theta, p)$ given by equation (1.27). Therefore, assuming for the sake of simplicity purely radial photon trajectories, it results

$$\ell_B = \frac{r}{2+p}\,, \tag{2.21}$$

and, in the simple case of a dipolar field ($p = 1$), one has $\ell_B = r/3$.

By comparing the two scale lengths ℓ_A and ℓ_B one can identify three propagation regions that characterize the polarization transfer (see Figure 2.2). In the internal region, where the magnetic field is stronger, $\ell_A \ll \ell_B$, implying that the photon electric field can adapt istantaneously its direction to that of the local magnetic field. Thus, a photon emitted either in the O- or in the X-mode maintains its initial polarization state: in these conditions the propagation is said to be adiabatic, and this zone is called the "adiabatic region" . Since in general $\ell_A \sim r^{4+2p}$, while $\ell_B \sim r$, as the photon propagates outwards there will be an intermediate region in which $\ell_A \simeq \ell_B$, where the photon electric field does not respond promptly to the variation of B. Finally, in the external region, where the magnetic field is weaker, $\ell_A \gg \ell_B$ and the photon electric field direction freezes; as a consequence, the polarization modes begin to change as the magnetic field direction varies along the photon trajectory.

It is convenient to introduce the "adiabatic radius" r_a, defined implicitly by the condition $\ell_A = \ell_B$ that roughly marks the boundary of the adiabatic region (see Taverna et al., 2015). Using equations (2.20) and (2.21) and the expressions (1.14) for the

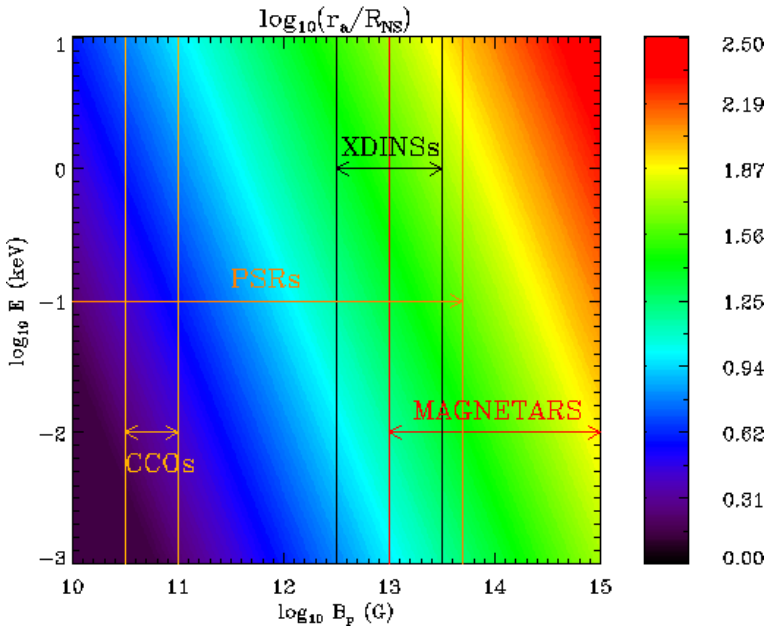

Figure 2.3: Contour plot showing the adiabatic radius $r_{\rm a}$ (in units of the stellar radius $R_{\rm NS}$) as a function of the polar magnetic field strength and the photon energy. The typical $B_{\rm pol}$-ranges for different classes of neutron stars (magnetars, XDINSs, CCOs and PSRs) are also shown (Taverna et al., 2015).

twisted magnetic field components one obtains

$$r_{\rm a} \simeq \left[1.3 \times 10^{-4}\,(2+p)\right]^{-1/(3+2p)} \left(\frac{\hbar\omega}{1\,{\rm keV}}\right)^{1/(3+2p)} \left(\frac{B_{\rm pol}}{10^{11}\,{\rm G}}\right)^{2/(3+2p)} R_{\rm NS}\,, \qquad (2.22)$$

where $F(\theta, p) \approx 2$ has been assumed for $\cos\theta \approx 1$. Since, in realistic cases, twist angles $\Delta\phi \approx 1$ rad are expected (which correspond to $p \approx 0.88$), one can use the expression for $r_{\rm a}$ in the dipole field limit ($p = 1$) as a reasonably good approximation also for twisted fields:

$$r_{\rm a} = 4.8 \left(\frac{\hbar\omega}{1\,{\rm keV}}\right)^{1/5} \left(\frac{B_{\rm pol}}{10^{11}\,{\rm G}}\right)^{2/5} R_{\rm NS}\,. \qquad (2.23)$$

The adiabatic radius is strictly related to the strength of vacuum polarization effects on the photon modes: as shown by equation (2.23), it is larger for NSs with stronger magnetic fields, i.e. photons are locked in their initial polarization state within a wider region close to the star surface. In the same way, for a fixed value of $B_{\rm pol}$, $r_{\rm a}$ is smaller for less energetic photons, which then start to change their polarization state closer to the surface with respect to more energetic ones. The behavior of $r_{\rm a}$ (in units of $R_{\rm NS}$) as a function of $B_{\rm pol}$ and the photon energy is plotted in Figure 2.3, where the typical magnetic field ranges for different class of NSs are also shown.

2.2.2 Gravitational effects

Light propagation is strongly influenced by the extreme gravitational field of NSs and black holes (BHs). Besides the gravitational redshift and ray bending effects, which

have been well studied in the past and used as tests of general relativity, Stark & Connors (1977) and Connors & Stark (1977) first proposed that strong gravity could affect directly also photon polarization. Ishihsara et al. (1988) distinguish two different effects: one induced by the parallel transport of the polarization vector along a null geodesic, while the other as a direct consequence of the relativistic ray bending. In particular, they refer to the latter as the "gravitational Faraday rotation", in analogy to that discovered by Faraday for linearly polarized radiation propagating through matter permeated by a longitudinal magnetic field.

Since the INSs studied in this work (magnetars and XDINSs) are slow rotators, the space-time outside these sources can be well described by the Schwarzschild metric, that in a spherical coordinate system (t, r, θ, ϕ) is given by

$$ds^2 = -\left(1 - \frac{2M}{r}\right) \mathrm{d}t^2 + \left(1 - \frac{2M}{r}\right)^{-1} \mathrm{d}r^2 + r^2 \mathrm{d}\theta^2 + r^2 \sin^2\theta \mathrm{d}\phi^2 \,, \tag{2.24}$$

with M the mass of the source and $G = c = 1$. The four-vector k^i tangent to a null geodesic is

$$\begin{aligned} k^t &= \left(1 - \frac{2M}{r}\right)^{-1} E & k^r &= \pm E \left[1 - \left(1 - \frac{2M}{r}\right) \frac{2L^2}{r^2 E}\right]^{1/2} \\ k^\theta &= \pm \frac{L^2}{r^2 \sin\theta} \left(\sin^2\theta - \cos^2\theta\right)^{1/2} & k^\phi &= \frac{L}{r^2 \sin^2\theta} \,, \end{aligned} \tag{2.25}$$

where E and L are constants of motion. The polarization vector $f^i = (f^t, f^r, f^\theta, f^\phi)$, instead, is determined by the orthogonal condition $k^i f_i = 0$ and, since it is a multiple of the null vector k^i, one can always take $f^t = 0$, without loss of generality. In this way, f^r can be simply expressed as a function of f^θ and f^ϕ.

For all the Petrov type D metrics, the parallel transport of the polarization vector can be derived exploiting the constant of motion discovered by Walker & Penrose (1970); in the Schwarzschild metric it is

$$\kappa_{\mathrm{WP}} = \kappa_2 + \mathrm{i}\kappa_1 = r k^t f^r + \mathrm{i} r^3 \sin\theta (k^\phi f^\theta - k^\theta f^\phi) \,. \tag{2.26}$$

So, by equating the real and imaginary parts calculated at the source (s) and at the observer (o) respectively, one obtains the rotation matrix R that gives the change in the polarization vector due to the parallel transport along a null geodesic

$$\begin{pmatrix} \hat{f}^\theta \\ \hat{f}^\phi \end{pmatrix}_{\mathrm{o}} = R \begin{pmatrix} \hat{f}^\theta \\ \hat{f}^\phi \end{pmatrix}_{\mathrm{s}} \,, \tag{2.27}$$

with $\hat{f}^\theta = r f^\theta$ and $\hat{f}^\phi = r \sin\theta f^\phi$. In particular, the R-matrix elements depend on the radial distance r through the components of k^i given by equations (2.25).

The spatial, three dimensional polarization vector in each point of the photon trajectory lies in a plane perpendicular to the propagation direction k^i. So, it can be decomposed in two components $f_\perp$ and $f_\parallel$ along the directions n^i and h^i orthogonal and parallel to the orbital plane, respectively:

$$\begin{pmatrix} f_\parallel \\ f_\perp \end{pmatrix} = N \begin{pmatrix} \hat{f}^\theta \\ \hat{f}^\phi \end{pmatrix} \,, \tag{2.28}$$

where N is a matrix of the form

$$N = \begin{pmatrix} h^\theta & h^\phi \\ n^\theta & n^\phi \end{pmatrix} . \tag{2.29}$$

Since the ray is deflected by the source gravity, the direction h^i varies along the photon trajectory, rotating the polarization plane and giving rise to the gravitational Faraday rotation. In order to derive the total effect a photon undergoes moving from the source to the observer, it is sufficient to combine the two transformations (2.27) and (2.28)

$$\begin{pmatrix} f_\parallel \\ f_\perp \end{pmatrix}_{\rm o} = N_{\rm o} R \begin{pmatrix} \hat{f}^\theta \\ \hat{f}^\phi \end{pmatrix}_{\rm s} = N_{\rm o} R N_{\rm s}^{-1} \begin{pmatrix} f_\parallel \\ f_\perp \end{pmatrix}_{\rm s} , \tag{2.30}$$

where in the last term it has been used the inverse of transformation (2.28) to express $\hat{f}^\theta$ and $\hat{f}^\phi$ at the source in terms of the components along n^i and h^i. The rotation matrix $N_{\rm o} R N_{\rm s}^{-1}$ can be written as

$$N_{\rm o} R N_{\rm s}^{-1} = \begin{pmatrix} \cos\upsilon & -\sin\upsilon \\ \sin\upsilon & \cos\upsilon \end{pmatrix} , \tag{2.31}$$

where the angle υ takes into account both the effects of the parallel transport along the null geodesic and of the gravitational Faraday rotation. Its behavior is shown as a function of the radial distance (in units of the Schwarzschild radius $R_{\rm s}$) in Figure 2.4: the change of the polarization plane induced by gravity is important only close to the star, up to rougly $20\,R_{\rm s}$ ($\sim 6\,R_{\rm NS}$). A simple order-of-magnitude calculation allows to estimate the length scale along which this change occurs

$$\ell_{\rm GR} = \left| \frac{1}{\sin\upsilon} \frac{{\rm d}\sin\upsilon}{{\rm d}r} \right|^{-1} \approx 10^6\,{\rm cm} . \tag{2.32}$$

By comparing $\ell_{\rm GR}$ with the length scale $\ell_{\rm A}$ along which the polarization vector changes due to the magnetized vacuum (see equation 2.20), it is appearent that the change of the polarization vector induced by QED effects in the presence of ultra-strong magnetic fields is much more rapid than that due to the strong gravity, and so GR effects are completely irrelevant. For this reason they will be neglected hereafter.

2.3 Stokes parameters

A convenient way to describe the polarization properties of the radiation collected from an astrophysical source is using the Stokes parameters, that are suitable combinations of the electric field complex amplitude components.

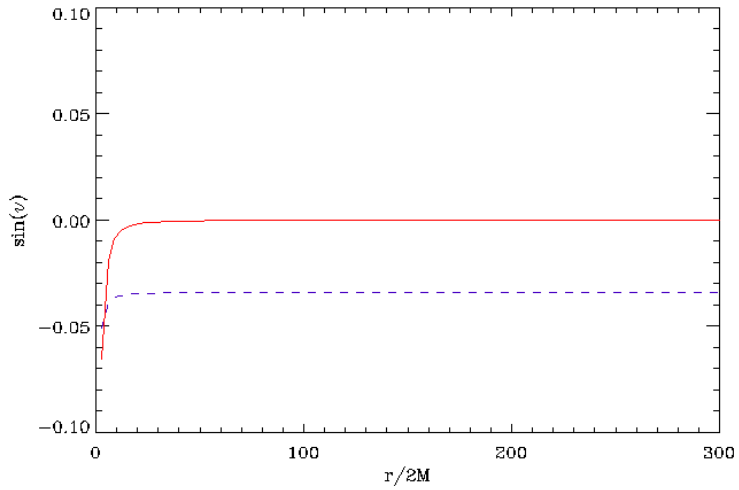

Figure 2.4: Sine of the angle υ by which the polarization vector of photons is rotated due to the strong gravitational field of a NS, plotted as a function of the radial distance $r/R_{\rm s}$. The red-solid line represents the change due to both the effects of parallel transport along a null geodesic and gravitational Faraday rotation; the blue-dashed line accounts only the former effect. Here the position angles of the source and of the observer are $\theta_{\rm s,o} = 45°$ and $\phi_{\rm s,o} = 0°$. The red curve has been shifted down to make easier the visual comparison.

2.3.1 Stokes parameters for single photons

In the cartesian frame (x, y, z) defined above, one can associate to each photon emitted from the star surface the following set of Stokes parameters

$$\begin{aligned}
\mathcal{I} &= A_x A_x^* + A_y A_y^* = a_x^2 + a_y^2 \\
\mathcal{Q} &= A_x A_x^* - A_y A_y^* = a_x^2 - a_y^2 \\
\mathcal{U} &= A_x A_y^* + A_y A_x^* = 2 a_x a_y \cos(\varphi_x - \varphi_y) \\
\mathcal{V} &= \mathrm{i}(A_x A_y^* - A_y A_x^*) = 2 a_x a_y \sin(\varphi_x - \varphi_y)\,,
\end{aligned} \tag{2.33}$$

where a star denotes the complex conjugate and the quantities a_x, a_y, φ_x and φ_y are related to A_x and A_y by

$$A_x = a_x \mathrm{e}^{-\mathrm{i}\varphi_x}\,, \qquad A_y = a_y \mathrm{e}^{-\mathrm{i}\varphi_y}\,. \tag{2.34}$$

The Stokes parameter $\mathcal{I}$ is related to the photon total intensity; $\mathcal{Q}$ and $\mathcal{U}$ describe the linear polarization, in particular the strength and the orientation in the $x-y$ plane of the polarization vector, respectively; finally $\mathcal{V}$ is the "circulararity" parameter, which measures the ratio between the polarization vector components along the x and y axes.

As it can be seen by equations (2.33), the set of Stokes parameters defined for each photon satisfy the condition

$$\mathcal{I}^2 = \mathcal{Q}^2 + \mathcal{U}^2 + \mathcal{V}^2\,. \tag{2.35}$$

Defining the total polarization fraction

$$\Pi = \frac{\sqrt{Q^2 + U^2 + V^2}}{I}\,, \tag{2.36}$$

radiation that satisfies equation (2.35) is said to be 100% polarized (see e.g. Rybicki & Lightman, 2004): in this case the polarization vector displays in general an ellipse in the plane perpendicular to the propagation direction, that becomes degenerate for linear polarization. For the sake of simplicity, one can always normalize $\mathcal{Q}$, $\mathcal{U}$ and $\mathcal{V}$ to the total intensity $\mathcal{I}$; in particular, since in the chosen reference frame $a_y = 0$ for O-mode photons and $a_x = 0$ for X-mode ones (see equations 2.17), one can associate to ordinary and extraordinary photons the following "Stokes vectors"

$$\begin{pmatrix} \bar{\mathcal{Q}} \\ \bar{\mathcal{U}} \\ \bar{\mathcal{V}} \end{pmatrix}_{\mathrm{O}} = \begin{pmatrix} 1 \\ 0 \\ 0 \end{pmatrix} \qquad \begin{pmatrix} \bar{\mathcal{Q}} \\ \bar{\mathcal{U}} \\ \bar{\mathcal{V}} \end{pmatrix}_{\mathrm{X}} = \begin{pmatrix} -1 \\ 0 \\ 0 \end{pmatrix}\,, \tag{2.37}$$

where a bar denotes the normalized Stokes parameters.

By using the Stokes parameters, equations (2.18) which describes the evolution of the normal modes due to vacuum polarization can be simplified in a set of three linearly independent differential equations

$$\begin{aligned} \frac{\mathrm{d}\bar{\mathcal{Q}}}{\mathrm{d}z'} &= -2P\bar{\mathcal{V}} \\ \frac{\mathrm{d}\bar{\mathcal{U}}}{\mathrm{d}z'} &= -(N-M)\bar{\mathcal{V}} \\ \frac{\mathrm{d}\bar{\mathcal{V}}}{\mathrm{d}z'} &= 2P\bar{\mathcal{Q}} + (N-M)\bar{\mathcal{U}}\,, \end{aligned} \tag{2.38}$$

where $\mathrm{d}z' = k_0\delta\mathrm{d}z/2$ and M, N, P are given by equations (2.19). The evolution of the Stokes parameters described by these equations follows the same pattern predicted by equations (2.18) for the complex amplitude components, since the Stokes parameters also change over the same length scale ℓ_{A}. Moreover, in order to perform numerical integrations, this last formulation has resulted to be more stable (see Taverna et al., 2014).

2.3.2 Stokes parameters for the entire radiation

Current instruments allow to measure the polarization properties of the radiation emitted from an astrophysical source by collecting a large number of photons during sufficiently long exposure times. The convenience of using the Stokes parameters lies precisely in the fact that they are additive (see e.g. Rybicki & Lightman, 2004): in this way one can describe the polarization features of the entire radiation through a set of "collective" Stokes parameters, that will be obtained by summing the Stokes parameters of single photons (see 2.33). Nevertheless, they are defined in a precise reference frame (x, y, z), that in turns depends on the direction of the local magnetic

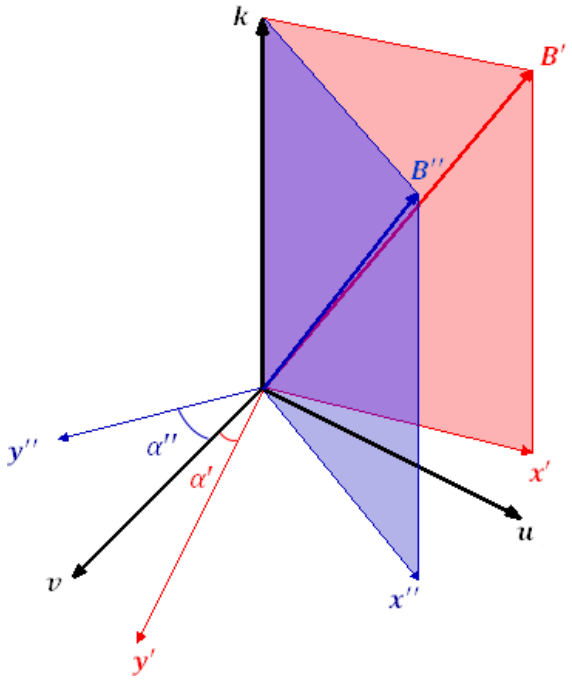

Figure 2.5: Graphical visualization of the different reference frames introduced in the text. $\boldsymbol{k}$ is the common propagation direction of the observed photons (LOS); ($\boldsymbol{u}$, $\boldsymbol{v}$) are the fixed, mutually orthogonal axes of the polarimeter; ($\boldsymbol{x'}, \boldsymbol{y'}$) and ($\boldsymbol{x''}, \boldsymbol{y''}$) are mutually orthogonal axes of two reference frames relative to photons coming from points characterized by different directions $\boldsymbol{B'}$ and $\boldsymbol{B''}$ of the local magnetic field. The angles α', α'' are also indicated (Taverna et al., 2015).

field. Since the observed photons will come from different regions, where the magnetic field takes in general different directions, their Stokes parameters will be defined in different reference frames (x_i, y_i, z_i), with the z_i axes along the respective propagation directions (at infinity coincide with the observer LOS) and the x_i axes in the planes defined each time by z_i and the local magnetic field direction (see e.g. Figure 2.5). So, it is necessary to refer the single Stokes parameters to the same, fixed reference frame before to sum them together; this fixed frame, said (u, v, w), can be always chosen as the polarimeter one, with the w-axis in the direction of the LOS and u, v axes as any pair of orthogonal directions in the detector plane.

Since the various $x_i - y_i$ planes and the $u - v$ plane are all perpendicular to the LOS, the required transformations are simple rotations around the vertical axis by different angles α_i, under which the Stokes parameters transform as

$$\begin{aligned} I_i &= \bar{\mathcal{I}}_i \\ Q_i &= \bar{\mathcal{Q}}_i \cos(2\alpha_i) + \bar{\mathcal{U}}_i \sin(2\alpha_i) \\ U_i &= \bar{\mathcal{U}}_i \cos(2\alpha_i) - \bar{\mathcal{Q}}_i \sin(2\alpha_i) \\ V_i &= \bar{\mathcal{V}}_i \,. \end{aligned} \tag{2.39}$$

Considering that, in the hypotheses of this work, all the photons emitted from the star surface are linearly polarized either in the O- or in the X-mode (see §2.1.2), one can assume that the Stokes parameters $(\bar{\mathcal{I}}_i, \bar{\mathcal{Q}}_i, \bar{\mathcal{U}}_i, \bar{\mathcal{V}}_i)$ at the emission point are given by equations (2.37). Moreover, since inside the adiabatic region the photon electric field is forced to change continuously to adapt its direction to that of the local magnetic field, the α_i angles can be calculated at the boundary of the adiabatic region, that is approximately given by the adiabatic radius $r_{\rm a}$ (see §2.2.1). Thus, once referred to the same reference frame, the collective Stokes parameters (I, Q, U, V) are obtained by the sum of the rotated Stokes parameters of the single photons.

In order to show in a simple way the effects that the reference frame rotation causes on the observed polarization signal, one can resort to an approximate treatment of the polarization mode evolution, in which only the adiabatic and the external regions are considered, and they are divided by a sharp edge located at $r_{\rm a}$ (see Taverna et al., 2015). With respect to the full numerical integration of the differential equation system (2.38), this method allows to substantially gain computational time and to easily assess the dependences of the polarization observables on the various physical and geometrical parameters (see chapter 3). The limits of validity of this approximation will be discussed in chapter 4.

Under these conditions, the rotated Stokes parameters are left unchanged as the photon travels from the adiabatic boundary to the observer, and their sum results in

$$\begin{aligned} I &= \sum_{i=1}^{N} I_i = N \\ Q &= \sum_{i=1}^{N} Q_i = \sum_{i=1}^{N_{\rm O}} \cos(2\alpha_i) - \sum_{j=1}^{N_{\rm X}} \cos(2\alpha_j) \\ U &= \sum_{i=1}^{N} U_i = \sum_{j=1}^{N_{\rm X}} \sin(2\alpha_j) - \sum_{i=1}^{N_{\rm O}} \sin(2\alpha_i) \\ V &= \sum_{i=1}^{N} V_i = 0\,, \end{aligned} \tag{2.40}$$

where $N_{\rm O}$ ($N_{\rm X}$) is the number of O-mode (X-mode) photons, $N = N_{\rm X} + N_{\rm O}$ and equations (2.37) have been used. From these relations it can be easily seen that, in the general case of radiation composed by the superposition of many photons, the identity (2.35) has to be corrected in

$$I^2 \geq Q^2 + U^2 + V^2\,. \tag{2.41}$$

This is due essentially to the fact that, since the stellar magnetic field is non-uniform, the rotation angles α_i are in general different photon per photon. The equality holds again only if all the α_i angles were equal to a same value α_0: in this case, in fact, the single terms in equations (2.40) add coherently, so that the entire radiation remains 100% polarized, because so the single photons are.

2.3.3 Polarization observables

Stokes parameters can be used to construct suitable observables that can be measured by the state-of-art polarimeters, allowing to understand how the polarization properties of collected radiation depend on the typical physical and geometrical parameters. These are the linear polarization fraction $\Pi_{\rm L}$, the polarization angle $\chi_{\rm p}$ and the circular polarization fraction $\Pi_{\rm C}$, defined as

$$\Pi_{\rm L} = \frac{\sqrt{Q^2+U^2}}{I} \tag{2.42}$$

$$\chi_{\rm p} = \frac{1}{2}\arctan\left(\frac{U}{Q}\right) \tag{2.43}$$

$$\Pi_{\rm C} = \frac{V}{I}\,. \tag{2.44}$$

Since, according to the simplified approach introduced in the previous section, V is always 0 for photons linearly polarized in either the O- or the X-mode, the circular polarization fraction can be neglected at the moment. $\Pi_{\rm L}$ represents the fraction of the total number of photons that are linearly polarized in the same mode. At the emission region it is in general given by

$$\Pi_{\rm L}^{\rm e} = \frac{|N_{\rm X} - N_{\rm O}|}{N}\,, \tag{2.45}$$

so that it is maximum (100%) if all the photons are polarized in the O-mode or in the X-mode, while it will be 0 for an equal number of O- and X-mode photons. The polarization angle, instead, represents the inclination of the polarization vector, ranging from 0° to 180° in the $u-v$ plane orthogonal to the LOS. In this respect, since both Q and U can assume either positive or negative values, care must be taken in defining the correct co-domain of the arctan function in equation (2.43): in particular, for $Q>0$ it will take values in the first ($U>0$) and in the fourth ($U<0$) quadrants, while for $Q<0$ in the second ($U>0$) and in the third ($U<0$) quadrants. Thus, at the emission region, it will be $\chi_{\rm p}=0°$ for ordinary photons and $\chi_{\rm p}=90°$ for extraordinary ones.

The linear polarization fraction of the whole radiation as observed at infinity is not, in general, equivalent to that at the emission. Using the expressions (2.40) one has

$$\begin{aligned}\Pi_{\rm L} &= \frac{1}{N}\left[N + 2\sum_{i=1}^{N_{\rm O}}\sum_{k>i}^{N_{\rm O}}\cos\left(2\alpha_i - 2\alpha_k\right) + 2\sum_{j=1}^{N_{\rm X}}\sum_{r>j}^{N_{\rm X}}\cos\left(2\alpha_j - 2\alpha_r\right)\right.\\ &\qquad \left. -2\sum_{i=1}^{N_{\rm O}}\sum_{j=1}^{N_{\rm X}}\cos\left(2\alpha_i - 2\alpha_j\right)\right]^{1/2}\,,\end{aligned} \tag{2.46}$$

which, for different values of the α_i angles, is striclty smaller than $\Pi_{\rm L}^{\rm e}$, the equality holding only for all the α_i equal to the common value α_0 (implying that the stellar magnetic field is uniform). In fact, in this latter case, it results:

$$\begin{aligned}\Pi_{\rm L} &= \frac{1}{N}\left[N + N_{\rm O}(N_{\rm O}-1) + N_{\rm X}(N_{\rm X}-1) - 2N_{\rm O}N_{\rm X}\right]^{1/2}\\ &= \frac{|N_{\rm O} - N_{\rm X}|}{N}\,.\end{aligned} \tag{2.47}$$

Similarly, for the polarization angle of the entire radiation one in general obtains

$$\chi_{\rm p} = \frac{1}{2}\arctan\left[-\frac{\sum_{i=1}^{N_{\rm O}}\sin\left(2\alpha_i\right)-\sum_{j=1}^{N_{\rm X}}\sin\left(2\alpha_j\right)}{\sum_{i=1}^{N_{\rm O}}\cos\left(2\alpha_i\right)-\sum_{j=1}^{N_{\rm X}}\cos\left(2\alpha_j\right)}\right] . \tag{2.48}$$

However, reducing to the case $\alpha_i = \alpha_0$ for each photon, the previous expression simplifies in

$$\begin{aligned}\chi_{\rm p} &= \frac{1}{2}\arctan\left[-\frac{(N_{\rm O}-N_{\rm X})\sin\left(2\alpha_0\right)}{(N_{\rm O}-N_{\rm X})\cos\left(2\alpha_0\right)}\right] \\ &= -\alpha_0\,, \end{aligned} \tag{2.49}$$

which does not contain any information on the polarization state of the emitted photons. The last two equations show, instead, that the polarization angle depends on the geometry of stellar magnetic field, through the α-angle distribution that depends in turn on the magnetic field direction at the photon emission point (see next chapter).

Chapter 3

Observed NS polarization pattern

In this chapter I present some numerical simulations aiming at reproducing the typical polarization pattern of neutron star surface emission as observed at infinity. Due to the non-uniform NS magnetic field (which involves the rotation of the Stokes parameters discussed in §2.3.2) and to vacuum polarization (see §2.2.1), the measured polarization observables are in general different from those at the emission. Hence, in order to correctly interpret the observations and to reconstruct the intrinsic polarization pattern, a study of these effects is crucial. To this end, I derive the distribution of the angles α by which the Stokes parameters have to be rotated to coincide with the fixed polarimeter frame (see §2.3.2). Then, I present the simulated behaviors of the polarization observables for different values of the physical and geometrical parameters that characterize the NS, i.e. the star magnetic field intensity at the poles, the inclination of LOS and magnetic axis with respect to the star spin axis and the magnetic twist angle. In order to better elucidate the geometrical and QED effects on the polarization pattern, I neglect in this chapter the effects of RCS, that will be discussed in details in the following.

3.1 The α-angle distribution

Since all the photons collected by the instrument are those propagating along the observer LOS, it is convenient to introduce a stellar fixed frame (X, Y, Z) with the Z-axis in the direction of the LOS (characterized by the unit vector $\boldsymbol{\ell}$), the X-axis in the plane of $\boldsymbol{\ell}$ and the star spin axis (unit vector $\boldsymbol{\Omega}$) and the Y-axis orthogonal to both X and Z. Let χ be the angle between the LOS and the spin axis, while ξ is the angle between the magnetic axis $\boldsymbol{b}_{\rm dip}$ and the LOS. Referring to Figure 3.1a, the expressions for the spin axis components are

$$\boldsymbol{\Omega} = \begin{pmatrix} -\sin\chi \\ 0 \\ \cos\chi \end{pmatrix} , \tag{3.1}$$

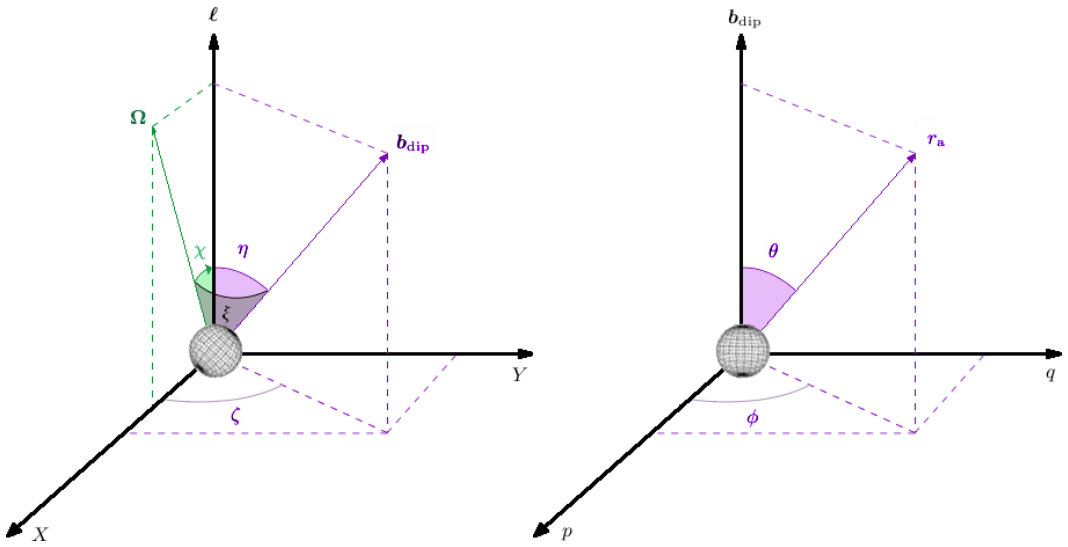

Figure 3.1: The two reference frames introduced in the text. Left: the (X, Y, Z) frame with the Z-axis along the LOS direction $\boldsymbol{\ell}$, the X-axis in the plane made by $\boldsymbol{\ell}$ and the spin axis $\boldsymbol{\Omega}$ and the Y-axis obtained as $\boldsymbol{\ell} \times \boldsymbol{X}$. Right: the (p, q, t) reference frame with the t-axis along the star magnetic axis $\boldsymbol{b}_{\rm dip}$ and p, q axes chosen along two mutually orthogonal directions in the plane perpendicular to $\boldsymbol{b}_{\rm dip}$. The angles χ, ξ, η, ζ, θ and ϕ are also shown.

while, by introducing the polar angles η and ζ that fix the direction of $\boldsymbol{b}_{\rm dip}$, it results $\boldsymbol{b}_{\rm dip} = (\sin\eta\cos\zeta, \sin\eta\sin\zeta, \cos\eta)$. The angles η and ζ are related to χ and ξ by

$$\begin{aligned} \cos\eta &= \cos\chi\cos\xi + \sin\chi\sin\xi\cos\gamma \\ \cos\zeta &= \frac{\cos\xi - \cos\chi\cos\eta}{\sin\chi\sin\eta}\,, \end{aligned} \tag{3.2}$$

where γ is the star rotational phase; hence, using these last expressions, the components of $\boldsymbol{b}_{\rm dip}$ take the form

$$\boldsymbol{b}_{\rm dip} = \begin{pmatrix} \sin\chi\cos\xi - \cos\chi\sin\xi\cos\gamma \\ \sin\xi\sin\gamma \\ \cos\chi\cos\xi + \sin\chi\sin\xi\cos\gamma \end{pmatrix}\,. \tag{3.3}$$

According to the discussion in section 2.3.2, the w-axis of the polarimeter frame (u, v, w) will be coincident with the Z-axis, while the axes u and v can be chosen as any pair of orthogonal directions in the XY plane, i.e.

$$\boldsymbol{u} = \begin{pmatrix} \cos\psi \\ \sin\psi \\ 0 \end{pmatrix}\,, \quad \boldsymbol{v} = \begin{pmatrix} -\sin\psi \\ \cos\psi \\ 0 \end{pmatrix}\,, \tag{3.4}$$

where ψ is the angle between u and X. The axes of the reference frame (x, y, z) in which the single photon Stokes parameters are naturally defined (see section 2.3.1) depend, instead, on the magnetic field geometry

$$\boldsymbol{z} \equiv \boldsymbol{\ell}\,, \qquad \boldsymbol{y} = \frac{\boldsymbol{\ell} \times \boldsymbol{B}}{|\boldsymbol{\ell} \times \boldsymbol{B}|}\,, \qquad \boldsymbol{x} = \boldsymbol{\ell} \times \boldsymbol{y}\,, \tag{3.5}$$

where $\boldsymbol{B}$ is the stellar magnetic field at the emission point. The angle α by which the photon frame (x, y, z) has to be rotated to coincide with the polarimeter frame (u, v, w) is then simply obtained taking the scalar product of $\boldsymbol{u}$ with $\boldsymbol{x}$

$$\cos\alpha = \boldsymbol{u} \cdot \boldsymbol{x}\,. \tag{3.6}$$

The indetermination in the sign of α is resolved looking at the sign of $\boldsymbol{v} \cdot \boldsymbol{x}$; if the latter is positive the rotation is by an angle $-\alpha$ (i.e. $\sin\alpha = -\sqrt{1 - \cos^2\alpha}$).

Since, as discussed in section §2.3.2, we need to consider photons only from the boundary of the adiabatic region outwards, the expression of $\boldsymbol{B}$ that appears in the second of equations (3.5) is that of the stellar magnetic field calculated at $r_{\rm a}$ (see equation 2.23). Actually, it is more convenient to express the magnetic field components in a reference frame (p, q, t), see Figure 3.1b, with the t-axis along $\boldsymbol{b}_{\rm dip}$ and p, q two mutually orthogonal directions in the plane perpendicular to t. In order to outline the procedure that leads to the α-distribution, I will present the calculations only in the case of a purely dipolar field. Albeit the derivation in the general case of a twisted field is basically the same, the radial and angular dependences of the B-field are more complicated (see equation 1.14), and the corresponding expressions for α become very involved. Hence, for the sake of conciseness I will not show the full expressions in the following, redirecting to section 3.3 for some results obtained with a non-zero twist angle.

The polar components of the stellar dipole field at $r = r_{\rm a}$ in the (p, q, t) frame are

$$\boldsymbol{B}^{\rm polar} = \begin{pmatrix} B_r \\ B_\theta \\ B_\phi \end{pmatrix} = \frac{B_{\rm pol}}{2} \left(\frac{R_{\rm NS}}{r_{\rm a}}\right)^3 \begin{pmatrix} 2\cos\theta \\ \sin\theta \\ 0 \end{pmatrix}\,, \tag{3.7}$$

with θ the magnetic colatitude (see Figure 3.1b). However, in order to calculate the expression of α given by equation (3.6), the Cartesian components of $\boldsymbol{B}$ in the (X, Y, Z) frame are needed; they can be obtained through a change of basis as

$$\begin{aligned} B_X &= B_p p_X + B_q q_X + B_t t_X \\ B_Y &= B_p p_Y + B_q q_Y + B_t t_Y \\ B_Z &= B_p p_Z + B_q q_Z + B_t t_Z\,. \end{aligned} \tag{3.8}$$

The Cartesian components (B_p, B_q, B_t) of the magnetic field in the reference frame (p, q, t) can be obtained from its polar components (B_r, B_θ, B_ϕ) given in equation (3.7) using the following expressions:

$$\boldsymbol{B} = \begin{pmatrix} B_p \\ B_q \\ B_t \end{pmatrix} = \begin{pmatrix} \boldsymbol{B}^{\rm polar} \cdot \boldsymbol{p}^{\rm polar} \\ \boldsymbol{B}^{\rm polar} \cdot \boldsymbol{q}^{\rm polar} \\ \boldsymbol{B}^{\rm polar} \cdot \boldsymbol{t}^{\rm polar} \end{pmatrix} = \begin{pmatrix} \sin\theta\cos\phi B_r + \cos\theta\cos\phi B_\theta - \sin\phi B_\phi \\ \sin\theta\sin\phi B_r + \cos\theta\sin\phi B_\theta + \cos\phi B_\phi \\ \cos\theta B_r - \sin\theta B_\theta \end{pmatrix}\,, \tag{3.9}$$

where $\boldsymbol{p}^{\rm polar}$, $\boldsymbol{q}^{\rm polar}$ and $\boldsymbol{t}^{\rm polar}$ are the unit vectors relative to the (p,q,t) frame expressed in polar components and ϕ is the magnetic azimuth (see Figure 3.1b).

The Cartesian components of the unit vectors $\boldsymbol{p}$, $\boldsymbol{q}$ and $\boldsymbol{t}$ in the (X,Y,Z) reference frame can be obtained instead as follows. Since it is $\boldsymbol{t} \equiv \boldsymbol{b}_{\rm dip}$, the components of $\boldsymbol{t}$ are simply given by equation (3.3). Then, considering $\boldsymbol{m}$ as a generic unit vector orthogonal to the star spin axis $\boldsymbol{\Omega}$ and rotating with the star, $\boldsymbol{p}$ is fixed by the projection of $\boldsymbol{m}$ perpendicular to $\boldsymbol{b}_{\rm dip}$

$$\boldsymbol{p} \equiv \frac{\boldsymbol{m} - (\boldsymbol{m}\cdot\boldsymbol{b}_{\rm dip})\,\boldsymbol{b}_{\rm dip}}{|\boldsymbol{m} - (\boldsymbol{m}\cdot\boldsymbol{b}_{\rm dip})\,\boldsymbol{b}_{\rm dip}|}\,. \tag{3.10}$$

Without loss of generality, one can choose $\boldsymbol{m}$ as the projection of $\boldsymbol{b}_{\rm dip}$ perpendicular to $\boldsymbol{\Omega}$

$$\boldsymbol{m} \equiv \frac{\boldsymbol{b}_{\rm dip} - (\boldsymbol{b}_{\rm dip}\cdot\boldsymbol{\Omega})\boldsymbol{\Omega}}{|\boldsymbol{b}_{\rm dip} - (\boldsymbol{b}_{\rm dip}\cdot\boldsymbol{\Omega})\boldsymbol{\Omega}|} = \begin{pmatrix} -\cos\chi\cos\gamma \\ \sin\gamma \\ \sin\chi\cos\gamma \end{pmatrix}\,, \tag{3.11}$$

where equations (3.1) and (3.3) have been used; hence, the Cartesian components of $\boldsymbol{p} = (p_X, p_Y, p_Z)$ are given by

$$\boldsymbol{p} = \begin{pmatrix} -\sin\chi\sin\xi - \cos\chi\cos\xi\cos\gamma \\ \cos\xi\sin\gamma \\ \sin\chi\cos\xi\cos\gamma - \cos\chi\sin\xi \end{pmatrix}\,. \tag{3.12}$$

Finally, the unit vector q is given by the vector product between $\boldsymbol{b}_{\rm dip}$ and $\boldsymbol{p}$

$$\boldsymbol{q} = \boldsymbol{b}_{\rm dip}\times\boldsymbol{p} = \begin{pmatrix} -\cos\chi\sin\gamma \\ -\cos\gamma \\ \sin\chi\sin\gamma \end{pmatrix}\,. \tag{3.13}$$

Substituting the expressions (3.8) in equations (3.5), the components of the unit vector $\boldsymbol{x}$ in the LOS reference frame are

$$\boldsymbol{x} = -\frac{1}{\sqrt{B_X^2 + B_Y^2}}\begin{pmatrix} B_X \\ B_Y \\ 0 \end{pmatrix}\,. \tag{3.14}$$

B_X and B_Y clearly depend on the angles χ, ξ and the phase γ through the unit vectors of the (p,q,t) reference frame, given by equations (3.3), (3.12) and (3.13). Moreover, they depend also on the magnetic colatitude and azimuth (θ and ϕ, that fix the point where the magnetic field is calculated on the adiabatic boundary) through the components B_p, B_q and B_t given by equations (3.7) and (3.9). Actually, the angles θ and ϕ depend in turn on χ, ξ and γ. In order to make this dependence explicit, Figure 3.2 shows the path of a photon emitted from a point of the surface, characterized by the polar angles $\Theta_{\rm S}$ and $\Phi_{\rm S}$ in the LOS reference frame, up to the point where it crosses the adiabatic boundary, characterized by the angles Θ and Φ. Observing the star at infinity, only photons traveling along vectors $\boldsymbol{k} = (0,0,k)$ parallel to the LOS $\boldsymbol{\ell}$ will be collected. The modulus of each vector $\boldsymbol{k}$ is fixed by the condition

$$\boldsymbol{r}_0 + \boldsymbol{k} = \boldsymbol{r}_{\rm a}\,, \tag{3.15}$$

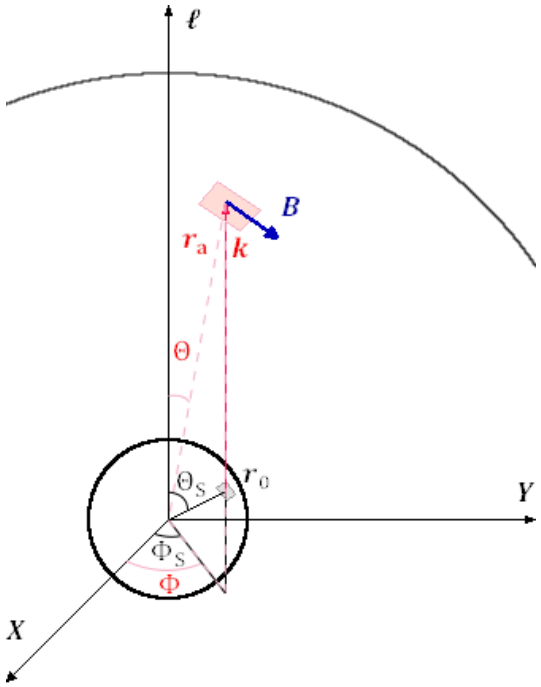

Figure 3.2: The path of a photon emitted by a point on the star surface with polar angles Θ_S and Φ_S, that crosses the adiabatic boundary ($r = r_a$) in a point of polar angles Θ and Φ in the LOS reference frame (Taverna et al., 2015).

where $\boldsymbol{r}_0 = R_{\rm NS}(\sin\Theta_{\rm S}\cos\Phi_{\rm S}, \sin\Theta_{\rm S}\sin\Phi_{\rm S}, \cos\Theta_{\rm S})$ is the position vector of the surface point from which the photon was emitted and $\boldsymbol{r}_{\rm a} = r_{\rm a}(\sin\Theta\cos\Phi, \sin\Theta\sin\Phi, \cos\Theta)$ is the position vector of the point where the photon crosses the adiabatic boundary. Taking the norm of both the sides of equation (3.15) and solving for k one has

$$k = \pm\sqrt{r_{\rm a}^2 - R_{\rm NS}^2\sin^2\Theta_{\rm S}} - R_{\rm NS}\cos\Theta_{\rm S}\,, \tag{3.16}$$

where the negative solution holds for a photon that propagates along the LOS but in the opposite direction with respect to the observer (so it should be rejected) and the distance $r_{\rm a}$ of the adiabatic boundary is given by equation (2.23). Substituting this result again in equation (3.15), one obtains

$$\boldsymbol{r}_{\rm a} = \begin{pmatrix} R_{\rm NS}\sin\Theta_{\rm S}\cos\Phi_{\rm S} \\ R_{\rm NS}\sin\Theta_{\rm S}\sin\Phi_{\rm S} \\ \sqrt{r_{\rm a}^2 - R_{\rm NS}^2\sin^2\Theta_{\rm S}} \end{pmatrix}\,. \tag{3.17}$$

From simple geometrical considerations (see again Figure 3.1b), it follows that

$$\cos\theta = \boldsymbol{b}_{\rm dip}\cdot\frac{\boldsymbol{r}_{\rm a}}{r_{\rm a}} \tag{3.18}$$

and, using equations (3.3) and (3.17), this gives

$$\begin{aligned}\cos\theta = {} & \frac{R_{\rm NS}}{r_{\rm a}}\sin\Theta_{\rm S}\left(\cos\Phi_{\rm S}\sin\chi\cos\xi + \sin\Phi_{\rm S}\sin\xi\sin\gamma - \cos\Phi_{\rm S}\cos\chi\sin\xi\cos\gamma\right) \\ & + \sqrt{1 - \left(\frac{R_{\rm NS}}{r_{\rm a}}\sin\Theta_{\rm S}\right)^2}\left(\cos\chi\cos\xi + \sin\chi\sin\xi\cos\gamma\right)\,.\end{aligned} \tag{3.19}$$

The cosine of the angle ϕ can be, instead, obtained as

$$\cos\phi = \boldsymbol{p}\cdot\boldsymbol{r}_{\rm a}^{\perp}\,, \tag{3.20}$$

where $\boldsymbol{p}$ is given by equation (3.12) and $\boldsymbol{r}_{\rm a}^{\perp}$ is the unit vector of the projection of $\boldsymbol{r}_{\rm a}$ orhogonal to $\boldsymbol{b}_{\rm dip}$

$$\boldsymbol{r}_{\rm a}^{\perp} = \frac{\boldsymbol{r}_{\rm a} - (\boldsymbol{r}_{\rm a}\cdot\boldsymbol{b}_{\rm dip})\,\boldsymbol{b}_{\rm dip}}{|\boldsymbol{r}_{\rm a} - (\boldsymbol{r}_{\rm a}\cdot\boldsymbol{b}_{\rm dip})\,\boldsymbol{b}_{\rm dip}|}\,. \tag{3.21}$$

Putting all together, one obtains

$$\begin{aligned}\cos\phi = {} & \frac{R_{\rm NS}\sin\Theta_{\rm S}}{r_{\rm a}\sin\theta}\left(\sin\Phi_{\rm S}\cos\xi\sin\gamma - \cos\Phi_{\rm S}\sin\chi\sin\xi - \cos\Phi_{\rm S}\cos\chi\cos\xi\cos\gamma\right) \\ & + \sqrt{\frac{r_{\rm a}^2 - R_{\rm NS}^2\sin^2\Theta_{\rm S}}{r_{\rm a}^2\sin^2\theta}}\left(\sin\chi\cos\xi\cos\gamma - \cos\chi\sin\xi\right)\,.\end{aligned} \tag{3.22}$$

Finally, substituting into equation (3.6) gives the distribution of α:

$$\cos\alpha = -\frac{B_X\cos\psi - B_Y\sin\psi}{\sqrt{B_X^2 + B_Y^2}}\,, \tag{3.23}$$

which is a function of the angles χ, ξ, the phase γ, the photon energy E and $B_{\rm pol}$ (through the adiabatic radius $r_{\rm a}$, see equation 2.23), the polar angles $\Theta_{\rm S}$ and $\Phi_{\rm S}$ that fix the points on the surface from which the photons were emitted and the angle ψ by which the polarimeter frame is rotated with respect to the LOS one. For the sake of simplicity, in the following I take $\psi = 0$, i.e. the u (v) axis of the polarimeter coincides with the X (Y) axis of the LOS frame, although the generalization to other values is straightforward.

3.2 Numerical implementation

In order to calculate the observed polarization fraction $\Pi_{\rm L}$ and polarization angle $\chi_{\rm p}$ I use the the ray-tracing code developed by Zane & Turolla (2006), to which specific modules for the evaluation of the α-angle distribution and of the Stokes parameters have been added. QED effects are included as described in section 2.3.2, i.e. considering only the adiabatic and the external regions divided by the adiabatic boundary as a sharp edge at $r = r_{\rm a}$. The code takes into account the effects due to the strong gravity on photon propagation (relativistic ray bending) and on the stellar magnetic field; the direct effects of general relativity on the polarization vectors have been, instead, neglected (see §2.2.2). The GR corrections on a dipole field are given by

$$\begin{aligned} B_r^{\rm GR} &= f_{\rm dip} B_r \\ B_\theta^{\rm GR} &= g_{\rm dip} B_\theta \\ B_\phi^{\rm GR} &= B_\phi = 0\,, \end{aligned} \tag{3.24}$$

where (see Page & Sarmiento, 1996)

$$\begin{aligned} f_{\rm dip} &= -\frac{3}{x^3}\left[\ln(1-x) + \frac{1}{2}x(x+2)\right] \\ g_{\rm dip} &= \sqrt{1-x}\left(-2f_{\rm dip} + \frac{3}{1-x}\right)\,, \end{aligned} \tag{3.25}$$

with $x = R_{\rm s}/r$ ($R_{\rm s}$ is the Schwarzschild radius), and B_r, B_θ and B_ϕ are given by equation (3.7).

The expressions for the collective Stokes parameters Q and U (equations 2.40) can be easily generalized to a continuous photon distribution by replacing the sums with integrals over the visible part of the star surface

$$\begin{aligned} F_Q &= \int_0^{2\pi} {\rm d}\Phi_{\rm S} \int_0^1 {\rm d}u^2\, (n_{\rm O} - n_{\rm X}) \cos(2\alpha) \\ F_U &= \int_0^{2\pi} {\rm d}\Phi_{\rm S} \int_0^1 {\rm d}u^2\, (n_{\rm X} - n_{\rm O}) \sin(2\alpha)\,, \end{aligned} \tag{3.26}$$

where $n_{\rm O}$ ($n_{\rm X}$) is the photon "number intensity" in the ordinary (extraordinary) mode and F_Q and F_U are the "fluxes" of Stokes parameters (see Pavlov & Zavlin, 2000;

Taverna et al., 2015). The total photon flux is obtained in a similar way

$$F_I = \int_0^{2\pi} \mathrm{d}\Phi_\mathrm{S} \int_0^1 \mathrm{d}u^2 \, (n_\mathrm{O} + n_\mathrm{X}) \ . \tag{3.27}$$

The integration variable $u = \sin\bar{\Theta}$ is related to Θ_S by the integral

$$\bar{\Theta} = \int_0^{1/2} \frac{\mathrm{d}v \sin\Theta_\mathrm{S}}{\left[(1-x)/4 - (1-2vx)v^2 \sin^2\Theta_\mathrm{S}\right]^{1/2}} \, , \tag{3.28}$$

that accounts for ray bending and reduces to $\bar{\Theta} = \Theta_\mathrm{S}$ in the limit $x \ll 1$ (when the effects of general relativity can be neglected).

In general, n_O and n_X depend on the photon energy and direction, and on the position on the star surface of the emission point. However, since the focus of this chapter is on the combined effects of QED and geometry on the polarization pattern, I consider here the simple case of radiation emitted by the cooling star surface with an isotropic blackbody distribution, referring to the next chapters for more realistic emission models. The photon number intensity is then

$$n_\mathrm{X,O} = \frac{2}{h^2c^2} \frac{E^2}{\mathrm{e}^{E/kT} - 1} \, , \tag{3.29}$$

where T is the local surface temperature. Instead of the standard temperature distribution for a core-centred dipole field, $T(\theta_\mathrm{B}) = T_\mathrm{pol} |\cos\theta_\mathrm{B}|^{1/2}$ (see e.g. Page, 1995), with θ_B the angle between the local normal and $\boldsymbol{B}$, and T_pol the temperature at the pole, I assume a variant of this to avoid a vanishing temperature at the equator

$$T(\theta_\mathrm{B}) = \max(T_\mathrm{pol} |\cos\theta_\mathrm{B}|^{1/2}, T_\mathrm{eq}) \, , \tag{3.30}$$

where T_eq is the equator temperature; in the following it is $T_\mathrm{pol} = 150$ eV and $T_\mathrm{eq} = 100$ eV.

The polarization degree of the radiation emitted at the surface is fixed specifying the ratio $p_0 \equiv n_\mathrm{X}/(n_\mathrm{X} + n_\mathrm{O})$, such that $\Pi_\mathrm{L}^\mathrm{e} = |n_\mathrm{X} - n_\mathrm{O}|/(n_\mathrm{X} + n_\mathrm{O}) = |2p_0 - 1|$ (see equation 2.45). Since, as mentioned above, for magnetic fields typical of XDINSs and magnetars the X-mode photon opacity is expected to be much smaller than that for O-mode photons (see equation 2.1), in the following photons emitted from the star surface are taken all polarized in the extraordinary mode, unless explicitly stated otherwise, corresponding to $p_0 = 1$ (see e.g. Fernàndez & Davis, 2011; Taverna et al., 2014, 2015). Moreover, this is indeed the choice that produces the most unfavourable conditions to detect the depolarizing effects of geometry on the polarization observables (see below).

3.3 Results

The polarization observables Π_L and χ_p can be computed recalling the definitions given in equations (2.42) and (2.43) and using the expressions (3.26) and (3.27) just derived for the Stokes parameters, together with the distribution of $\cos\alpha$ given in equation (3.23).

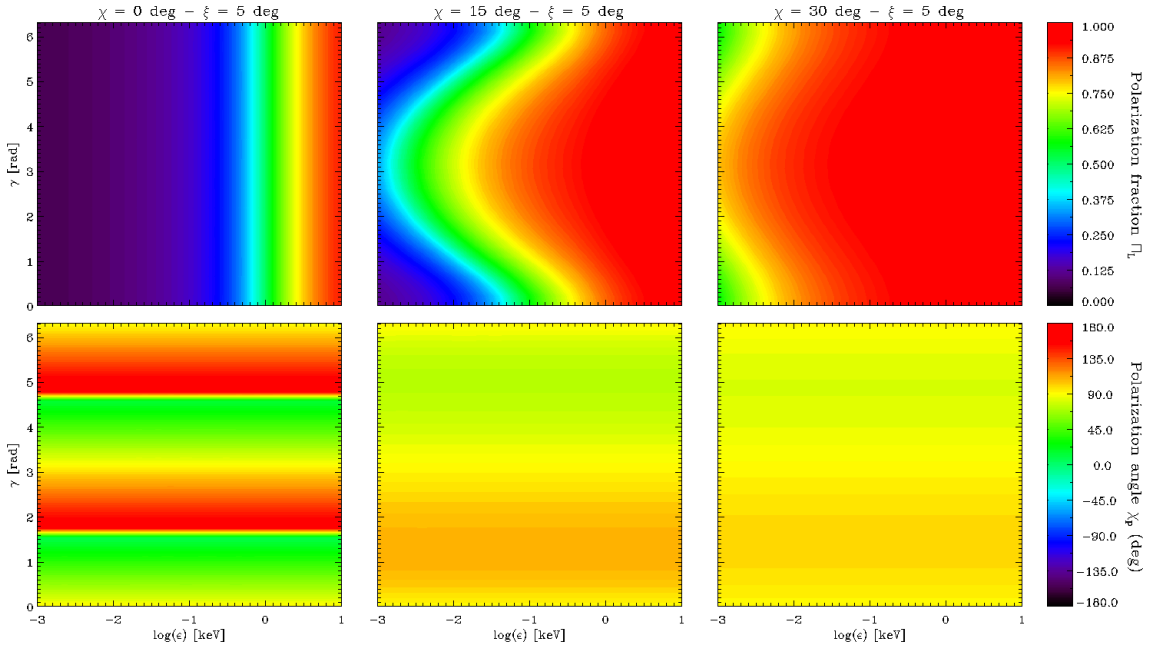

Figure 3.3: Contour plots in the energy-phase plane of the polarization fraction (top row) and the polarization angle (bottom row) for a neutron star with $B_{\rm pol} = 10^{13}$ G, $R_{\rm NS} = 10$ km and mass $M_{\rm NS} = 1.4\,M_{\odot}$. The inclination of the magnetic axis with respect to the spin axis is fixed to $\xi = 5°$, while the angle between the spin axis and the LOS is $\chi = 0°$ (left-hand column), 15° (middle column) and 30° (right-hand column). Seed photons are all polarized in the X-mode (Taverna et al., 2015).

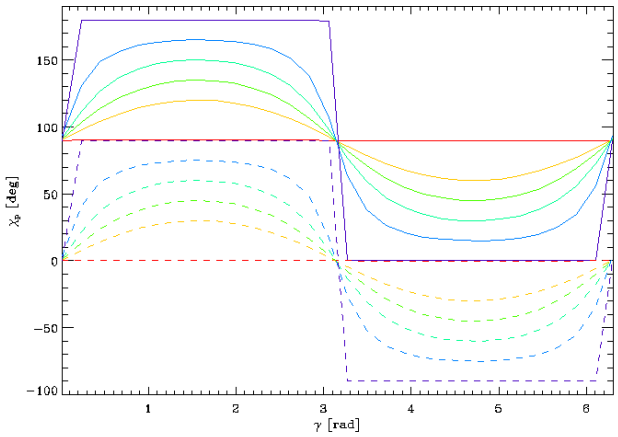

Figure 3.4: Polarization angle as a function of the rotational phase at a fixed energy ($E = 0.02$ keV), for $\chi = 90°$ and different values of ξ: 0° (red), 30° (orange), 45° (green), 60° (light blue) 75° (blue) and 90° (violet). The solid (dashed) lines correspond to seed photons all polarized in the X-mode (O-mode). The curves for $\xi = 90°$ are actually box-like; the sloping lines are an artefact introduced by the finite resolution of the phase grid. The values of $R_{\rm NS}$, $M_{\rm NS}$ and $B_{\rm pol}$ are the same as in Figure 3.3 (Taverna et al., 2015).

Figure 3.3 shows the polarization fraction and the polarization angle as functions of the photon energy and the rotational phase, for different values of the inclination χ of the LOS with respect to the star spin axis. The magnetic axis is at an angle $\xi = 5°$ with respect to the spin axis (i.e. the NS is a nearly aligned rotator) and $B_{\rm pol} = 10^{13}$ G. The effects produced by the rotation of the reference frame in which the single photon Stokes parameters are initially defined (induced by the non-uniform B-field) are quite dramatic, as it is evident from the polarization fraction (top row). In particular, for $\chi = 0$ (top-left panel) $\Pi_{\rm L}$ is almost everywhere far from unity, the value expected from the intrinsic degree of polarization

$$\Pi_{\rm L}^{\rm e} = \frac{|n_{\rm X} - n_{\rm O}|}{n_{\rm X} + n_{\rm O}} = 1\,, \tag{3.31}$$

and it becomes ~ 0.9 only at high energies ($E \sim 10$ keV). By increasing the LOS inclination ($\chi = 15°$, top-middle panel), the polarization fraction reaches unity for photon energies $\gtrsim 1$ keV, while at lower energies it is substantially smaller (between ~ 0.1 and ~ 0.8). Only when χ becomes sufficiently large (e.g. $\chi = 30°$, top-right panel), i.e. when the polar caps are not always in view during the star rotation, $\Pi_{\rm L}$ is unity almost everywhere in the plot, except at low energies ($\sim 1-10$ eV), where it drops to about ~ 0.6 corresponding to the phase intervals in which the polar regions enter in view. The behavior showed by $\Pi_{\rm L}$ as a function of E is due to the vacuum polarization and clearly reflects the dependence of $r_{\rm a}$ on the photon energy (see equation 2.23): the electric field of photons with lower energies decouples from the stellar magnetic field before that of more energetic photons. As a consequence, the α angles for low-energy photons take values in a wider range and the depolarization effect at infinity is stronger than for high-energy photons. Furthermore, besides being a function of the photon energy, the polarization fraction depends on γ and χ, which in turn enter in the α angle, as shown in the previous section.

The bottom row of Figure 3.3 illustrates the polarization angle for the same three simulations. Contrary of what happens for the polarization fraction, $\chi_{\rm p}$ does not depend on energy and exhibits an oscillatory behavior as a function of the rotational phase around a value of 90°. This means that the polarization angle does not depend on QED effects (the energy dependence enters, in fact, through the adiabatic radius $r_{\rm a}$), but only on geometry, as stressed at the end of section 2.3.2. The amplitude of the oscillations depends on the viewing angle: it is smaller ($\chi_{\rm p} \sim 80° - 100°$) for $\chi = 30°$, increasing as the angle between the LOS and the magnetic axis decreases ($\chi_{\rm p} \sim 70° - 110°$ for $\chi = 15°$); then it sweeps the entire range $[0°, 180°]$ for $\chi = 0°$ through a sort of discontinuity or "jump". This is further illustrated in Figure 3.4, which shows the polarization angle as a function of the rotational phase at a single energy ($E = 0.02$ keV), $\chi = 90°$ and different values of ξ for photons polarized in the X-mode (solid lines) and in the O-mode (dashed lines). The amplitude of the oscillation vanishes in the case of an aligned rotator seen equator-on ($\chi = 90°$, $\xi = 0°$) and increases for increasing ξ until the "jump" appears for $\xi = 90°$. The average value of $\chi_{\rm p}$, instead, does not change with χ and ξ, but it is fixed by the polarization mode of the seed photons: it is 90° for X-mode photons and 0° for O-mode ones. Actually, the mean value would be the same even if photons were not all polarized in the same mode at the surface; since the Stokes parameters for O- and X-mode photons have opposite

signs (see equations 2.37) and the polarization observables are obtained by summing the Stokes parameters over all photons, the mean value of $\chi_{\rm p}$ reflects the polarization mode which dominates.

It is important to stress, at this point, that the mean value of the observed polarization angle is not univocally associated to the two photon modes, but it depends also on the choice of the fixed reference frame (u, v, w), i.e. on the angle ψ introduced in section 3.1, through the expression of α (equation 3.23). If, for instance, $\psi = 90^\circ$ (so that the u-axis coincides with the Y-axis of the LOS frame), the situation depicted in Figure 3.4 would be reversed, with the polarization angle for X-mode photons oscillating around 0° and that for the O-mode ones around 90°. This means that a measurement of the polarization angle alone is not sufficient to disambiguate in what mode the collected photons are polarized, confirming that the collective polarization angle loses all the information about the original polarization modes (see equations 2.48 and 2.49). Of course, different choices of the ψ angle do not affect the polarization degree $\Pi_{\rm L}$, the amplitude of the oscillations of $\chi_{\rm p}$ and the shift of 90° between the mean values of $\chi_{\rm p}$ for X-mode and O-mode photons.

The effects of varying the magnetic field strength are illustrated in Figure 3.5, where $\chi = 15^\circ$, $\xi = 5^\circ$ and $B_{\rm pol} = 10^{12}$ G (left-hand panel), 10^{13} G (middle panel; this is the same case shown in Figure 3.3) and 10^{14} G (right-hand panel). Again, changes are mostly in the polarization fraction $\Pi_{\rm L}$ (top row). Overall, the polarization fraction is smaller when the magnetic field is lower (top-left panel), and increases for increasing $B_{\rm pol}$, reaching values ~ 1 (i.e. the intrinsic polarization degree) in almost the entire energy and phase ranges for $B_{\rm pol} = 10^{14}$ G. The variation of $\Pi_{\rm L}$ with $B_{\rm pol}$, together with the energy dependence discussed above, confirms that the polarization fraction is quite sensitive to QED effects. In fact the adiabatic radius $r_{\rm a}$ depends also on the intensity of the star magnetic field at the poles (see again equation 2.23), so that the adiabatic region is larger for NSs with stronger magnetic field. On the contrary, the polarization angle (bottom row) does not change, exhibiting the same oscillation between $\sim 70^\circ$ and $\sim 110^\circ$ at all values of $B_{\rm pol}$. The fact that the polarization angle is unchanged as the magnetic field intensity varies confirms that $\chi_{\rm p}$ does not depend on the vacuum polarization effects; the dependence on $r_{\rm a}$ cancels in the ratio between the Stokes parameters U and Q that appears in the definition of the polarization angle (see equation 2.43).

The phase-averaged polarization fraction (top row) and polarization angle (bottom row) as a function of the angles χ, ξ is shown in Figure 3.6 for two values of the energy, $E = 2$ eV (optical, left-hand column) and $E = 0.3$ keV (X-rays, middle column). Comparing the two polarization observables, it can be seen that the region in the $\chi - \xi$ plane where $\Pi_{\rm L}$ approaches zero corresponds to the transition between the two values (0° and 90°) assumed by $\chi_{\rm p}$. The transition is abrupt because the mean value of the polarization angle depends on which polarization mode dominates. Hence, even starting from photons all polarized in the X-mode, the observed radiation is 100% X-mode photons only for $\chi \gtrsim 40^\circ$ and $\xi \lesssim 20^\circ$ (see the top-left panel), and is still predominantly polarized in the X-mode in all the yellow region in the bottom-left panel, where the mean value of $\chi_{\rm p}$ is 90°. On the other hand, ordinary photons prevail in the green region (mean value of $\chi_{\rm p} = 0^\circ$), providing a maximum $\Pi_{\rm L}$ of $\sim 70 - 80\%$. The right-hand panel of Figure 3.6 illustrates the variation of the semi-amplitude of

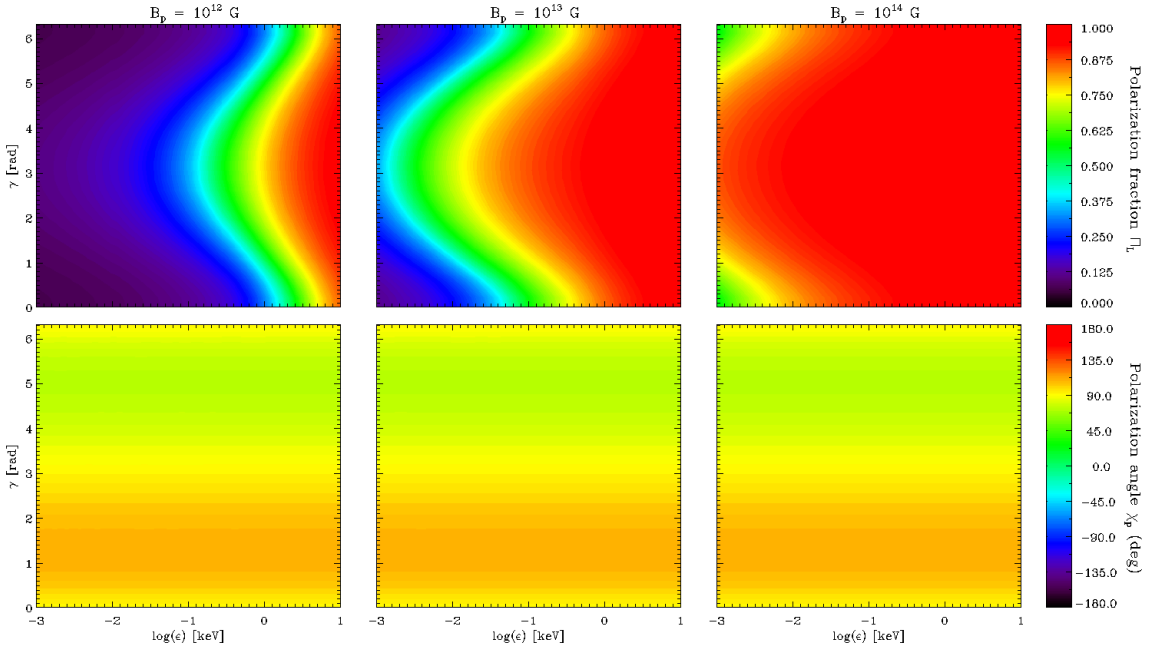

Figure 3.5: Same as in Figure 3.3 for $\chi = 15°$, $\xi = 5°$ and three different values of the magnetic field: $B_{\rm pol} = 10^{12}$ (left-hand column), 10^{13} (middle column) and 10^{14} G (right-hand column, Taverna et al., 2015).

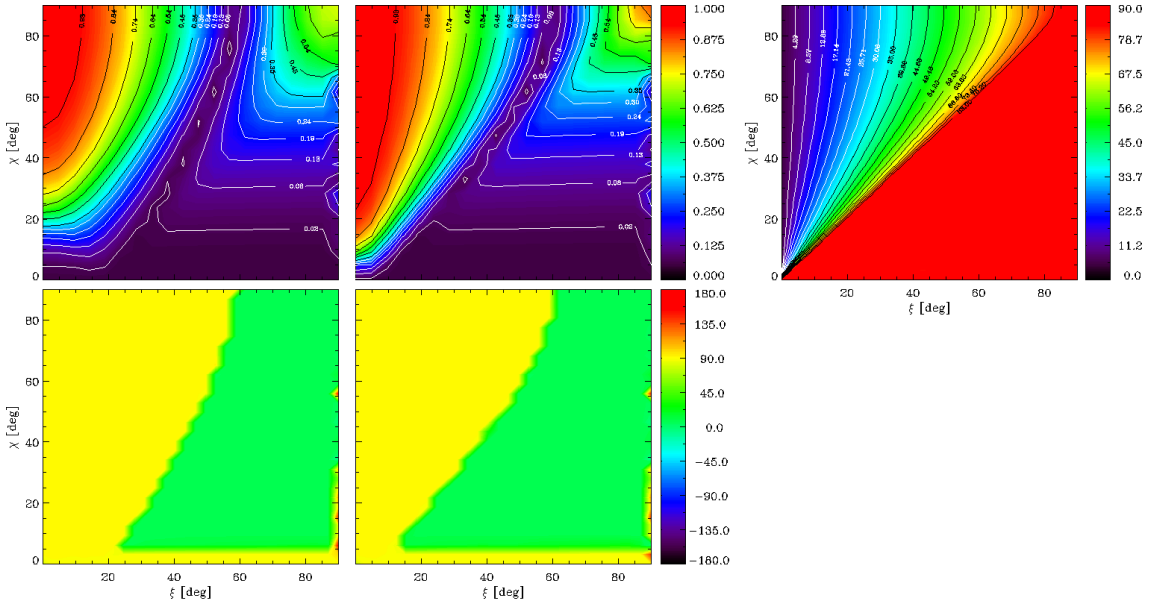

Figure 3.6: Contour plots for the phase-averaged polarization fraction and polarization angle at optical (2 eV, left-hand column) and X-ray (0.3 keV, middle column) energies, and of the semi-amplitude of the oscillations of the polarization angle (right-hand panel), as functions of χ and ξ. The values of $R_{\rm NS}$, $M_{\rm NS}$ and $B_{\rm pol}$ are the same as in Figure 3.3 (Taverna et al., 2015).

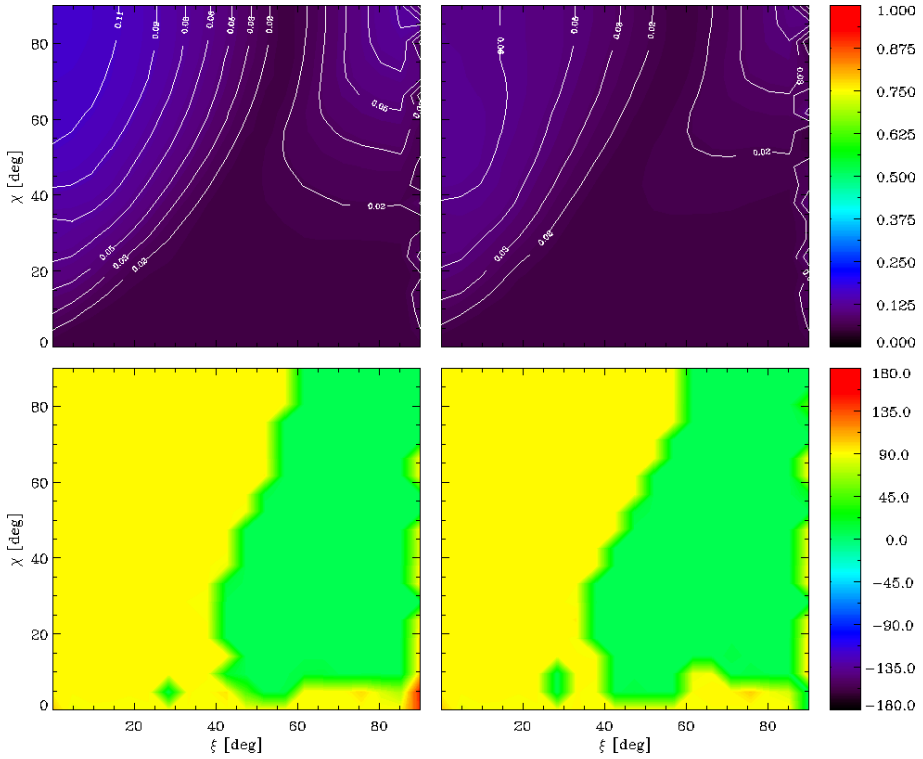

Figure 3.7: Contour plots for the phase-averaged polarization fraction and polarization angle at optical (2 eV, left-hand column) and X-ray (0.3 keV, right-hand column) energies, with the effects of vacuum polarization turned off (i.e. $r_{\rm a} = R_{\rm NS}$, so that no adiabatic region has been accounted for). The values of $R_{\rm NS}$, $M_{\rm NS}$ and $B_{\rm pol}$ are the same as in Figure 3.3.

$\chi_{\rm p}$. As already noted by Fernàndez & Davis (2011, see also Wagner & Seifert 2000), the amplitude is 180° for $\xi \lesssim \chi$, when the phase-averaged polarization degree attains its minimum value. In particular, $\chi_{\rm p}$ sweeps the entire range $[0°, 180°]$ when the region close to the magnetic pole is always in view during the star rotation, while the swing gets smaller for values of χ and ξ such that the polar region enters into view only at certain rotational phases (as seen in Figure 3.3). This behavior appears to be related to the α-angle distribution, and provides an explanation for the correlation between the swing by 180° of the polarization angle and the low phase-averaged polarization fraction at $\chi < \xi$. In fact, the regions where the polarization angle spans the widest range correspond to those in which at least one among the Stokes parameters Q and U takes all values between -1 and 1. Consequently, the phase-averaged polarization fraction, obtained by summing the Stokes parameters over a rotational cycle, turns out to be very small.

Figure 3.7 shows the contour plots of the phase-averaged polarization observables for optical and X-ray energies, as in the left-hand and middle columns of Figure 3.6, but with the effects of vacuum polarization turned off, i.e. taking $r_{\rm a} = R_{\rm NS}$, so that no adiabatic region is accounted for. As it can be clearly seen, in both the energy bands the phase-averaged polarization degree (top row) dramatically decreases with

respect to the case shown in Figure 3.6, where QED effects were considered, attaining a maximum value $\sim 11\%$ at optical energies, and $\sim 6\%$ at X-ray ones. This confirms what said before about the dependence of $\Pi_{\rm L}$ on the effects of vacuum polarization: if no adiabatic region is considered, the effects of Stokes parameter rotation operate in the direction of a drastic depolarization, since the α-angle distribution tends to sweep the entire range $[0, 2\pi]$. By locking the photon modes up to a sufficiently large distance from the star surface, QED prevents this depolarization effect, restricting the range in which the α-distribution takes values. Although the expression of the adiabatic radius used in Figure 3.7 ($r_{\rm a} = R_{\rm NS}$) is independent on the photon energy, $\Pi_{\rm L}$ exhibits anyway a residual energy dependence, which appears to be opposite to that in the presence of vacuum polarization: the polarization fraction is larger (smaller) for optical (X-ray) photons. This is a second order effect, related to the surface temperature map (see equation 3.30). In fact, since the integrals that give the collective Stokes parameters (see equations 3.26) include the surface intensity (that depends in turn on the surface temperature), one can expect a weak energy dependence of the polarization observables also if the adiabatic radius is taken to be constant. On the other hand, I proved that, chosing a constant temperature over the entire star surface, these weak energy dependence vanishes. The behavior of the phase-averaged polarization angle (bottom row) is, instead, quite similar to that for QED effects taken into account. This allows to recognize radiation that was polarized at the surface, despite the very low polarization fraction at infinity.

Finally, Figure 3.8 illustrates the effects on the polarization observables induced by the presence of a toroidal field component. The right-hand column shows the phase-energy contour plot of the polarization fraction (top panel) and a phase plot of the polarization angle at a fixed energy (bottom panel) for a globally twisted dipole field. The twisted field actually introduces a dependence of $\chi_{\rm p}$ on the photon energy; nevertheless, for the value of the twist angle considered here ($\Delta\phi_{\rm N-S} \simeq 50^\circ$), this dependence is quite small. The left-hand column shows for comparison the same quantities for a pure dipole with the same $B_{\rm pol} = 10^{13}$ G. The twisted magnetic field was evaluated using the analytical approximation by Pavan et al. (2009). Since relativistic corrections are unavailavle for a twisted field, they were not applied also to the dipole shown for comparison, whereas the ray bending is still considered in both the cases. The effects of the twist on the polarization fraction are quite modest and the variation of $\Pi_{\rm L}$ with photon energy and rotational phase is nearly the same as in the pure dipole case (see Figures 3.3 and 3.5). The only difference is in a slight overall decrease in the polarization degree. The twist of the external field affects much more the polarization angle, as it can be seen from the bottom row of Figure 3.8. The net effect is an overall asymmetry of the oscillations: $\chi_{\rm p}$ sweeps a larger angle in a half-period with respect to a purely dipolar case; this effect increases with the twist angle $\Delta\phi_{\rm N-S}$, as already noticed by Fernàndez & Davis (2011).

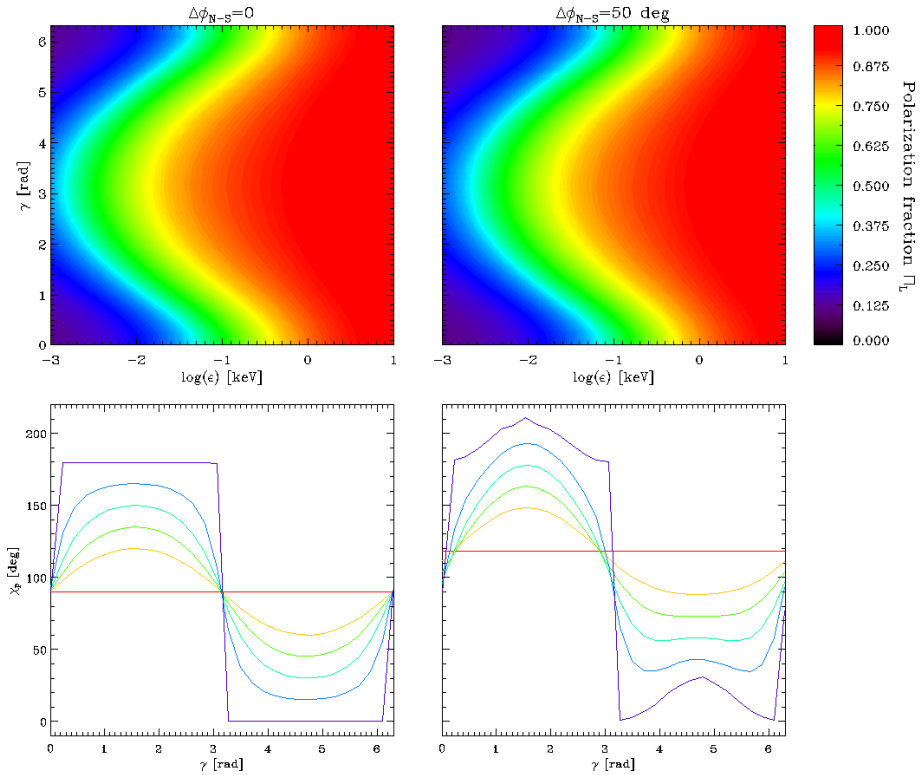

Figure 3.8: Polarization observables for the cases of a pure dipolar magnetic field (left-hand column) and a globally twisted dipole with twist angle $\Delta\phi_{\rm N-S} \simeq 50°$ (right-hand column). Top row: polarization fraction in the energy-phase plane for $\chi = 15°$ and $\xi = 5°$. Bottom row: polarization angle as a function of the rotational phase for a fixed photon energy ($E = 0.02$ keV), $\chi = 90°$ and $\xi = 0°$ (red), 30° (orange), 45° (green), 60° (light blue), 75° (blue) and 90° (violet). All the plots are obtained for seed photons all polarized in the X-mode and values of $R_{\rm NS}$, $M_{\rm NS}$ and $B_{\rm pol}$ as in Figure 3.3 (Taverna et al., 2015).

Chapter 4

Polarized emission from magnetar magnetospheres

AXPs and SGRs are among the best targets for X-ray polarimetric investigations thanks to their ultra-strong magnetic fields; moreover, in the operational energy range of state-of-art X-ray polarimeters, the expected photon counts are large enough to give good statistics within reasonable exposure times. As shown in section 1.4.4, the polarization pattern of the radiation emitted by magnetars is influenced by resonant cyclotron scattering (RCS) onto magnetospheric charged particles. Since the polarization observables are sensitive to the geometry of the source (see §3.3), X-ray polarization measurements can potentially reveal important information on the physical and geometrical properties of the magnetosphere, such as the velocity of charge carriers and the twist angle, that otherwise can not be assessed by spectral analysis alone. In this chapter I present the Monte Carlo code developed to compute the polarization properties of X-ray radiation excaping from magnetar magnetospheres, taking into account the effects of RCS as well as those of QED and geometry discussed in the previous chapters. The results of theoretical simulations, obtained for different values of physical and geometrical parameters, are also presented.

4.1 Monte Carlo code

RCS of primary thermal photons onto magnetospheric particles is dealt with using the FORTRAN code developed by Nobili, Turolla & Zane (2008a, see also Taverna et al. 2014), with the addition of a new module to solve the equations for the evolution of polarization modes in vacuo (see equations 2.38). According to the assumptions introduced in section 1.4.4, charge carriers are taken to be as electrons and ions (unidirectional flow), with spatial density $n_{\rm e}$ given by equation (1.23). In order to mimic the real scenario for magnetospheric particles, the electron motion is approximated with a bulk motion along the magnetic field direction, with bulk velocity $\beta_{\rm b}$ in units of the speed of light, superimposed to a 1D (relativistic) Maxwellian distribution at temperature $T = T_{\rm el}$, that accounts for the dispersion in the direction orthogonal to $\boldsymbol{B}$ (see Nobili, Turolla & Zane, 2008a; Taverna et al., 2014). The invariant distribution

function results

$$\frac{\mathrm{d}n_\mathrm{e}}{\mathrm{d}(\gamma\beta)} = \frac{n_\mathrm{e}\exp(-\gamma' m_\mathrm{e}c^2/kT_\mathrm{el})}{2K_1(m_\mathrm{e}c^2/kT_\mathrm{el})}\,, \tag{4.1}$$

where $\gamma' = \gamma\gamma_\mathrm{b}(1-\beta\beta_\mathrm{b})$ and K_1 is the modified Bessel function of the first order.

4.1.1 Scattering process

Once the magnetospheric structure is specified, providing in input the polar value B_pol of the surface magnetic field, the twist angle $\Delta\phi_{\mathrm{N-S}}$, the bulk velocity β_b and the temperature T_el of the electrons, the code follows the propagation of photons, as they interact with the magnetospheric charges. For the sake of simplicity, general relativistic effects (described in section 3.2) are not accounted for in this case; in fact, typical computing times for each run are of about 30 min for processing $\sim 10^6$ photons on an Intel core i7 2.30 GHz processor, and the full treatment that includes photon propagation along null geodesics would significantly increase the computing time, without adding much physical insight.

Photons are emitted from the cooling star surface with an assumed, isotropic blackboby distribution. The surface is divided into discrete, equal-area angular patches, each of them labelled with the values of the cosine of the magnetic colatitude $\mu = \cos\theta$ and the magnetic azimuth ϕ that identify its centre. The number of surface patches, their temperature and the number of photon emitted by each of them are inputs of the code. For the sake of generality, in the following I take an uniform temperature $T = 0.5$ keV on the whole surface, as well as an equal number of photons emitted from each patch. Also the intrinsic polarization fraction can be controlled patch by patch, choosing if photons are emitted all polarized in the X- or in the O-mode ($\Pi_\mathrm{L}^\mathrm{e} = 1$), or if the number of ordinary and extraordinary photons is equal ($\Pi_\mathrm{L}^\mathrm{e} = 0$). For the reasons discussed in the previous chapters, also in this case I assume that seed photons are 100% polarized in the X-mode for all the surface patches.

After the emission, the code evaluates the typical distance l traveled by a photon between two consecutive scatterings in the region where condition (1.24) for which RCS occurs is met. This is done integrating the infinitesimal optical depth

$$\mathrm{d}\tau_{\mathrm{i-j}} = \mathrm{d}l \int_{\beta_\mathrm{min}}^{\beta_\mathrm{max}} \mathrm{d}\beta \bar{n}_\mathrm{e}\gamma^3(1-\beta\cos\theta_\mathrm{Bk})\sigma_{\mathrm{i-j}} f_\mathrm{e}\,, \tag{4.2}$$

where $i, j = \mathrm{O}, \mathrm{X}$ and the first (second) index refers to the photon polarization mode before (after) scattering. Furthermore, in the previous equation, $[\beta_\mathrm{min}, \beta_\mathrm{max}]$ is the charge velocity spread, $\bar{n}_\mathrm{e}$ is the particle density (1.23) integrated over the velocities, $\sigma_{\mathrm{i-j}}$ are given by equations (1.29) and $f_\mathrm{e} = \gamma^{-3} n_\mathrm{e}^{-1}\mathrm{d}n_\mathrm{e}/\mathrm{d}\beta$ (see equation 4.1) is the momentum distribution function (Nobili, Turolla & Zane, 2008a). Introducing an uniform deviate U, the value of l is fixed by the condition

$$\tau_\mathrm{i} = \int_0^l \mathrm{d}\tau_\mathrm{i} = -\ln U\,, \tag{4.3}$$

with $\mathrm{d}\tau_i = \mathrm{d}\tau_{\mathrm{i-i}} + \mathrm{d}\tau_{\mathrm{i-j}}$ the (total) optical depth for a photon polarized in the mode i.

Integral (4.2) is performed by using a stepwise, fourth-order Runge-Kutta method. The integration is stopped as $\tau_{\rm i} \geq -\ln U$, and l is then obtained by extrapolating the values in the last two integration steps. Besides a reduction of the computational time required for a run, this approach is convenient also because it allows to control at each step if the resonant condition $\omega = \omega_{\rm D}$ holds (see equation 1.24). This happens when the two roots

$$\beta_{1,2} = \frac{1}{\cos^2\theta_{\rm Bk} + (\omega_{\rm B}/\omega)^2}\left[\cos\theta_{\rm Bk} \pm \frac{\omega_{\rm B}}{\omega}\sqrt{(\omega_{\rm B}/\omega)^2 + \cos^2\theta_{Bk} - 1}\right] \qquad (4.4)$$

obtained solving the resonant condition for β, are real, i.e. for $(\omega_{\rm B}/\omega)^2 \geq \sin^2\theta_{\rm Bk}$. If at a certain step this condition is found to be not satisfied, the code verifies if the photon moves towards the region where RCS is allowed or not; this is made possible by calculating numerically the tangent to the photon trajectory at $(\omega_{\rm B}/\omega)^2 \simeq \sin^2\theta_{\rm Bk}$. If yes, the procedure is repeated, otherwise the photon is left to freely propagate up to infinity, without any further interaction, and the code proceeds with the emission of a new photon (up to reach the maximum photon number set in input). Actually, to avoid that photons remain trapped in the magnetosphere, a maximum number of scatterings $N_{\rm max} = 1000$ is fixed, after which the photon is considered to be re-absorbed by the star surface.

Energy and direction of photons that scatter onto magnetospheric particles can be obtained from the cross sections (1.29). However, since the latter depend on the polarization modes of the incident and scattered photons, it is necessary to determine in what polarization state a photon initially polarized in the mode i emerges after the interaction. To this end a new uniform deviate U_1 is defined: if it results

$$U_1 > \frac{\sigma_{\rm i-i}}{\sigma_{\rm i-i} + \sigma_{\rm i-j}} \qquad (4.5)$$

the photon will change its original polarization state. It has to be noticed that, since $\sigma_{\rm O-O}/(\sigma_{\rm O-O} + \sigma_{\rm O-X}) = 1/4$ and $\sigma_{\rm X-X}/(\sigma_{\rm X-X} + \sigma_{\rm X-O}) = 3/4$ (see equations 1.29), it is more likely for an ordinary photon to change its polarization mode, while an extraordinary photon tends to maintain its original state. Given that the seed radiation is assumed to be polarized 100% in the X-mode, the number of O-mode photons that are expected to arise due to RCS is quite small (see Nobili, Turolla & Zane, 2008a). In doing this calculation, the photon polarization mode between two consecutive scatterings has been kept fixed: the validity of this approximation will be verified below.

The scattering electron velocity is decided between the two values β_1 and β_2 given by equation (4.4) through a similar method, by defininig the random number U_2 and comparing it with the ratios

$$R_{\rm O} = \frac{S_1(\beta_1)}{S_1(\beta_1) + S_1(\beta_2)} \qquad\qquad R_{\rm X} = \frac{S_2(\beta_1)}{S_2(\beta_1) + S_2(\beta_2)}\,, \qquad (4.6)$$

where

$$S_1(\beta_{1,2}) = \frac{|\cos\theta_{\rm Bk} - \beta_{1,2}|}{1 - \cos\theta_{\rm Bk}\beta_{1,2}} f_{\rm e}(\beta_{1,2}) \qquad S_2(\beta_{1,2}) = \frac{1 - \cos\theta_{\rm Bk}\beta_{1,2}}{|\cos\theta_{\rm Bk} - \beta_{1,2}|} f_{\rm e}(\beta_{1,2})\,. \qquad (4.7)$$

So, when $U_2 < R_\mathrm{i}$ ($U_2 > R_\mathrm{i}$) the i-mode photon scatters onto an electron with velocity β_1 (β_2). The photon frequency ω' after the interaction is then given by

$$\omega' = \gamma_{1,2}^2 \omega (1 - \beta_{1,2} \cos\theta_\mathrm{Bk})(1 + \beta_{1,2} \cos\theta') \,, \tag{4.8}$$

where, according to the angular dependence of the RCS cross sections (see Nobili, Turolla & Zane, 2008a), the magnetic colatitude θ' and azimuth ϕ' of the scattered photon are given by $\cos\theta' = 2U_3 - 1$ and $\phi' = 2\pi U_4$, respectively, with U_3, U_4 two further uniform deviates.

4.1.2 Stokes parameter evolution

Vacuum polarization evolution is switched on as soon as the escape condition is met, i.e. when the scattering probability becomes vanishingly small. This happens for $(\omega_\mathrm{B}/\omega)^2 = \sin^2\theta_\mathrm{Bk}$ that, for twisted fields (see equation 1.14), corresponds to a distance

$$\begin{aligned} r_\mathrm{esc} &= \left[\frac{F(\theta,p)}{2} \left(1-\mu^2\right)^{-1/2} \left(\frac{e B_\mathrm{pol}}{m_\mathrm{e} c\, \omega} \right) \right]^{1/(2+p)} \\ &\simeq 12 \left[\frac{F(\theta,p)}{2} \left(1-\mu^2\right)^{1/2} \left(\frac{B_\mathrm{pol}}{10^{14}\,\mathrm{G}} \right) \left(\frac{\hbar\omega}{1\,\mathrm{keV}} \right)^{-1} \right]_{\Delta\phi=1\,\mathrm{rad}}^{1/2.88} R_\mathrm{NS} \,, \end{aligned} \tag{4.9}$$

where $F(\theta, p)$ is given by equation (1.27) and it has been taken $p \simeq 0.88$ for a twist angle $\Delta\phi_\mathrm{N-S} = 1$ rad (Fernàndez & Davis, 2011). Since the distance r_esc is in any case smaller than the adiabatic radius r_a (see equation 2.23), scatterings occur well inside the adiabatic region. Hence, keeping fixed the photon polarization mode between two consecutive scattering is a good approximation; moreover, this allows to consider RCS and QED effects separately.

Photons arriving at the adiabatic radius are labelled by the Stokes vectors $(Q, U, V) = (\pm 1, 0, 0)$ (see equations 2.17) in the local frames $(x_\mathrm{i}, y_\mathrm{i}, z_\mathrm{i})$ described previously. At variance with the ray-tracing code discussed in chapter 3, here photons are emitted in all the possible directions and a preferred LOS does not exist; so, the stellar reference frame is chosen as the (p, q, t) frame shown in Figure 3.1b, with the t-axis along the magnetic axis $\boldsymbol{b}_\mathrm{dip}$. As a consequence, the unit vectors of the reference frame (x, y, z) (see Figure 4.1a) are still given by equations (3.5), provided that $\boldsymbol{\ell}$ is replaced by the photon wave vector $\boldsymbol{k}$ (characterized by the components k_p, k_q and k_t in the stellar frame):

$$\boldsymbol{z} \equiv \boldsymbol{k} \,, \qquad \boldsymbol{y} = \frac{\boldsymbol{k} \times \boldsymbol{B}}{|\boldsymbol{k} \times \boldsymbol{B}|} \,, \qquad \boldsymbol{x} = \boldsymbol{k} \times \boldsymbol{y} \,. \tag{4.10}$$

Again, in order to obtain the polarization observables as measured at infinity, the photon local frame (x, y, z) has to be rotated by an angle α up to coincide with a fixed frame (u, v, w) (see §2.3.2); this is done as soon as the photon has reached the boundary of the adiabatic region, before the integration of the equation system (2.38) that accounts for the Stokes parameter evolution is performed (see below). In the case at hand, however, the unit vectors that identify this fixed frame vary as the photon propagation direction changes: in particular, $\boldsymbol{w}$ is parallel to the photon wave vector

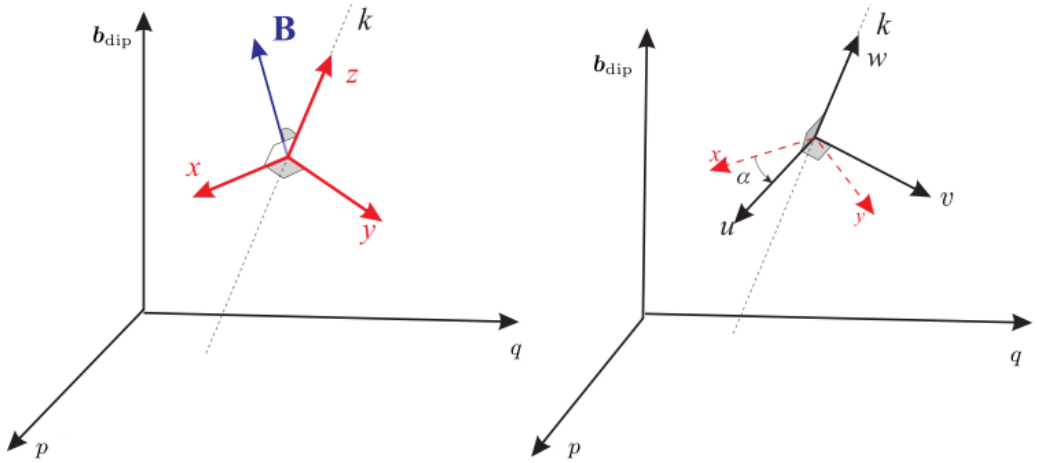

(a) (b)

Figure 4.1: The reference frames used in the Monte Carlo code. Left: the (x, y, z) reference frame with the z-axis always along the photon wave vector $\boldsymbol{k}$, the x-axis in the plane made by $\boldsymbol{k}$ and the local magnetic field $\boldsymbol{B}$ and $\boldsymbol{y} = \boldsymbol{k} \times \boldsymbol{x}$. Right: the (u, v, w) frame with the w-axis along the photon propagation direction $\boldsymbol{k}$, the u-axis perpendicular to both $\boldsymbol{w}$ and the star magnetic axis $\boldsymbol{b}_{\rm dip}$ and the v-axis obtained as $\boldsymbol{w} \times \boldsymbol{u}$. The α angle between $\boldsymbol{u}$ and $\boldsymbol{x}$, as well as the stellar frame (p, q, t), with the t-axis aligned with $\boldsymbol{b}_{\rm dip}$, are also shown (courtesy Luciano Nobili).

$\boldsymbol{k}$, $\boldsymbol{u}$ is chosen perpendicular to both $\boldsymbol{b}_{\rm dip}$ and $\boldsymbol{k}$ and the v-axis is given by the vector product between $\boldsymbol{k}$ and $\boldsymbol{u}$. Hence, a different (u, v, w) frame is associated to each direction $\boldsymbol{k}$, through the unit vectors

$$\begin{aligned} \boldsymbol{u} &= \left(\frac{k_q}{\sqrt{k_p^2 + k_q^2}}, -\frac{k_p}{\sqrt{k_p^2 + k_q^2}}, 0 \right) \\ \boldsymbol{v} &= \left(\frac{k_p k_t}{\sqrt{k_p^2 + k_q^2}}, \frac{k_q k_t}{\sqrt{k_p^2 + k_q^2}}, -\sqrt{k_p^2 + k_q^2} \right) \\ \boldsymbol{w} &= (k_p, k_q, k_t) \ , \end{aligned} \tag{4.11}$$

where $k_p^2 + k_q^2 + k_t^2 = 1$ (see Figure 4.1b). Then, as for the ray-tracing code described in chapter 3, for each photon direction the angle α is obtained by $\cos\alpha = \boldsymbol{x} \cdot \boldsymbol{u}$, and its sign is defined according to the sign of the scalar product $\boldsymbol{v} \cdot \boldsymbol{x}$ (if the latter is positive the rotation is by a negative angle α). The Stokes parameter rotation follows the same rules as in section 2.3.2 (see equations 2.39).

Then the integration of the differential equation system (2.38), that describes how Stokes parameters evolve due to vacuum polarization, is performed. In this way, all the three regions described above (adiabatic, intermediate and external regions, see Figure 2.2) are taken into account along the photon path. However, in order to avoid that too much computing time is spent when the photon is yet in the adiabatic region

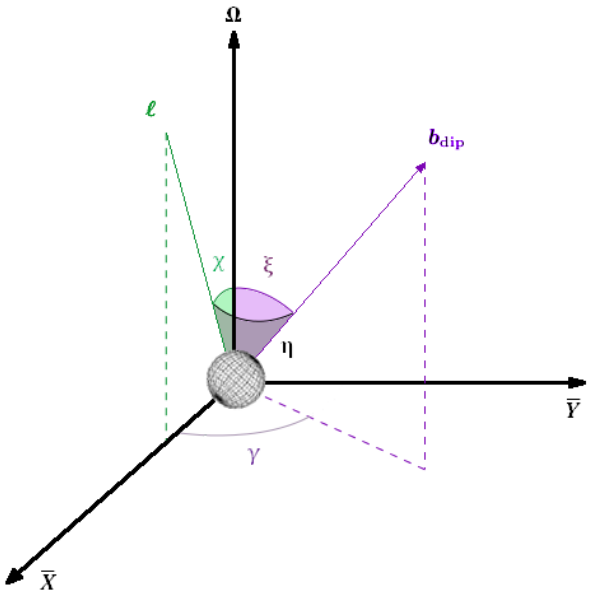

Figure 4.2: Reference frame $(\bar{X}, \bar{Y}, \bar{Z})$ used in the IDL script discussed in the text: the $\bar{Z}$-axis lies along the star spin axis $\boldsymbol{\Omega}$, the $\bar{X}$-axis is taken in the $\bar{Z} - \boldsymbol{\ell}$ plane, where $\boldsymbol{\ell}$ is the LOS unit vector, and the $\bar{Y}$-axis is perpendicular to both the $\bar{Z}$ and $\bar{X}$ axes. The angles χ, ξ, η and the rotation phase γ are also shown (Taverna et al., 2014).

(where the Stokes parameters are kept constant by QED effects) and to be sure, at the same time, that the entire intermediate region is accounted for, the adiabatic limit is taken a bit smaller than what equation (2.23) predicts, at $r'_{\rm a} < r_{\rm a}$. The integration is again performed, for each ray, through a fourth-order Runge-Kutta method, and it is stopped at a certain radius $r_{\rm max}$ at which the magnetic field has sufficiently decayed to affect no more the dielectric and magnetic permeability tensor components (so that the Stokes parameters freeze). After some experimenting, the value of the upper bound $r_{\rm max}$ has been fixed at $500\,R_{\rm NS}$. It is also possible to consider the effects of vacuum polarization with the simplified approach discussed in section 2.3.2, in which only the adiabatic and the external regions are present, divided by a sharp edge at $r = r'_{\rm a}$. In this case, the integration of equations (2.38) is skipped, allowing to considerably gain computational time (a typical run requires ~ 100 s instead of ~ 30 min).

Photons are eventually collected on the sky-at-infinity, i.e. on a spherical surface far enough that the NS appears point-like. The sphere is divided into discrete patches by an angular grid (much in the same way as the star surface when dealing with thermal emission), each characterized by the pair $(\mu_{\rm sky}, \phi_{\rm sky})$, which are the cosine of the magnetic colatitude and the magnetic azimuth of their centres. For each sky patch, the program returns the number of photons collected and their Stokes parameters, sorted according to the energy; the latter are computed by summing the values derived for single photons (see section 2.3.2).

4.2 Simulations

In order to reproduce a typical observation of magnetar X-ray emission, it is necessary to define a reference frame that conveniently describes the viewing geometry. In fact, as discussed above, the Monte Carlo code simulates photon emission from the star surface in all directions, regardless of the position of the observer at infinity, and the star is described in the (p, q, t) frame, without any reference to the direction of its spin axis. Hence, data generated by the Monte Carlo are re-processed with an IDL script, in which the direction of the observer LOS (unit vector $\boldsymbol{\ell}$) is introduced. The star is then described in a reference frame $(\bar{X}, \bar{Y}, \bar{Z})$, with the $\bar{Z}$-axis along the direction of the spin axis (unit vector $\boldsymbol{\Omega}$), the $\bar{X}$-axis in the plane made by $\boldsymbol{\Omega}$ and $\boldsymbol{\ell}$ and the $\bar{Y}$-axis perpendicular to both the $\bar{Z}$ and the $\bar{X}$ axes. As before, χ and ξ are the inclinations with respect to the spin axis of the LOS $\boldsymbol{\ell}$ and the magnetic axis $\boldsymbol{b}_{\rm dip}$, respectively, and γ is the rotational phase (see Figure 4.2). As γ varies in the range $[0, 2\pi]$, the polar angles η and ζ which the LOS makes with the magnetic axis change according to equations (3.2), simulating the star rotation.

4.2.1 Phase-averaged simulations

A first set of simulations has been obtained in the simplifying hypothesis of the star as an aligned rotator, i.e. $\xi = 0$, so that $\chi = \eta$; because of axial symmetry, data from Monte Carlo code are averaged with respect to the azimuthal angle ϕ in the $\boldsymbol{b}_{\rm dip}$ frame, that in this particular case coincides with the rotational phase γ. All the relevant quantities depend only on the photon energy and of the cosine of χ.

Results for some typical runs are presented in Figure 4.3, which shows the contour plots relative to the observed linear polarization fraction $\Pi_{\rm L}$ (top row), polarization angle $\chi_{\rm p}$ (middle row) and circular polarization fraction $\Pi_{\rm C}$ (bottom row) as functions of energy and $\cos\chi = \cos\eta$ for different values of the model parameters. In particular, by varying the left-hand and middle columns the effects of comparing the electron velocity, keeping all the other parameters fixed, can be assessed[1]. As follows from equation (1.23), the electron density scales as $|\langle\beta_{\rm b}\rangle|^{-1}$, so for lower values of the electron bulk velocity, the spatial density is higher, and photons undergo more scatterings. As a result, the linear polarization degree is overall smaller (radiation more depolarized) than for higher $\beta_{\rm b}$. The linear polarization fraction shows in addition a quite strong dependence on η and E, which is evident in all the three cases shown in Figure 4.3. At low energies, $\Pi_{\rm L}$ exhibits a clear asymmetry between the Northern and the Southern magnetic hemispheres (see also Fernàndez & Davis, 2011). This behavior is due to the assumed uni-directional flow of charged particles in the magnetosphere (see section 1.4.4). Electrons stream from the north towards the south pole, so that scatterings are more effective for photons coming from the Southern hemisphere (because collisions tend to be more "head-on"), while those from regions above the magnetic equator retain more their initial polarization state (here they are 100% polarized in the X-mode).

A comparison between the middle and the right-hand columns illustrates, instead, the effects of varying the twist angle $\Delta\phi_{\rm N-S}$, again with all other parameters held fixed.

[1] I checked that varying both $B_{\rm pol}$ and $T_{\rm el}$ has a very little effect on the polarization observables.

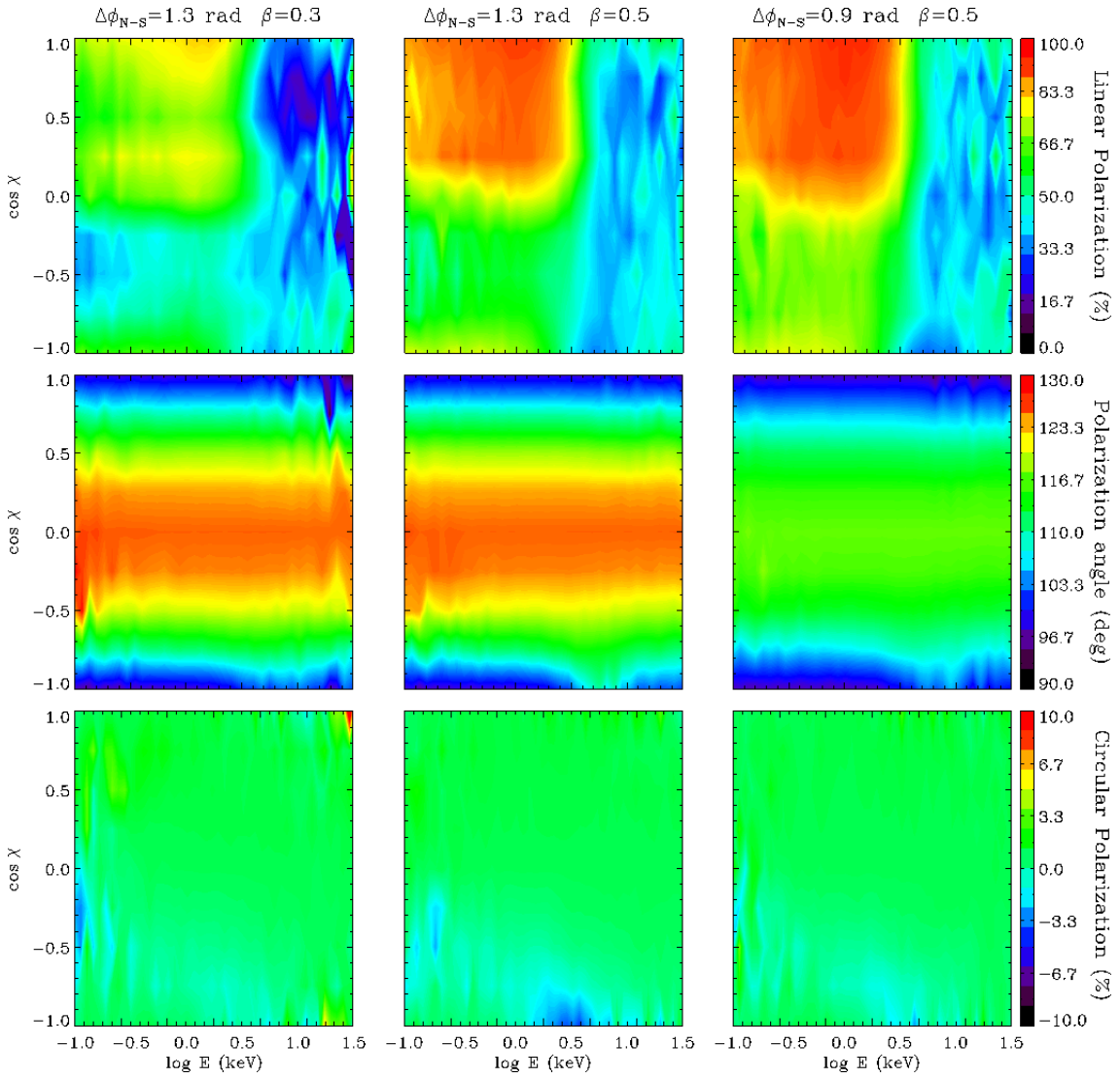

Figure 4.3: Contour plots for the observed linear polarization fraction (top row), polarization angle (middle row) and circular polarization fraction (bottom row) as functions of the photon energy and $\cos\chi = \cos\eta$ for different values of the twist angle and the electron bulk velocity: $\Delta\phi_{\rm N-S} = 1.3$ rad, $\beta_{\rm b} = 0.3$ (left-hand column); $\Delta\phi_{\rm N-S} = 1.3$ rad, $\beta_{\rm b} = 0.5$ (middle column); $\Delta\phi_{\rm N-S} = 0.9$ rad, $\beta_{\rm b} = 0.5$ (right column). In all runs, it is $B_{\rm pol} = 5 \times 10^{14}$ G and $T_{\rm el} = 10$ keV (Taverna et al., 2014).

Contrary to what happens by changing $\beta_{\rm b}$, now the variation affects both the linear polarization fraction and the polarization angle. The effect on $\Pi_{\rm L}$ can be understood by noticing that also the twist angle influences the charge density (see equations 1.17 and 1.23), so when $\Delta\phi_{\rm N-S}$ is larger RCS is more efficient and vice versa.

On the other hand, the behavior of $\chi_{\rm p}$ appears to be quite independent on scatterings: as seen also in section 3.3, in all the three panels the phase-averaged polarization angle as a function of energy is essentially constant, and deviations from its initial value of 90° (see Figure 3.6) are the same in the low- and high-energy ranges. Instead, the polarization angle strongly depends on the magnetosphere geometry (which is controlled by $\Delta\phi_{\rm N-S}$); it takes higher values as the twist increases, confirming what also Figure 3.8 shows. More precisely, it can be checked that (see Fernàndez & Davis, 2011; Taverna et al., 2014)

$$\chi_{\rm p} = \chi_{\rm p}^0 + \arctan\left(\frac{B_\phi}{B_\theta}\right) , \tag{4.12}$$

where $\chi_{\rm p}^0$ is a constant that depends on the choice of the (u, v, w) reference frame (see §3.3, in the case at hand $\chi_{\rm p}^0 = \pi/2$) and B_θ, B_ϕ are given by equations (1.14). The only relevant energy-dependent effect of RCS on the polarization angle is a small feature recognizable near the south magnetic pole, between $\sim$ 3 and 10 keV. This is also associated with the north-south asymmetry already mentioned, as noticed by Fernàndez & Davis (2011, see also Taverna et al. 2014). As a proof of the fact that this feature is due to RCS, it tends to disappear for low $\beta_{\rm b}$ and becomes more evident for higher velocities.

Finally, bottom row shows that, contrary to $\Pi_{\rm L}$ and $\chi_{\rm p}$, the circular polarization fraction is not so much affected by the variation of the electron bulk velocity and the twist angle. In particular, it can be seen a substantial deviation from zero of $\Pi_{\rm C}$ (anyway not larger than 1%) only in the Southern magnetic hemisphere ($\cos\eta = \cos\chi < 0$), across the almost entire range of energies. Such a behavior seems to correlate the presence of a small circular polarization degree with the scattering process, which is responsible for the north-south asymmetry in the plots. This is further confirmed by the fact that, for the largest values of $\Delta\phi_{\rm N-S}$ and $\beta_{\rm b}$ (middle panel), $\Pi_{\rm C}$ increases up to $5-6\%$ precisely in correspondence with the feature discussed just above for $\chi_{\rm p}$. Following Fernàndez & Davis (2011), this is due to the anisotropic nature of the scattered radiation (see e.g. the cross sections, equations 1.29). Starting from photons 100% linearly polarized in a transverse mode (either ordinary or extraordinary), a circular polarization degree can arise only due to the vacuum polarization, according to the last of equations (2.38). In the local reference frame (x, y, z) and taking only the leading term in δ (see equation 2.7), one has

$$\frac{{\rm d}V}{{\rm d}z} = (q+m)\sin^2\theta_{\rm Bk}\cos(2\phi_{\rm Bk})U + O(\delta^2) , \tag{4.13}$$

where q and m are given by equations (2.6). From the previous equation it becomes clear that the contribution to circular polarization fraction is a second-order effect in δ for linearly polarized seed photons (with $U = 0$), or anyway in the case of photons which propagate parallel to the B-field (with $\theta_{\rm Bk} = 0$). For non-radial photons, instead, $\theta_{\rm Bk}$ and $\phi_{\rm Bk}$ take different values along the photon path, according to how the magnetic

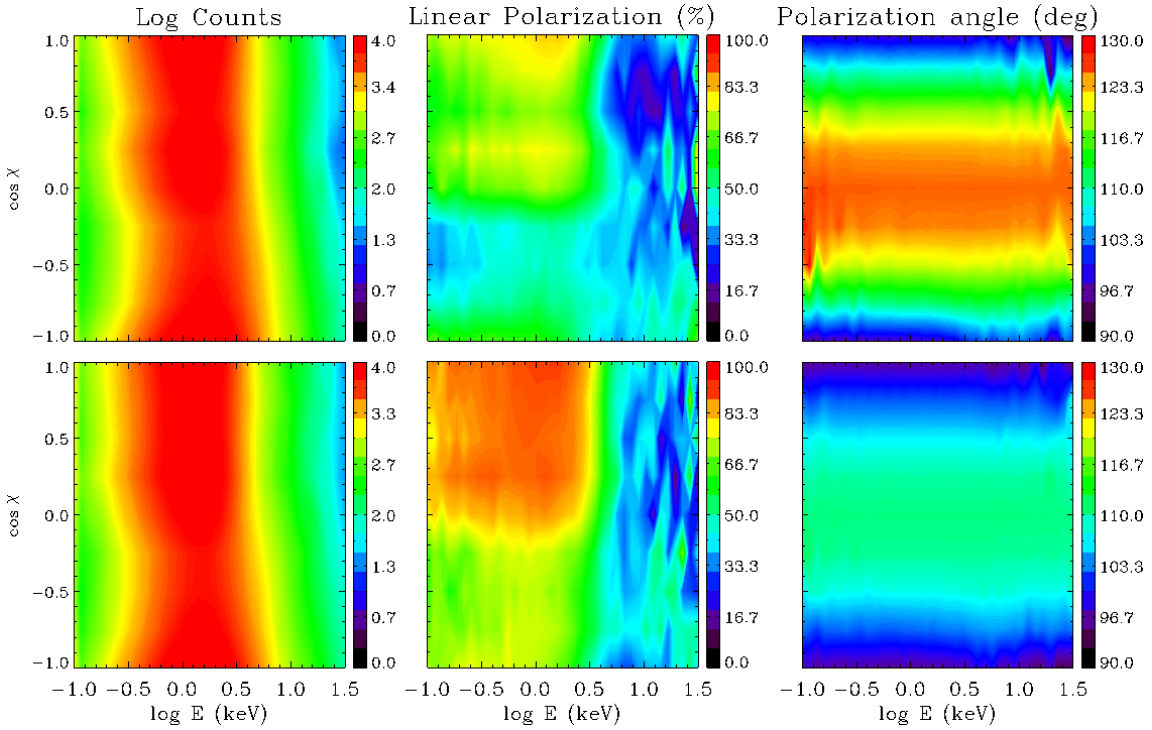

Figure 4.4: Contour plots for number of counts (in arbitrary units; left-hand column), linear polarization fracton (middle column) and polarization angle (right-hand column) as functions of the photon energy and $\cos\chi = \cos\eta$, for different values of the twist angle and the electron bulk velocity: $\Delta\phi_{\rm N-S} = 1.3$ rad, $\beta_{\rm b} = 0.3$ (top row) and $\Delta\phi_{\rm N-S} = 0.7$ rad $\beta_{\rm b} = 0.4$ (bottom row). In all runs, it is $B_{\rm pol} = 5 \times 10^{14}$ G and $T_{\rm el} = 10$ keV (Taverna et al., 2014).

field "rotates" around $\boldsymbol{k}$. If the radiation is perfectly isotropic, each non-radial photon trajectory has a counterpart for which the magnetic field rotates exactly in the opposite way, canceling all the contributions to $\Pi_{\rm C}$. However, since scattered radiation is not isotropic, some contributions to $\mathrm{d}V/\mathrm{d}z$ do not cancel anymore, giving rise to the amount of circular polarization fraction shown in the plots. Given that this amount is small, the Stokes parameter V, as well as $\Pi_{\rm C}$, can be neglected (as it has been done in section 2.3.2) without serious consequences.

In order to illustrate the effectiveness of polarimetric measurements in removing the degeneracy of the model, Figure 4.4 shows a series of simulations for different values of $\Delta\phi_{\rm N-S}$ and $\beta_{\rm b}$, in such a way to produce spectra which are very close to each other: the number of photons collected at infinity (left-hand column), the linear polarization fraction (middle column) and the polarization angle (right-hand column) are plotted as functions of $\cos\eta = \cos\chi$ and the photon energy. Although the plots for the photon spectrum are almost undistinguishable in the two cases, $\Pi_{\rm L}$ and $\chi_{\rm p}$ are dramatically different. This actually proves that measurements of polarization in magnetar X-ray emission could be of key importance to probe the different geometries of the magnetosphere, in addition to spectral analysis, which alone cannot, however, suffice.

4.2.2 Phase-resolved simulations

In this second case the star is not considered as an aligned rotator anymore; thus regions corresponding to different magnetic colatitudes enter into view as the star rotates. More precisely, according to the first of equations (3.2), the surface visibility range is $\chi - \xi \leq \eta \leq \chi + \xi$ (see Figure 4.2). Once the angles χ and ξ are fixed, the position on the sky-at-infinity at which all the (energy-dependent) quantities (the photon counts and the Stokes parameters) are extracted is known for each value of the rotational phase γ. A bilinear interpolation is actually used to obtain the values at arbitrary positions on the sphere starting from those at the patch centres.

An example of a typical phase-resolved output is shown in the top row of Figure 4.5, where the photon spectrum, linear polarization fraction and polarization angle as functions of the energy and rotational phase are plotted for $\chi = \xi = 90°$, corresponding to an orthogonal rotator seen perpendicularly to the spin axis. In this specific case, an observer can see all the surface as the star rotates, between the north (for $\gamma = 0, 2\pi$) and the south (for $\gamma = \pi$) magnetic poles.

The polarization angle confirms the oscillating behavior shown in the bottom-right panel of Figure 3.8, with the only exception that, for $\chi = \xi = 90°$, the mean value of the oscillations is expected to be 0° (see bottom panels of Figure 3.6). Thus, in the case at hand $\chi_{\rm p}$ takes values in the range $[90°, 130°]$, where the deviation from 90° is due to the presence of the twist (see equation 4.12). Actually, in the phase interval $[\pi, 2\pi]$ the polarization angle has been shifted by 180° for a better visualization of the behavior in the contour plot. Again, it shows little dependence on the energy, as expected from the phase-averaged results, apart from the feature localized near the south pole (i.e. around $\gamma = \pi$ in this case) and between $\sim$ 3 and 10 keV, due to the assumed uni-directional flow in the magnetosphere, as already discussed in section 4.2.1. On the other hand, on varying the phase, $\chi_{\rm pol}$ shows the maximum deviation

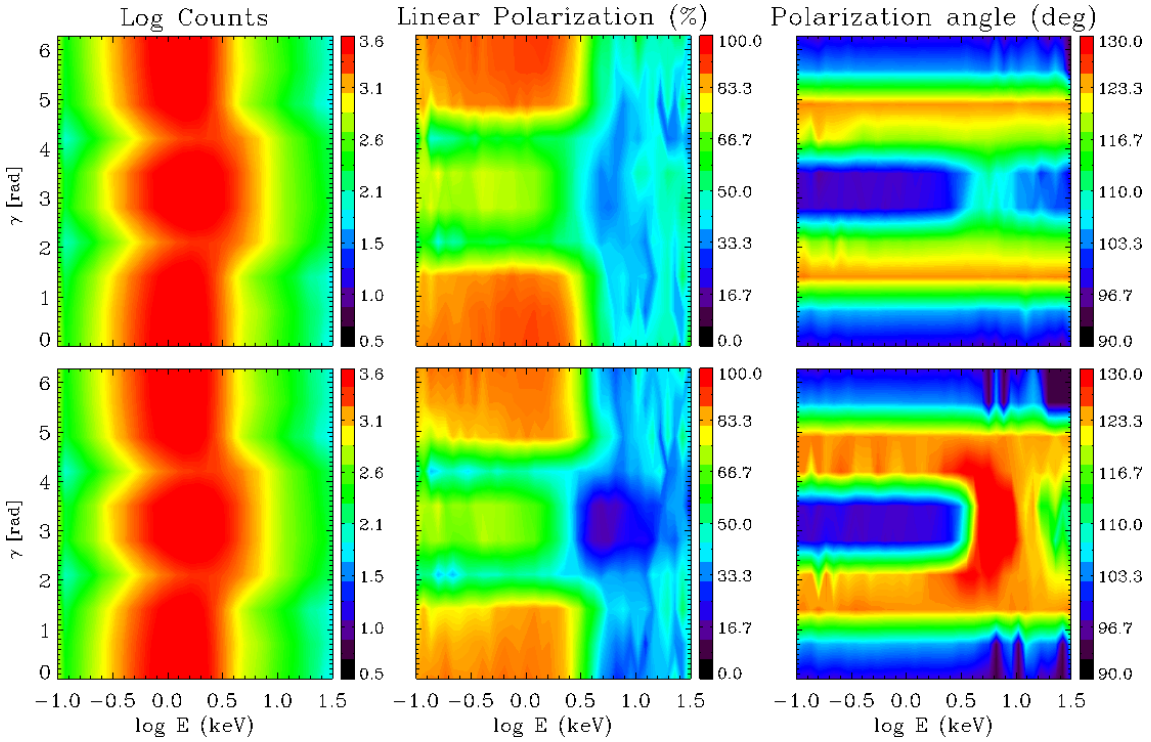

Figure 4.5: Number of counts (in arbitrary units; left-hand column), linear polarization fraction (middle column) and polarization angle (right-hand column) as functions of energy and rotational phase, for a simulation with $B_{\rm pol} = 4.6 \times 10^{14}$ G, $\Delta\phi_{\rm N-S} = 1.3$ rad, $\beta_{\rm b} = 0.5$ and $T_{\rm el} = 10$ keV. Plots in the top row are obtained integrating the full system (2.38), while those in the bottom row are obtained in the approximation of adiabatic and external region divided by a sharp edge at $r = r'_{\rm a}$. $\chi = \xi = 90°$ has been assumed (Taverna et al., 2014).

from the initial value of 90° which occurs almost exactly at the magnetic equator (seen twice, at $\gamma = \pi/2$ and $3\pi/2$).

Also the behavior of the linear polarization fraction (top-middle panel) is rather similar to that of the phase-averaged simulations. However, again for the asymmetry caused by the choice of the uni-directional flow, in the $\sim 0.1-3$ keV range the minimum value of $\Pi_{\rm L}$ occurs not in correspondence to the equator, as for the maximum value of $\chi_{\rm p}$, but just a bit below (for $\gamma \sim 2.1$ and 4.2 rad). In fact, as noticed in section 4.2.1, $\Pi_{\rm L}$ is quite sensitive to scattering, unlike $\chi_{\rm p}$. This is the main reason for which the behavior of the polarization angle is more symmetrical between the Northern and the Southern hemispheres than that of the polarization fraction, because the asymmetry is related only to scatterings.

The bottom row of Figure 4.5 shows again the number of counts, linear polarization fraction and polarization angle for the same values of the model parameters of the top row but with the integration of equations (2.38) switched off and the effects of vacuum polarization approximated as in chapter 3 (i.e. considering $r = r'_{\rm a}$ as a sharp edge between the adiabatic and the external regions). The photon spectrum is clearly the same, since it is not affected by vacuum polarization. The plots concerning the polarization observables are, instead, different: the most evident result is that integrating the full differential equation system acts in smoothing out the linear polarization fraction and polarization angle behaviors. Looking at $\Pi_{\rm L}$ (bottom-middle panel), an overall decrease of the polarization degree can be observed when the transition zone between the adiabatic region and the external one is neglected. This is due to the fact that, without integrating equations (2.38), the polarization modes start to change closer to the star surface, so that the depolarization effects of the Stokes parameter rotation are more important (see §3.3). On the other hand, the differences for $\Pi_{\rm L}$ are not so important, and are essentially due to the slight shift of the adiabatic boundary at $r'_{\rm a} < r_{\rm a}$ (see above). The two approaches return to give the same qualitative results by restoring the adiabatic limit at $r = r_{\rm a}$ in the "sharp-edge" approximation.

The polarization angle (bottom-right panel) appears to be much more affected by the absence of the transition region. In particular it shows a sharper dependence on energy near the south magnetic pole where, as discussed above, RCS effects are more important. This means that, contrary of what happens integrating equations (2.38), $\chi_{\rm p}$ is more sensitive to scattering effects.

Chapter 5

Polarized thermal emission from cooling neutron stars

In the previous chapters I discussed the polarization properties of radiation from highly magnetized NSs, in the simplifying assumptions of surface emission characterized by a (isotropic) blackbody distribution (with simple temperature profiles) and photons initially 100% polarized in the extraordinary mode with purely or globally twisted dipolar magnetic fields. However, the surface emission of these NSs is in general more complicated: according to the conventional picture, a gaseous atmosphere can reprocess the thermal radiation coming from the outermost stellar layers; alternatively, in the presence of strong magnetic fields a phase transition can occur, turning the atmosphere into a condensate and leaving "bare" the star surface (see §1.5). While the magnetospheric structure of magnetars, with the presence of returning currents that bombard the surface with high-energy charged particles, makes rather unlikely the formation of an atmosphere (at least of the type discussed in section 1.5), the magnetized atmosphere and condensed surface emission models are suited to describe the spectral properties of XDINSs, as mentioned in section 1.2. Therefore, in the following I present some simulations of the expected polarization pattern from cooling, highly magnetized NSs like the XDINSs, obtained using the ray-tracing code already described in chapter 3. The intrinsic polarization properties of the surface radiation predicted by the two models are reproduced in the code with the addition of specific modules that calculate the respective intensities. I take as a template the source RX J1856.5-3754, which is the brightest among the XDINSs and also the most promising for the study of polarized emission in the optical band, showing that polarization measurements can be crucial in understanding what is the nature of the surface emission in these sources.

5.1 Numerical implementation

The ray tracing code used in chapter 3 has been adapted to the study of RX J1856.5-3754 (RX J1856 hereafter), taking $R_{\rm NS} = 10$ km and $M_{\rm NS} = 1.4\,M_{\odot}$, so that the gravitational red-shift factor is $1 + z \simeq 0.76$. This source shows a nearly λ^{-4} optical-UV spectral energy distribution, with magnitude $V = 25.58$ (van Kerkwijk & Kulkarni, 2001; Kaplan et al., 2011) and a X-ray spectrum well modelled by two blackbody

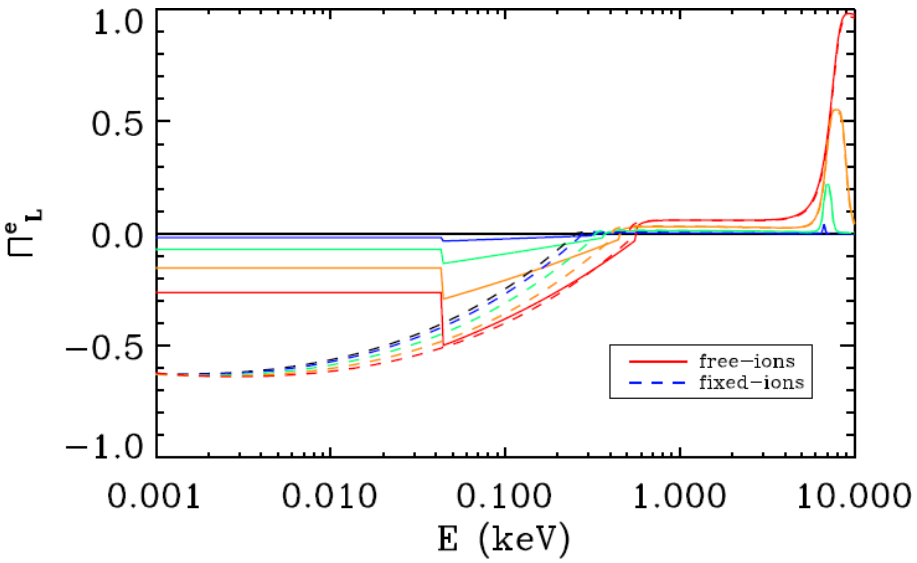

Figure 5.1: Intrinsic polarization degree for a bare NS with an iron condensed surface, as predicted by the model developed by Potekhin et al. (2012) in the free-ions (solid lines) and fixed-ions (dashed lines) limits. Here the polar magnetic field strength is fixed at $B = 1.5 \times 10^{13}$ G, $\theta_{\rm B} = 0°$, $\phi_{\rm k} = 0°$ and $\theta_{\rm k} = 0°$ (black), 15° (blue), 30° (green), 45° (orange) and 60° (red).

components, with temperatures (observed at infinity) $T_{\rm c}^{\infty} = 40$ eV and $T_{\rm h}^{\infty} = 60$ eV (Sartore et al., 2012). The measured X-ray pulsed fraction is $\sim 1.3\%$ (see Tiengo & Mereghetti, 2007), that is the lowest among XDINSs. An upper limit on the period derivative has been derived by van Kerkwijk & Kaplan (2008), $\dot{P} < 3 \times 10^{-14}$ s s^{-1}; this, together with the measured rotational period $P = 7$ s (Tiengo & Mereghetti, 2007), translates into an upper limit on the spin-down magnetic field of $B < 1.5 \times 10^{13}$ G; hence, in the code a purely dipolar magnetic field has been adopted, with $B_{\rm pol} = 1.5 \times 10^{13}$ G. If the upper limit is representative of the real value, a non vanishing degree of polarization is indeed expected in the thermal emission of the source. Consequently, the surface temperature distribution has been taken as described by equation (3.30), i.e. the modified core-centred dipole profile $T = \max(T_{\rm pol} |\cos\theta_{\rm B}|^{1/2}, T_{\rm eq})$, where the polar and equatorial temperatures are given respectively by

$$T_{\rm pol} = \frac{T_{\rm h}^{\infty}}{1+z} \qquad\qquad T_{\rm eq} = \frac{T_{\rm c}^{\infty}}{1+z}\,, \tag{5.1}$$

correcting the values at infinity of the analysis by Sartore et al. (2012) for the gravitational redshift.

5.1.1 Condensed surface emission

The emission from the condensed surface of a bare neutron star is described by using the analytical fitting formulae developed by Potekhin et al. (2012), that, besides the total (monochromatic) emissivity J_ν already calculated in section 1.5 (see equations

1.42 and 1.43), give also the emissivities in the two normal modes; these are functions of the magnetic field strength $B_{\rm pol}$, the photon energy E, the angle $\theta_{\rm B}$ between the local magnetic field $\boldsymbol{B}$ and the normal to the star surface $\boldsymbol{n}$, the polar angles $\theta_{\rm k}$ and $\phi_{\rm k}$ that identify the photon direction $\boldsymbol{k}$ with respect to $\boldsymbol{n}$ and the angle $\theta_{\rm Bk}$ between $\boldsymbol{k}$ and $\boldsymbol{B}$. In particular, the emissivity $J_{\nu,\rm X}$ for the X-mode photons[1] results

$$J_{\nu,\rm X} = \begin{cases} J_{\rm A,1} & \text{for } E < E_{\rm ci} \\ \\ J_{\rm B,1}(1-J_{\rm C}) + J_{\rm C}(1-R_{\rm L}) & \text{for } E \geq E_{\rm ci}\,, \end{cases} \tag{5.2}$$

where $E_{\rm ci}$ is the ion cyclotron energy and the auxiliary functions $J_{\rm A,1}$, $J_{\rm B,1}$, $J_{\rm C}$, and $R_{\rm L}$ are given in Potekhin et al. (2012) for both the free- and fixed-ions limits. The emissivity $J_{\nu,\rm O}$ for the O-mode photons can be derived using $J_{\nu,\rm X}$ and the total emissivity J_ν, using the identity

$$J_{\nu,\rm O} = 2J_\nu - J_{\nu,\rm X}\,. \tag{5.3}$$

Figure 5.1 shows the behavior of the intrinsic polarization fraction

$$\Pi_{\rm L}^{\rm e} = \frac{J_{\nu,\rm X} - J_{\nu,\rm O}}{2J_\nu} \tag{5.4}$$

predicted by the model for an iron condensed surface, plotted as a function of the photon energy, with $\theta_{\rm B} = 0°$, $\phi_{\rm k} = 0°$ and different values of $\theta_{\rm k}$. In both the free- and fixed-ions limits, O-mode photons (negative $\Pi_{\rm L}^{\rm e}$) dominate at lower energies, while a larger fraction of X-mode photons (positive $\Pi_{\rm L}^{\rm e}$) is expected at higher energies.

The specific intensities that characterize the emission model are obtained multiplying the emissivities by the radiance $B_\nu(T)$ of a blackbody (see equation 1.41); they in general depend on the photon frequency ν and direction $\boldsymbol{k}$, and on the position on the star surface of the emission point. Much in the same way as in chapter 3, the spectral and polarization properties at infinity are then computed by integrating the contributions of the surface elements which are into view at a given rotational phase γ. For the monochromatic flux detected by an observer at distance $D \gg R_{\rm NS}$ one has

$$F_\nu(\gamma) = \left(1 - \frac{R_{\rm s}}{R_{\rm NS}}\right) \frac{R_{\rm NS}^2}{D^2} \int_0^{2\pi} {\rm d}\Phi_{\rm S} \int_0^1 I_\nu(\boldsymbol{k}, \theta, \phi) {\rm d}u^2\,, \tag{5.5}$$

where $R_{\rm s}$ is the Schwarzschild radius and $u = \sin\bar{\Theta}$ is defined by the "ray tracing" integral (3.28). In this way, in analogy with the quantity defined by equation (5.4), the intrinsic polarization fraction as seen at infinity can be defined as

$$\bar{\Pi}_{\rm L}^{\rm e} = \frac{F_{\nu,\rm X} - F_{\nu,\rm O}}{2F_\nu}\,, \tag{5.6}$$

where $F_{\nu,\rm X}$ and $F_{\nu,\rm O}$ are the monochromatic, phase-dependent fluxes in each mode, defined as in equation (5.5).

Figure 5.2 shows the behavior of $\bar{\Pi}_{\rm L}^{\rm e}$ for free ions (top row) and fixed ions (bottom row) as a function of the viewing angles χ and ξ; plots in the left-hand column refer

[1] Mode 1 (2) of Potekhin et al. (2012) corresponds to the X (O) mode.

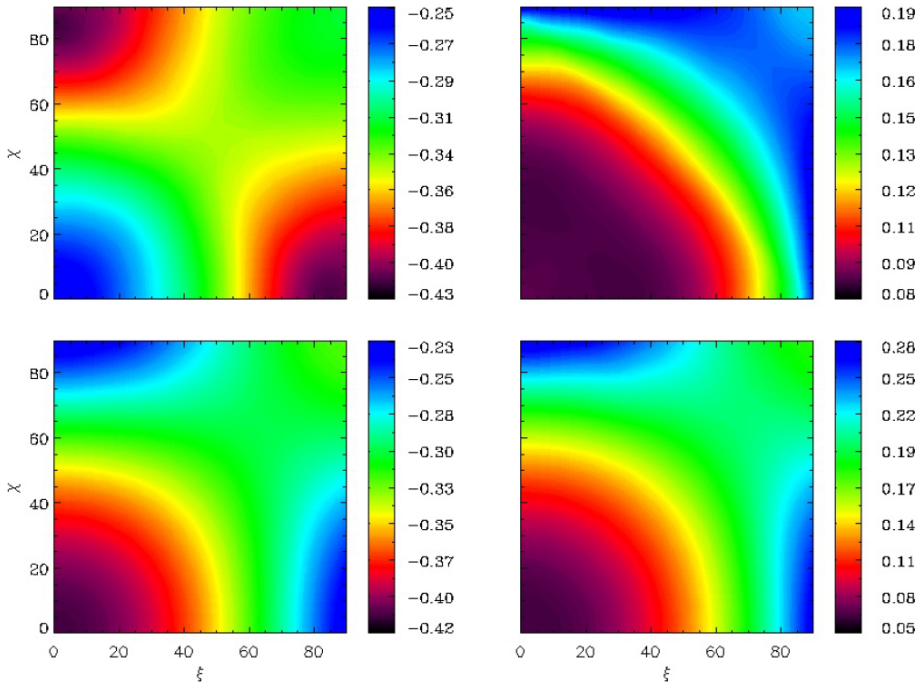

Figure 5.2: Intrinsic degree of polarization as seen at infinity for the emission from a condensed surface according to the model developed by Potekhin et al. (2012), in the free-ions (top row) and fixed-ions (bottom row) limits, plotted as a function of the angles χ and ξ in the optical band (left-hand column) and in the X-ray band (right-hand column). See text for details (Gonzàlez Caniulef et al., 2016).

to the optical band (energy range $2.5 - 3.1$ eV, B-filter), while those in the right-hand column to the X-ray band (energy range $0.1 - 0.5$ keV). Contour plots confirm the trend shown in Figure 5.1, i.e. optical photons are polarized mostly in the O-mode, while in the X-rays X-mode photons dominate. According to the model by Potekhin et al. (2012), condensed surface emission is only mildly polarized, with an intrinsic degree of polarization $\lesssim 40\%$ in the optical, and even lower ($\lesssim 28\%$) in the X-rays; in any case, this is far from the assumption of 100% X-mode photons made in chapter 3.

5.1.2 Atmospheric emission

As discussed in section 1.5, atmospheres around cooling NSs are commonly modeled by considering a gas in radiative and hydrostatic equilibrium. Due to the ultra-strong surface gravity $g_{\rm NS}$, the atmosphere scale height ($h \sim kT/m_{\rm p}g_{\rm NS} \sim 10$ cm) is small enough to allow solving the radiative transfer equation in the plane-parallel approximation. Different atmospheric models have been presented so far, accounting for different compositions and complexities (see Potekhin, 2014, for a review). For the sake of simplicity, and since the main goal in this chapter is showing how polarimetric measurements allow to probe the star emission mechanism, all the considerations in the following are based on the simple model of a pure H, fully ionized atmosphere. In the code, the emitted intensities in the two normal modes are calculated according to the numerical method developed by Lloyd (2003, see also Lloyd et al. 2003; Zane & Turolla 2006): it solves the stationary radiative transfer equation for the two modes in a plane-parallel slab through a complete linearization technique, taking into account, in the source term, magnetic Thompson scattering and magnetic Bremsstrahlung (see section 1.5.1).

Computed spectra are characterized by the (local) effective temperature T and magnetic field strength B, the surface gravity and the angle $\theta_{\rm B}$ between the local magnetic field and the surface normal $\boldsymbol{n}$. The star surface is then divided, through an angular grid, in different patches, labelled by the colatitude $\Theta_{\rm S}$ of their centres in the LOS frame (X, Y, Z) (see §3.1): $\Theta_{\rm S} = \{0^\circ, 10^\circ, 30^\circ, 50^\circ, 70^\circ, 90^\circ\}$. At each patch the magnetic field strength and direction (the angle $\theta_{\rm B}$) are calculated using expressions (3.7) and (3.8); hence, the temperature T is computed using equation (3.30) and the values of $T_{\rm pol}$ and $T_{\rm eq}$ given in equation (5.1). Since the choice of the photon trajectory has to be optimized to ensure fast convergence at different magnetic field strengths and inclinations (see Lloyd, 2003), the single atmospheric models (obtained for each values of $\Theta_{\rm S}$) are in general calculated using different integration grids in the photon phase space, and they are eventually reinterpolated over a common grid.

The code returns in output the emergent intensities $I_{\nu,{\rm O}}$ and $I_{\nu,{\rm X}}$ for the two photon modes, and the total intensity I_ν, all functions of the patch angle $\Theta_{\rm S}$, the photon energy E and the polar angles $\theta_{\rm k}$ and $\phi_{\rm k}$ that the photon wave vector $\boldsymbol{k}$ makes with the slab normal $\boldsymbol{n}$. The $\phi_{\rm k} = 0$ direction is defined by the projection of the magnetic field in the plane orthogonal to $\boldsymbol{n}$. Due to the symmetry properties of the opacities, the intensities in the southern magnetic hemisphere ($\theta_{\rm B} > 90^\circ$) can be obtained from those in the northern one through

$$I_\nu(\theta_{\rm B}) = I_\nu(180^\circ - \theta_{\rm B}) \quad \text{and} \quad I_{\nu,{\rm i}}(\theta_{\rm B}) = I_{\nu,{\rm i}}(180^\circ - \theta_{\rm B})\,, \tag{5.7}$$

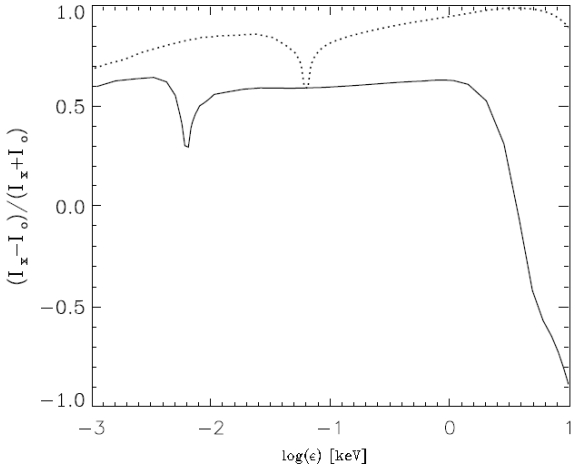

Figure 5.3: Intrinsic degree of polarization expected for the emission from a pure H, fully ionized atmosphere, according to the model developed by Lloyd (2003), plotted as a function of the photon energy for a plane-parallel slab with $T = 10^{6.5}$ K, $\theta_{\rm B} = 0°$, $B = 10^{12}$ G (solid line) and $B = 10^{13}$ G (dotted line). See text for details (Gonzàlez Caniulef et al., 2016).

where $i = \mathrm{O}, \mathrm{X}$. Finally, similar symmetry considerations allow to restrict the calculation in the range $0° < \phi_{\rm k} < 180°$, provided that, for $\theta_{\rm B} > 90°$, the value of $\phi_{\rm k}$ is shifted to $\tilde{\phi}_{\rm k} = 180° - \phi_{\rm k}$.

The behavior of the intrinsic polarization fraction, given by

$$\Pi_{\rm L}^{\rm e} = \frac{I_{\nu,\mathrm{X}} - I_{\nu,\mathrm{O}}}{I_{\nu,\mathrm{X}} + I_{\nu,\mathrm{O}}}\,, \tag{5.8}$$

is illustrated in Figure 5.3 as a function of the photon energy and in the case of a single slab, characterized by $\theta_{\rm B} = 0$ and for two different values of the polar magnetic field strength. Figure 5.4 shows instead the behavior of the intrinsic polarization degree as seen at infinity (derived integrating the intensities over the visible part of the star surface, see equations 5.5 and 5.6), as a function of the angles χ and ξ. The plot in the left-hand panel refers to the optical band, while that in the right-hand panel to the the X- rays, as in Figure 5.2. It can be seen that, for $B \gtrsim 10^{13}$ G, radiation reprocessed in a gaseous atmospheric layer is clearly dominated by the extraordinary photons ($\Pi_{\rm L}^{\rm e} > 0$), with a high intrinsic polarization degree ($\sim 100\%$), contrary to what happens for the condensed surface emission. The situation changes as the magnetic field varies: in particular at lower magnetic fields the number of ordinary photons with respect to that of extraordinary ones increases. Actually, this is due to the fact that, considering photon energies well below the electron cyclotron frequency, the mode opacities follow equation (2.1), for which $\kappa_{\rm X}$ is proportional to B^{-2}, while $\kappa_{\rm O}$ is pratically unaffected by the magnetic field intensity. As a function of the viewing angles χ and ξ, $\Pi_{\rm L}^{\rm e}$ shows a nearly constant behavior, similar in both the optical and X-ray bands, with a value $\sim 87\%$ at lower photon energies and only fractionally larger ($\sim 99\%$) in the X-rays.

As noticed in section 2.1.2 (see also Ho & Lai 2003), in the atmospheres around strongly magnetized NSs QED effects can induce a vacuum resonance, that occurs when

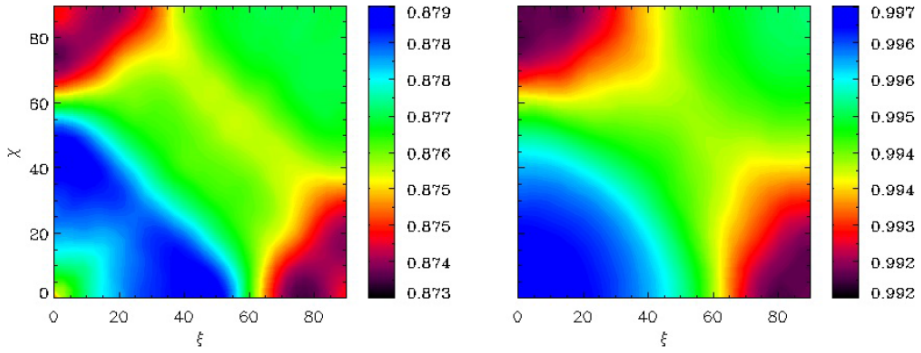

Figure 5.4: Intrinsic degree of polarization as seen at infinity for the emission from a pure H, fully ionized atmosphere, according to the model developed by Lloyd (2003), plotted as a function of the angles χ and ξ in the optical (left-hand panel) and in the X-ray (right-hand panel) bands (Gonzàlez Caniulef et al., 2016).

the density ρ equals the critical value $\rho_{\rm V}$ where vacuum and plasma contributions to the dielectric tensor are comparable (see equation 2.14). Near the vacuum resonance, a photon may convert from one mode into the other, significantly changing the intrinsic polarization pattern. This happens with probability

$$1 - P_{\rm jump} = 1 - \exp\left[-\pi \left(E/E_{\rm ad}\right)^3/2\right] \ , \tag{5.9}$$

where $E_{\rm ad}$ depends on the photon energy, the strength of the local magnetic field B and the angle $\theta_{\rm Bk}$ between the magnetic field and photon propagation directions (see van Adelsberg & Lai, 2006); hence, the maximum mode conversion probability is achieved for $P_{\rm jump} = 0$, that implies photon energies E much greater than $E_{\rm ad}$. Taking $B \lesssim 10^{13}$ G (as in the case at hand), it is $\rho_{\rm V} < 10^{-3}$ g cm^{-3}, i.e. the vacuum resonance is well outside the photospheres of both the ordinary and extraordinary mode photons. Moreover, the inequality $E < E_{\rm ad}$ holds for all photon energies $\lesssim 1$ keV, unless radiation is propagating nearly along the magnetic field direction ($\tan\theta_{\rm Bk} \lesssim 0.1$). For this reason, no mode conversion at the vacuum resonance has been assumed, that is equivalent to take $E \ll E_{\rm ad}$ (or $P_{\rm jump} = 1$) for all photons.

5.2 Results

The intensities calculated in both the atmospheric and the condensed surface cases are used in the main ray-tracing code, in order to include in the calculation of the polarization observables $\Pi_{\rm L}$ and $\chi_{\rm p}$ (see equations 2.42 and 2.43) the effects of vacuum polarization and geometry, as discussed in sections 3.1 and 3.2. The code can also generate the phase-resolved spectra for the different emission models. Moreover, as in chapter 3, all the calculations are performed assuming that the polarimeter frame (u, v, w) is coincident with the LOS frame (X, Y, Z), i.e. the angle ψ between the u and the X axes is zero. It should be remembered that a different choice of the angle ψ results in a shift of the polarization angle, while the polarization fraction is left unchanged (see section 3.3).

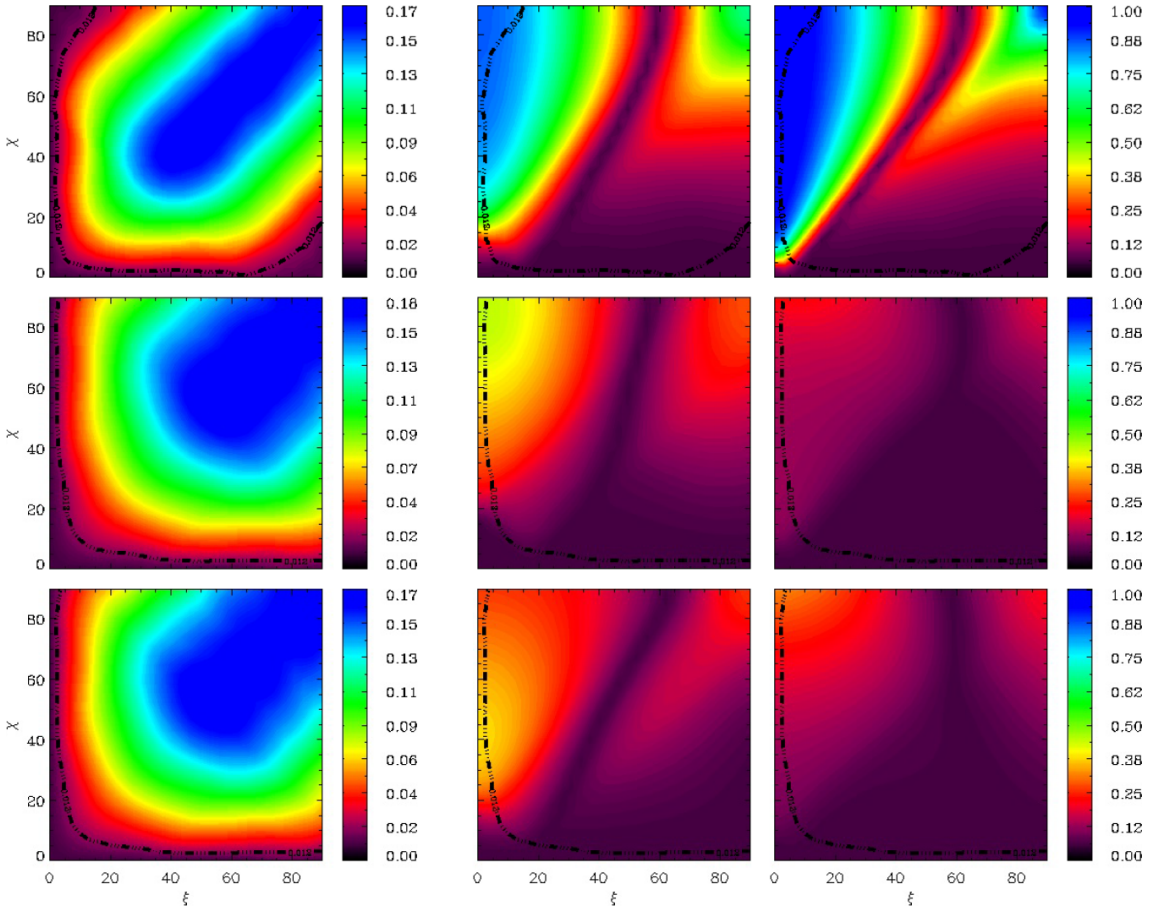

Figure 5.5: Contour plots for the X-ray pulsed fraction (left-hand column) and phase-averaged polarization fraction in the optical (middle column) and X-ray (right-hand column) bands for the atmospheric (top row) and condensed surface emission models, in the free-ions (middle row) and fixed-ions (bottom row) limits, as functions of the angles χ and ξ. The black line superimposed to all the plots corresponds to an X-ray pulsed fraction $\sim 1\%$, as measured for RX J1856, see text for details (Gonzàlez Caniulef et al., 2016).

Figure 5.5 shows the X-ray pulsed fraction (left-hand column) and the phase-averaged polarization fraction as measured at infinity in the optical (middle column) and in the X-rays (right-hand column), for radiation emitted from a magnetized atmosphere (top row) and a condensed surface, for both free ions (middle row) and fixed ions (bottom row), as functions of the angles χ and ξ. In all the panels the curve corresponding to an X-ray pulsed fraction of $\sim 1\%$ (that is the value measured for RX J1856) is also shown, in such a way to highlight the values of χ and ξ that are compatible with observations and the values of $\Pi_{\rm L}$ one can expect. A comparison between the three panels of the left-hand column shows that all the considered emission models exhibit a quite similar X-ray pulsed fraction. In particular, the 1% X-ray pulsed fraction observed in RX J1856 does not impose a strong constraint on the viewing geometry of the NS.

The viewing geometry and the source emission mechanism can be more easily assessed through optical or X- ray polarization measurements. In the case of emission from a magnetized atmosphere, the phase-averaged polarization fraction is substantial in large regions of the $\chi - \xi$ plane, at both optical and X- ray energies. This result is similar to that obtained in chapter 3 (see Figure 3.6) for simple blackbody emission and seed photons 100% polarized in the X-mode. In fact, also in the case at hand photons are expected to be initially polarized mostly in the X-mode, with an intrinsic degree of polarization close, although not equal, to 100% (see Figure 5.4). Taking into account QED and geometrical effects, the phase-averaged polarization fraction at infinity is globally reduced with respect to the intrinsic one, especially for $\chi > \xi$, owing to the effects of Stokes parameter rotation (as discussed in section 3.3). Nevertheless, viewing geometries near $\xi = 0^\circ$, $\chi = 90^\circ$ or $\xi = 90^\circ$, $\chi = 90^\circ$ (which correspond to consider the star as an aligned and an orthogonal rotator respectively, both seen perpendicularly to the spin axis) are particularly favorable for detecting a high phase-averaged polarization fraction, up to a maximum value $\sim 90\%$ in the X-ray band.

On the contrary, for the condensed surface emission the observed, phase-averaged polarization fraction is considerably lower in both the free-ions and fixed-ions limits, much in the same way as the intrinsic polarization degree for bare surface emission is much smaller than that in the case of the magnetized atmosphere (see Figure 5.2). In particular, the maximum value attained by $\Pi_{\rm L}$ is $\sim 40\%$ for free and $\sim 30\%$ for fixed ions, both in the optical band, while in the X- rays it is $\Pi_{\rm L} \lesssim 20\%$ in both the limits. This is at odds with what happens in the case of the atmosphere, where the phase-averaged polarization fraction is greater at higher photon energies. Also restricting to the region of the $\chi - \xi$ plane where the X-ray pulsed fraction is $\lesssim 1\%$, polarization measurements can still disambiguate if radiation is emitted from a magnetized atmosphere or a condensed surface: for atmospheric emission, the phase-averaged polarization fraction is generally larger by a factor 2 than for the case of a condensed surface, except for $\chi \sim 0^\circ$ (i.e. with the LOS pratically aligned with the rotation axis), when $\Pi_{\rm L}$ is very low in any case, due to geometrical effects.

Figure 5.6 illustrates, finally, the behavior of the phase-averaged polarization angle at infinity plotted as a function of the angles χ and ξ, again for the atmospheric emission (top row) and condensed surface, in both the free-ions (middle row) and fixed-ions (bottom row) limits. In the left-hand (right-hand) column the results in the optical band (X-ray band) are shown. In the case of a magnetized atmosphere, the

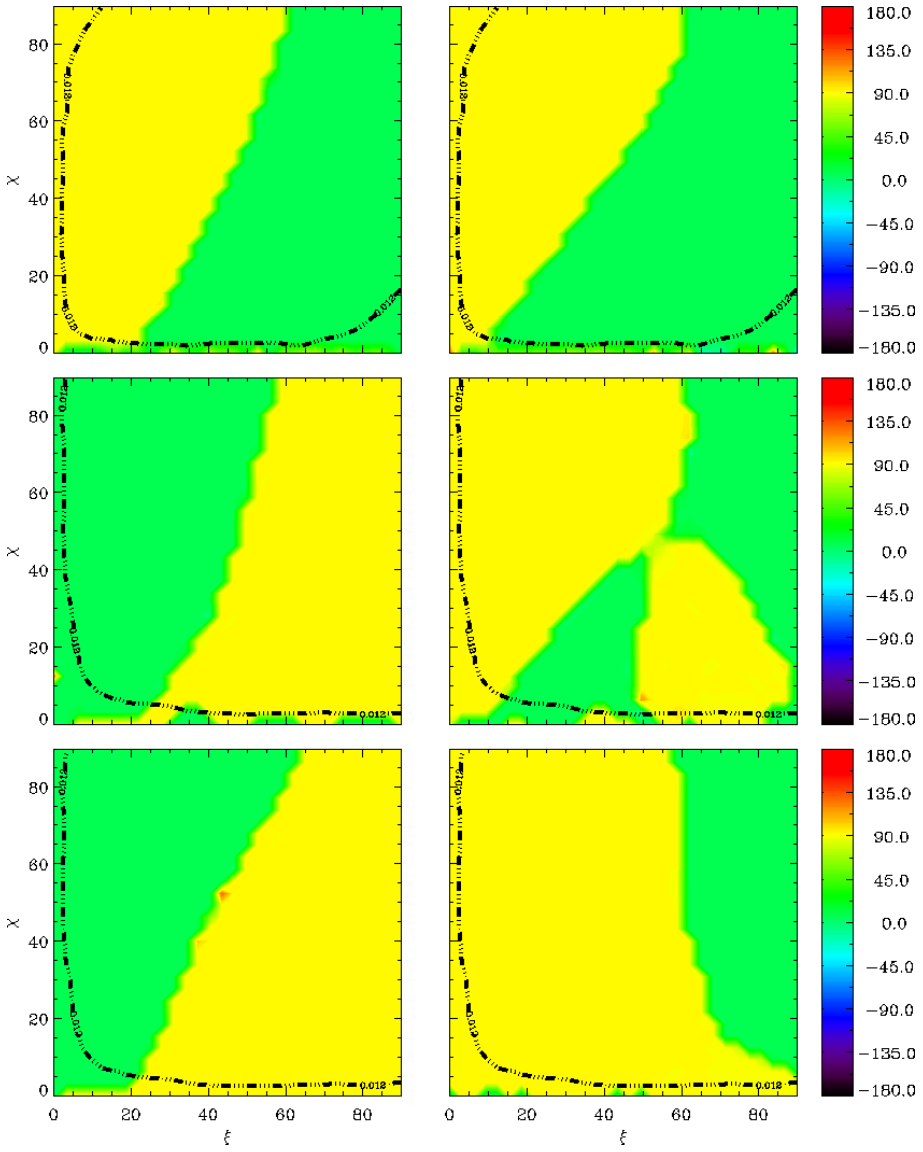

Figure 5.6: Phase-averaged polarization angle as a function of the angles χ and ξ for the cases of atmospheric (top row) and condensed surface emission, in the free-ions (middle row) and fixed-ions (bottom row) limits. Plots in the left-hand column have been obtained in the optical band, while those in the right-hand one in the X-ray band. The curve corresponding to X-ray pulsed fraction $\sim 1\%$ is also shown in all the plots, see text for details (Gonzàlez Caniulef et al., 2016).

behavior of the phase-averaged polarization angle is quite similar to that obtained in section 3.3 (see Figure 3.6), as discussed for the polarization fraction. The computed quantities attain only two constant values, namely 90° in the region $\chi < \xi$ and 0° for $\chi > \xi$. This is due again to the fact that the atmospheric model used in the code predicts a high intrinsic polarization fraction in both the optical and the X-ray bands, so that all the considerations made in section 3.3 for 100% X-mode photons are valid also in this case. The two different values of $\chi_{\rm p}$, shifted by 90°, can be associated to the two photon modes: in particular, assuming that the polarimeter frame (u, v, w) coincides with the stellar frame (X, Y, Z), $\chi_{\rm p} = 90°$ is associated to the extraordinary photons and $\chi_{\rm p} = 0°$ to the ordinary ones (see §3.3, see also Taverna et al. 2015). This means that, for viewing angles $\chi < \xi$, photons emitted at the surface as extraordinary are seen still polarized in the X-mode at infinity, while they appear polarizaed in the O-mode for $\chi > \xi$, due to the depolarization effects of Stokes parameter rotation.

In the condensed surface case, instead, the situation is quite different. In the optical band the values attained by $\chi_{\rm p}$ in the $\chi - \xi$ plane are reversed with respect to the atmospheric case, i.e. $\chi_{\rm p} \sim 0°$ for $\chi < \xi$ and $\chi_{\rm p} \sim 90°$ for $\chi > \xi$, for both free ions and fixed ions. In the X-rays the polarization angle behavior is again similar to that in the atmospheric case, although it appears quite irregular for free ions. This can be understood looking again at the polarization fraction; in fact, at the surface, extraordinary photons dominate only in the X-rays but with a low polarization degree ($\lesssim 19\%$ for free-ions, see the top-right panel of Figure 5.2), and is further diminished at infinity by geometrical effects (see Figure 5.5, middle-right panel). Since, as noticed in section 3.3, the phase-averaged polarization angle reflects the dominant polarization mode, for particularly low polarization fractions (so that the number of O- and X-mode photons is almost the same) $\chi_{\rm p}$ presents frequent "jumps" by 90°, depending on which of the two modes dominates. On the other hand, in the optical band surface radiation is dominated by ordinary photons (see Figure 5.2, left-hand column), with an intrinsic polarization fraction $\lesssim 40\%$; this explains why the values in middle-left and bottom-left panels are reversed with respect to the usual pattern.

Chapter 6

Observability of X-ray polarization signatures

The theoretical simulations presented in chapters 3 and 4 show that polarization measurements on the radiation emitted by astrophysical sources, such as highly magnetized NSs, provide key information about their physical and geometrical properties, allowing direct tests of theoretical models. As previously mentioned (see chapter 2), radio and optical polarimetry has been already exploited to resolve the viewing geometry in the case of some radio pulsars; moreover, current 8-m class telescopes (like the VLT) can potentially perform polarization measurements for faint optical sources like the XDINSs. While no definite results have been obtained so far in the X-rays, the situation is bound to change in the coming years, thanks to dedicated missions which have been proposed in 2015. In this chapter I briefly discuss the state-of-art X-ray polarimetry techniques, focusing in particular on the X-ray Imaging Polarimetry Explorer (XIPE) and the Imaging X-ray Polarimetry Explorer (IXPE) missions, recently selected in the study phase of ESA M4 and NASA SMEX programmes, respectively, since I am deeply involved in their science teams. I also present some simulated measurements, produced by a Monte Carlo code (described below), taking as a template the AXP 1RXS J170849.0-400910 (1RXS J1708 hereafter), one of the brightest known magnetars (with unabsorbed flux $\sim 21 - 35 \times 10^{-12}$ erg cm^{-2} s^{-1} in the $2 - 6$ keV range, see Rea et al., 2005; Campana et al., 2007).

6.1 X-ray polarimetry techniques

Current polarimeters for X-ray astrophysics are based on the dependence of Bragg diffraction, photoelectric effect or Compton scattering on the linear polarization of the incident radiation; it has been shown that all these techniques provide enough sensitivity for an astrophysical measurement. On the other hand, X-ray magnetic circular dichroism and the dependence of Compton scattering on circular polarization have not proven comparable efficiency as yet. For this reason, and given the low degree of circular polarization expected in highly magnetized NSs (see §4.2), circular polarization will not be considered in the following. Due to the choice of 1RXS J1708 as a test bed, and since the spectrum of several INSs that are bright in the X-rays peaks

around few keV, all the following considerations will be focussed on the $2 - 6$ keV energy range: here the polarization signatures are more evident and the measurements are easier to perform. Moreover, since XDINSs and AXPs/SGRs are relatively faint sources (the latter at least in their quiescence state), the use of an X-ray telescope is needed and, in this energy range, conventional telescopes based on grazing incidence can be easily exploited.

In this energy range, the most promising polarimeters are those based on the photolectric effect (Costa et al., 2001). They can measure the polarization of the beam, together with its spectrum, with a moderate energy resolution, of the order of 20% at 6 keV, and with an accurate timing of the event, usually at the level of few microseconds (Bellazzini et al., 2006; Black et al., 2007). Photoelectric polarimeters are based essentially on two different technologies: the gas pixel detector (GPD; Bellazzini et al., 2007; Bellazzini & Muleri, 2010), and the time projection chamber (TPC; Black et al., 2007). They give equivalent results in determining the polarization observables, but GPD, in addition, can provide also very good imaging capabilities (Fabiani et al., 2013; Soffitta et al., 2013), which are particularly useful for studying faint sources, allowing for a proper removal of the background. The GPD has been presented as a focal plane detector in a number of mission proposals, together with small (Costa et al., 2010), medium (Tagliaferri et al., 2012) or large (Bellazzini et al., 2010) area telescopes; among these, both the XIPE and IXPE missions are based on GPD technology. The operation of a typical GPD is illustrated in Figure 6.1a: once a photon hits the detector, a photoelectron is extracted, the path of which can be reconstructed thanks to the electron-ion pairs produced in the gas cell through ionization. The electrons are then accelerated by an electric field towards a gas electron multiplier (GEM), that amplifies the original signal before it is collected in the detector plane. Such instruments can detect only the azimuthal direction of the emitted photoelectrons, i.e. the angle φ between the projection of the photon track in the detection plane and the u-axis of the polarimeter frame (u, v, w) (see §3.1); they are, instead, unsensitive to the meridional distribution (the angle θ in Figure 6.1a).

Figure 6.1b shows instead a sketch of the operation of a typical Compton polarimeter, that, at variance with photoelectric polarimeters, is the most efficient at higher energies ($\gtrsim 30$ keV, see e.g. Muleri, 2014). This instrument is composed by different arrays of scintillator rods, that can work as scattering or absorbing elements (a single rod can work as both a scatterer and an absorber if all the elements are made by the same material). The direction of scattering is determined by the line which connects the scatterer and the absorber hit in each detected event. Albeit such instruments could in principle give information also on the meridional distribution of the events (giving the w components in the polarimeter frame of the scatterer and the absorber rods), this would be quite demanding in terms of operational time, due to the low energies normally related to each event. For this reason, also Compton polarimeters are optimized for an azimuthal response, much in the same way as the photoelectric ones.

In general, polarization in X-rays is derived from the measured modulation curve, which is basically the histogram of the azimuthal response of the instrument. For example, the modulation curve for photoelectric polarimeters is the histogram of the azimuthal direction of the emitted photoelectrons (Bellazzini & Spandre, 2010). In the

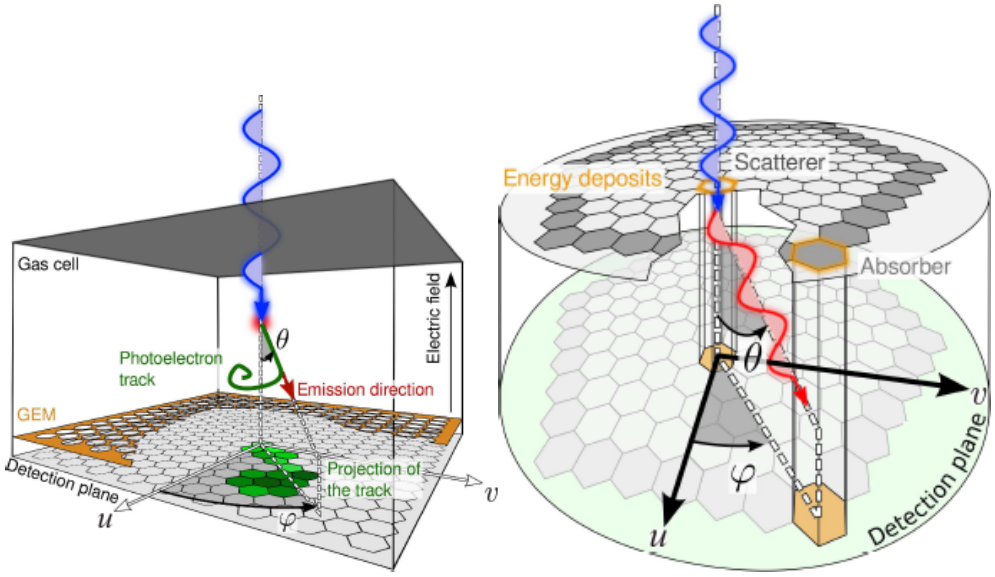

(a) (b)

Figure 6.1: Operation scheme of a GPD (a) and a Compton polarimeter (b). The polarimeter frame (u, v, w) and the angles of the emitted (scattered) electron are also indicated (Muleri, 2014).

case of polarized photons, the modulation curve shows a cosine square modulation

$$\mathcal{M}(\varphi) = A + B\cos^2(\varphi - \varphi_0)\,, \tag{6.1}$$

where the "flat term" A, the "modulated term" B and the phase φ_0 are free parameters that allow to reconstruct the polarization of the incident radiation. In particular φ_0 is related to the polarization angle by

$$\chi_{\rm p} = \varphi - \varphi_0 + \delta\varphi\,, \tag{6.2}$$

where $\delta\varphi = 0°$ in the case of photoelectric polarimeters and 90° in the case of Compton ones. The amplitude of the modulation is instead proportional to the degree of polarization and to the modulation factor $\bar{\mu}$, which is the amplitude of the intrumental response to 100% polarized photons:

$$\Pi_{\rm L} = \frac{1}{\bar{\mu}}\frac{\mathcal{M}_{\rm max} - \mathcal{M}_{\rm min}}{\mathcal{M}_{\rm max} + \mathcal{M}_{\rm min}} = \frac{B/\bar{\mu}}{2A + B}\,, \tag{6.3}$$

where $\mathcal{M}_{\rm max}$ ($\mathcal{M}_{\rm min}$) is the maximum (minimum) of the modulation amplitude.

Since a cosine square modulation is positive definite, and due to the statistical nature of the measurement, a problem arises when unpolarized radiation is observed. In fact, in place of the expected flat distribution a small modulation will be always detected because of statistical fluctuation of the contents of each phase bin. The situation is illustrated in Figure 6.2, where the real response of a GPD to polarized radiation is shown. In order to determine when the observed signal corresponds to

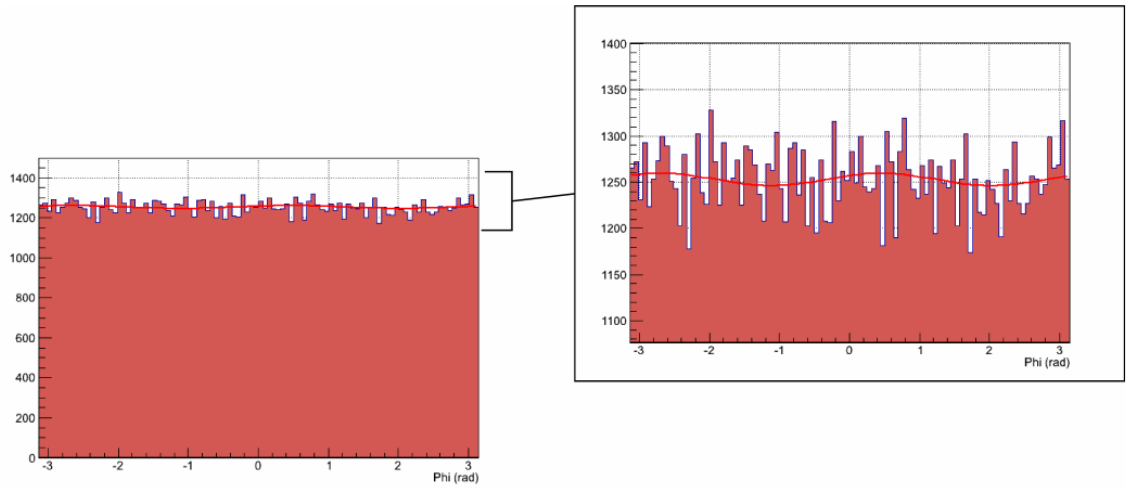

Figure 6.2: Real response of a photoelectric polarimeter (GPD) to unpolarized radiation. The colored field corresponds to the histogram of the azimuthal response of the instrument, while the red curve is the modulation curve $\mathcal{M}(\varphi)$ (Muleri et al., 2012).

unpolarized radiation or not, one defines the minimum detectable polarization (MDP), at 99% of confidence level, as

$$\mathrm{MDP} = \frac{4.29}{\bar{\eta} F \bar{\mu}} \sqrt{\frac{B + \bar{\eta} F}{S \Delta T}}\,, \tag{6.4}$$

where $\bar{\eta}$ is the instrument efficiency, F and B are the signal and background count rates, respectively, and ΔT is the exposure time. The MDP is the polarization degree associated to the amplitude of the modulation function detected in response to unpolarized photons, assuming that the content of the modulation curve bins is Poisson-distributed. This means that signals characterized by a polarization degree greater than the MDP actually correspond to polarized radiation with a probability of 99%. Although the MDP cannot be defined properly as the instrument sensitivity, it can be used to compare the sensitivities of different polarimeters.

6.2 Simulated polarization measurements

In order to derive the values of the polarization observables which would be measured by the instrument, and the associated errors, the Monte Carlo technique developed by Dovčiak et al. (2011) has been used. The purpose of this Monte Carlo code is to produce a number of "trial" modulation curves in the energy range of interest, fit them with a cosine square function and derive for each trial an estimate of the polarization observables which are measured from that modulation curve. The number of entries in the histogram is instead the number of collected events in the considered energy interval, obtained by multiplying the source spectrum by the collecting area of the telescope and by the instrument efficiency, using the response matrix of the instrument, including its energy resolution. Each trial is affected by a different Poisson

noise in the number of entries per azimuthal beam; systematic effects, proven to be lower than 1% for the GPD (Bellazzini & Muleri, 2010), are neglected. In defining the energy interval, the code takes into account the finite energy resolution of the instrument. The "measured" angle and degree of polarization which are provided by the Monte Carlo are the values derived by a random trial, whereas their errors are the average values over all trials. The efficiency and the modulation factor of the GPD are discussed in detail in Muleri et al. (2008, 2010); the collecting area, together with other instrumental features, is given in Weisskopf et al. (2013) for IXPE and in the dedicated website for XIPE[1].

The simulated measurement have been obtained using the parameter values of the template source 1RXS J1708[2]. The source period and period derivative are $P \simeq 11$ s and $\dot{P} \simeq 1.9 \times 10^{-11}$ s s^{-1}, respectively, implying a dipole field of 4.6×10^{14} G. The estimated source distance is ~ 3.8 kpc (Durant & van Kerkwijk, 2006) and the column density derived by Rea et al. (2005), $N_{\rm H} = 1.48 \times 10^{22}$ cm^{-2}, has been adopted. Spectral fits to high-statistics XMM-Newton data of 1RXS J1708 with the XSPEC model by Nobili, Turolla & Zane (2008a) have been presented in Zane et al. (2009). The best fitting parameters (see §4.1) are $T = 0.47$ keV, $\beta_{\rm b} = 0.34$ and $\Delta\phi_{\rm N-S} = 0.49$ rad, with the electron temperature set to $T_{\rm el} = 10$ keV; the column density, $N_{\rm H} = 1.45 \times 10^{22}$ cm^{-2}, is fully in agreement with that obtained by Rea et al. (2005). No estimate of the angles χ and ξ could be derived, since the model by Nobili, Turolla & Zane (2008a) is angle averaged, nor it has been obtained by other means.

The study of magnetar sources with similar properties to 1RXS J1708 is in the core science for XIPE and IXPE missions; for this reason a total observation time of $500 - 1000$ ks could be reasonably assumed. The simulations presented in the following are phase resolved, and performed assuming an exposure time of 1 Ms. The simulated source photon spectrum is then generated, for a given set of parameters, by the Monte Carlo code presented in section 4.1, including the full integration of equations (2.38) to account for the vacuum polarization effects; in order to produce phase-resolved polarization observables, data are collected in nine, equally spaced, phase bins.

A first simulation is shown in Figure 6.3, where the XIPE simulated data for $T = 0.47$ keV, $\beta_{\rm b} = 0.34$, $\Delta\phi_{\rm N-S} = 0.49$ rad, $\chi = 60°$ and $\xi = 30°$ are compared with the model. The three panels refer to the $2 - 6$ keV pulse profile (top), linear polarization fraction (middle) and polarization angle (bottom). The filled circles with error bars show the XIPE simulated measurements, while the solid lines represent the models computed for the parameter values mentioned above and different values of ξ (the model from which the simulated data were derived is shown by the black curve). As a matter of fact, while the polarization angle is almost independent on the energy, one can derive the average degree of polarization of each model in the $2 - 6$ keV energy range by simply weighting the phase-resolved polarization spectrum $P(E, \gamma)$ with the photon spectrum $S(E, \gamma)$, that is

$$P(\gamma)_{2-6\,\rm keV} = \frac{\int_{2\,\rm keV}^{6\,\rm keV} P(E,\gamma) S(E,\gamma) {\rm d}E}{\int_{2\,\rm keV}^{6\,\rm keV} S(E,\gamma) {\rm d}E} \,, \tag{6.5}$$

[1] http://www.isdc.unige.ch/xipe/

[2] See the McGill online magnetar catalogue at http:// www.physics.mcgill.ca/pulsar/magnetar/main.html and references therein.

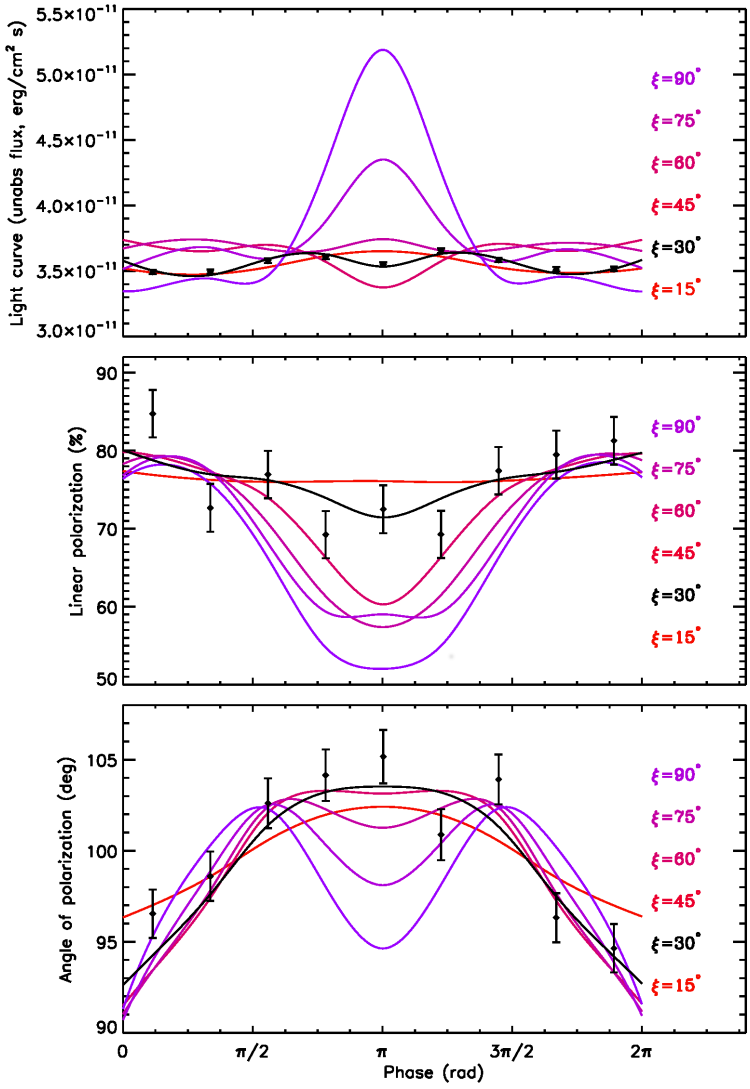

Figure 6.3: Pulse profile (top panel), phase-resolved polarization degree (middle panel) and polarization angle (bottom panel) for a set of models with the same viewing direction ($\chi = 60°$) and different values of ξ. The filled circles with error bars (1σ errors) denote the simulated data obtained with a 1 Ms observation of 1RXS J1708 by XIPE, assuming $\chi = 60°$ and $\xi = 30°$ (black lines). All quantities refer to the $2 - 6$ keV energy range (Taverna et al., 2014).

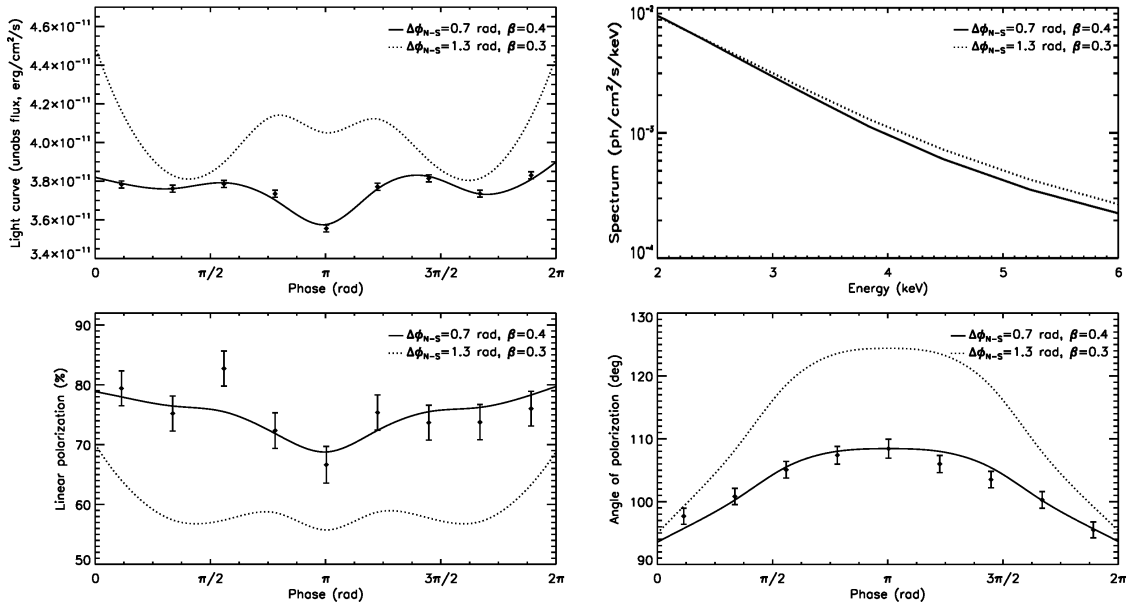

Figure 6.4: Comparison of the pulse profile (top-left panel), photon spectrum (top-right panel), phase-resolved polarization fraction (bottom-left panel) and angle (bottom-right panel) for two models, characterized by $\Delta\phi_{\rm N-S} = 0.7$ rad, $\beta_{\rm b} = 0.4$ (solid line, model A) and $\Delta\phi_{\rm N-S} = 1.3$ rad, $\beta_{\rm b} = 0.3$ (dotted line, model B). The filled circles with error bars denote the simulated XIPE data obtained from model A. All quantities refer to the 2-6 keV energy range (Taverna et al., 2014).

where γ is the rotational phase. From the plots in Figure 6.3 it is clear that a simultaneous fit of the polarization fraction and angle allows to derive unambiguously the value of ξ; additional information could be derived from the light curve that the instrument is able to provide thanks to its very good timing properties. A similar result holds by keeping constant the angle ξ and letting χ free to vary.

In the second simulation, illustrated in Figure 6.4, the issue of the spectral degeneracy, already mentioned in section 4.2, is addressed, considering two models characterized by a different set of parameters that produce an almost indistiguishable spectrum as shown in the top-right panel. Model A (solid line) has $\Delta\phi_{\rm N-S} = 0.7$ rad and $\beta_{\rm b} = 0.4$, while model B (dotted line) has $\Delta\phi_{\rm N-S} = 1.3$ rad and $\beta_{\rm b} = 0.3$; both models are for $\chi = 60°$ and $\xi = 30°$. The simulated XIPE data (filled circles with error bars) were generated from model A. This simulation highlights the merits of X-ray polarimetry: although also a precise fitting of the pulse profile alone allows to discriminate the two models (as already pointed out e.g. by Albano et al. (2010)), the addition of the two polarization observables can be crucial for assessing the consistency of the model and, if so, to enhance the significance of the measurement. In fact, a 1 Ms observation with XIPE clearly sets the two cases apart, both as far as the polarization degree and angle are concerned.

Simulation results shown in Figure 6.5 illustrate the capability of the method to recover the input model parameters from fitting the simulated data without any assumption, much in the same way as it would be done comparing the model with real

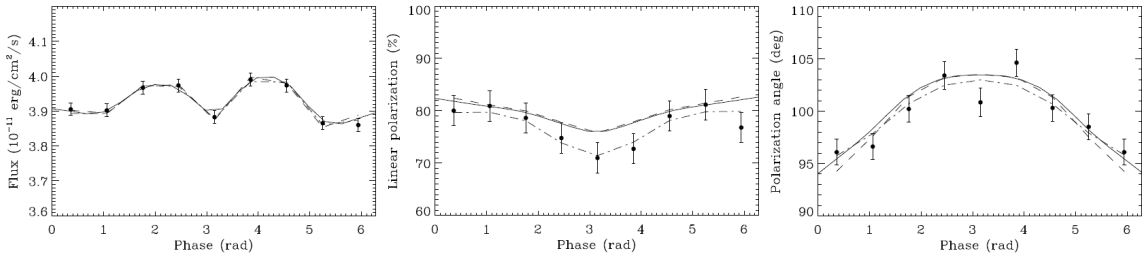

Figure 6.5: Simulated data (filled circles with error bars) and best simultaneous fit (solid line) of the pulse profile (left-hand panel), polarization degree (middle panel) and polarization angle (right-hand panel) in the $2-6$ keV energy range for the model characterized by the input parameters $\beta_{\rm b} = 0.34$, $\Delta\phi_{\rm N-S} = 0.5$ rad, $\chi = 60°$ and $\xi = 30°$. The dashed and dash-dotted lines show, respectively, the model from which simulated data were generated and the individual fits (Taverna et al., 2014).

observational data. To this end, an archive of theoretical simulations has been created, containing the pulse profile, phase-resolved polarization fraction and angle leaving both the magnetospheric parameters ($\beta_{\rm b}, \Delta\phi_{\rm N-S}$) and the geometrical angles (χ, ξ) free to vary; the magnetic field strength, the surface and electron temperature, together with the column density are, instead, held fixed at the values introduced previously. The parameter ranges covered are $0.2 \leq \beta_{\rm b} \leq 0.7$ (step 0.1), 0.3 rad $\leq \Delta\phi_{\rm N-S} \leq 1.4$ rad (step 0.1 rad), $15° \leq \chi \leq 150°$ (step 15°) and $15° \leq \xi \leq 90°$ (step 15°). Single models were then loaded in an IDL script which performs both individual and simultaneous fits of the "measured" pulsed profile, polarization fraction and polarization angle data, exploiting linear interpolation to obtain models for values of the parameters not included in the archive. The results of the fits shown in Figure 6.5 are summarized in Table 6.1. In particular the simultaneous fit of all the three observables is quite satisfactory ($\chi^2_{\rm red} = 0.97$), and returns parameter values which are well compatible with the input ones at the 2σ level. The only exception is the angle ξ, for which a value somewhat lower than the input one is derived.

	$\beta_{\rm b}$	$\Delta\phi_{\rm N-S}$ (rad)	χ (°)	ξ (°)	$\chi^2_{\rm red}$
Input values	0.34	0.5	60	30	-
1RXS J1708	0.34 ± 0.004	0.51 ± 0.01	61.4 ± 0.9	25.7 ± 1.8	0.97
Input values	0.5	1.3	90°	60°	-
Integration-on	0.501 ± 0.004	1.17 ± 0.03	90.3 ± 1.3	57.9 ± 2.2	1.17
Integration-off	0.503 ± 0.002	1.34 ± 0.04	89.3 ± 1.4	60.4 ± 3.2	7.78

Table 6.1: Best-fitting parameters (reported errors are at the 1σ level) (Taverna et al., 2014).

Finally, two further simulations, the results of which are shown in Figure 6.6, have been performed in order to better illustrate the dependence of the polarization signa-

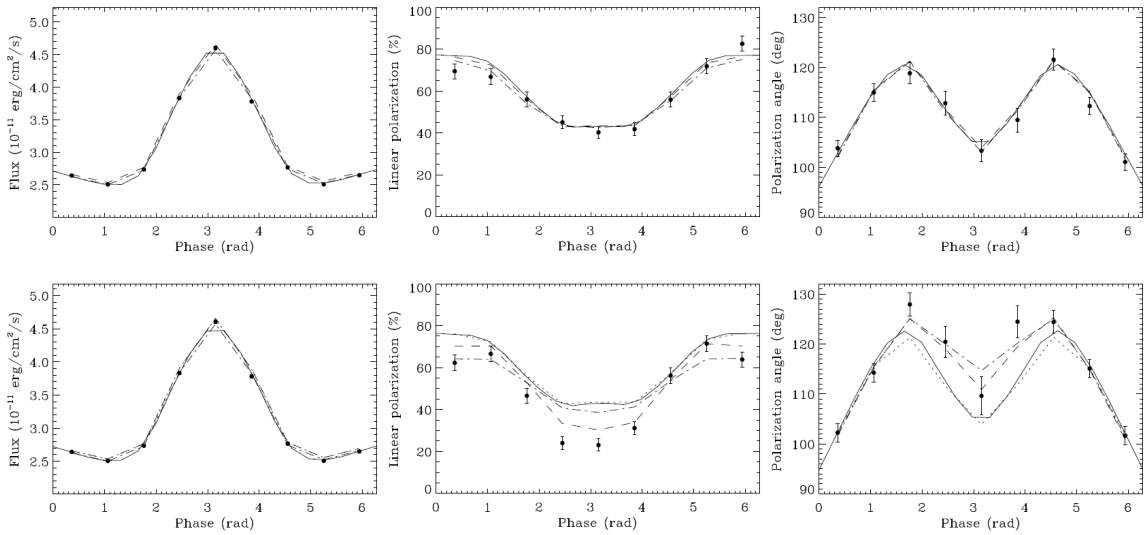

Figure 6.6: Comparison of the pulsed profile (left-hand column), polarization degree (middle column) and polarization angle (right-hand column), again in the $2-6$ keV energy range, for two models both characterized by $\Delta\phi_{\rm N-S} = 1.3$ rad, $\beta_{\rm b} = 0.5$, $\chi = 90°$ and $\xi = 60°$. The filled circles with error bars denote the XIPE data, generated with (top row) and without (bottom row) the integration of equations (2.38), as discussed in section 4.2. The solid and dash-dotted lines denote the simultaneous and individual fits, respectively, with "integration-on" models (see text for details). The dashed lines show the models from which data were produced; in the bottom panels the model obtained with the integration of equations (2.38) is also shown (dotted lines) for comparison (Taverna et al., 2014).

ture on vacuum polarization effects. Much at the same way as in the case illustrated in Figure 4.5, these two simulations have been generated from models with the same values of the input parameters ($\chi = 90°$, $\xi = 60°$, $\Delta\phi_{\rm N-S} = 1.3$ rad and $\beta_{\rm b} = 0.5$), the first ("integration-on") obtained integrating equations (2.38), as discussed in section 4.2, whereas in the second ("integration-off") the integration has not been performed, and the vacuum polarization effects have been accounted for with the simplified approach described in section 2.3.2. XIPE data have been generated for both the models, and fitted using the model archive discussed above, that includes the integration of equations (2.38). From the results shown in Figure 6.6, where the top panels refer to the integration-on case and the bottom panels to the integration-off one, it can be clearly seen that the polarization observable behaviors are quite different in the two cases, while the pulse profiles are indistinguishable, as expected. For the integration-on model, the simultaneous fit of the pulse profile, polarization fraction and angle is satisfactory ($\chi^2_{\rm red} \sim 1.2$) and returns values compatible, within errors, with the input ones (see Table 6.1). This, however, does not occur for the integration-off data, to which integration-on models provide an unacceptable representation ($\chi^2_{\rm red} \sim 7.8$). This show that polarimetric measurements are particularly sensitive to QED effects that act in the magnetosphere of highly magnetized NSs. Since, as pointed out in section 4.2, the main difference between the results of the two models is essentially given by the choice of the adiabatic boundary position, that in turn depends on the magnetic field strength, this means that polarimetry can be used to provide an indirect evidence of ultra-strong magnetic fields in these sources.

Chapter 7

Modeling of magnetar burst emission

Due to their strong magnetic fields, magnetars and XDINSs are in principle ideal candidates for polarization measurements, since the radiation emitted from their surface and reprocessed in their magnetosphere is expected to be characterized by a substantial polarization degree. Nevertheless the persistent emission of many of these sources (especially among XDINSs) is peaked at energies too low compared with the operational energy range of the instruments today under development[1]. On the other hand, the sources with hard enough emission are often characterized by small (unabsorbed) fluxes, so that the expected photon counts are extremely small, accounting for the standard exposure times that a typical mission can allocate for a single target. As a result, only a handful of these sources are indeed good candidates to be addressed by polarimetric investigations using the current technology. However, at least in the case of magnetars, short bursts and intermediate flares represent further possible targets for polarization measurements. In fact, they are much harder, and several orders of magnitude brighter, than the persistent emission (see §1.3.3); moreover, the occurrence of batches of these of events (during which a great number of single short bursts and intermediate flares are emitted) can compensate for their short duration time, providing enough statistics for a significant study. This is the case, for example, of the so-called "burst forest" (Israel et al., 2008), observed in 2006 March by SWIFT from the magnetar SGR 1900+14. In this chapter I discuss a simple approach for modeling the magnetar burst emission. I shortly describe the "trapped fireball" model (Thompson & Duncan, 1995, 2001, see also Yang & Zhang 2015), that is commonly believed to explain the spectral properties of the burst emission observed so far, comparing its theoretical implications with the observations discussed by Israel et al. (2008). Then, I present the code I developed to simulate the spectral and angular distributions of the burst radiation. Finally, I show the first, preliminary results which provide enough elements for a first comparison with the available observational data, although the work is still in progress.

[1]Due to the structure of the germanium detectors, on which photoelectric polarimeters are based, the minimum energy that can be reached by these instruments is ~ 2 keV.

7.1 Trapped fireball model

In the presence of the ultra-strong magnetic fields of magnetars, photons emitted in short bursts or intermediate flares can convert into electron-positron pairs. Due to Landau quantization (see §1.4.4), that prevents the transport of charged particles across the closed magnetic field lines, this pair plasma remains confined in the magnetosphere. In fact, the critical luminosity $L_{\rm crit}$ at which the radiation pressure breaks the magnetic confinment, given by the balance between the radiative energy density $L/4\pi r^2 c$ and the magnetic energy density $B^2/8\pi$, results

$$L_{\rm crit} \simeq 3 \times 10^{49} \left(\frac{B}{B_{\rm Q}}\right)^2 \left(\frac{r}{R_{\rm NS}}\right) \text{ erg s}^{-1} \,. \tag{7.1}$$

Since the typical luminosities of magnetar short bursts and intermediate flares are $\lesssim 10^{44}$ erg s^{-1} (see §1.3.3), this photon-pair plasma is indeed expected to be trapped, giving rise to a so-called "trapped fireball" (Thompson & Duncan, 1995, 2001). A simple sketch is shown in Figure 7.1, where, for the sake of simplicity, the magnetic field has been assumed as purely dipolar (Yang & Zhang, 2015). The trapped fireball is the orange region, enclosed between the star surface and a closed magnetic field line, the latter identified by its maximum radius $R_{\rm max}$. Owing to the fact that the optical depth deep in the fireball is expected to be very high, the equations that describe its structure can be solved in a geometrically-thin layer (the light-orange region in Figure 7.1), bounded by the closed field lines characterized by maximum radii $R_{\rm max,0}$ and $R_{\rm max}$, respectively, such that the optical depth is $\gg 1$ at the bottom interface and $\ll 1$ at the top.

Following the approach by Yang & Zhang (2015), the structure of this layer can be solved through a set of equations (the equation of state, the temperature gradient equation and the optical depth equation), similarly to the case of a magnetized atmosphere (see sections 1.5 and 5.1). The equation of state for the fireball medium, made by tightly coupled photons and electron-positron pairs, is determined by the total pressure P, the particle density ρ and the star magnetic field $\boldsymbol{B}$. Photons and pairs are characterized by the pressures $P_{\rm r}$ and $P_{\rm p}$, respectively, and, assuming pairs form an ideal gas in local thermodynamic equilibrium, they can be expressed as

$$P_{\rm r} = \frac{4\sigma_{\rm SB}}{3c} T^4 \qquad P_{\rm p} = \frac{\rho}{m_{\rm e}} k_{\rm B} T \,, \tag{7.2}$$

where $\sigma_{\rm SB}$ is the Stefan-Boltzmann constant. For mildly relativistic electrons and positrons (see §1.4), the pair plasma can be assumed to follow a one-dimensional, magnetized, non-relativistic distribution, characterized by a density (see Yang & Zhang, 2015)

$$\rho = m_{\rm e} \frac{(m_{\rm e}c)^3}{\hbar^3 (2\pi^3)^{1/2}} \frac{B}{B_{\rm Q}} \left(\frac{k_{\rm B}T}{m_{\rm e}c^2}\right)^{1/2} \exp\left(-\frac{m_{\rm e}c^2}{k_{\rm B}T}\right) . \tag{7.3}$$

The total pressure P is then obtained by adding to $P_{\rm r}$ and $P_{\rm p}$ the magnetic pressure $P_{\rm B} = B^2/8\pi$. In the hypothesis of hydrostatic equilibrium one has

$$\boldsymbol{\nabla} P + \rho \nabla \Phi - \frac{1}{4\pi} (\boldsymbol{B} \cdot \boldsymbol{\nabla}) B = 0 \,, \tag{7.4}$$

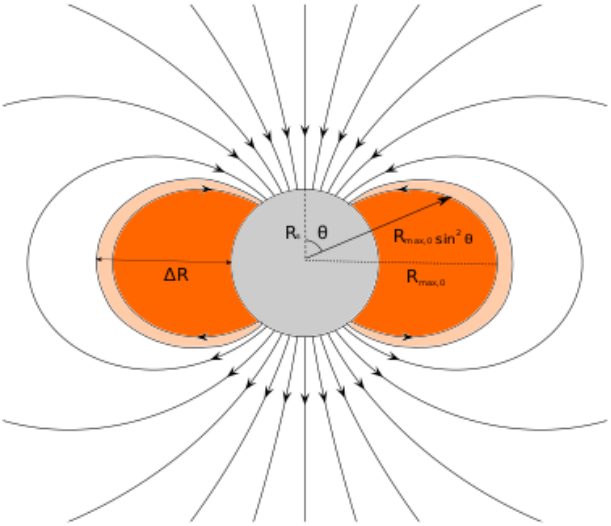

Figure 7.1: Simple illustration of the "trapped fireball". The orange region represents the entire fireball, enclosed between the star surface and a closed magnetic field line, characterized by a maximum radius $R_{\rm max}$: the linear size of the fireball is then quantified by the length $\Delta R = R_{\rm max} - R_{\rm NS}$. Due to the large optical depth expected in the fireball medium, the calculations can be restricted in the geometrically-thin, light-orange region between the closed field lines with maximum radii $R_{\rm max,0}$ and $R_{\rm max}$, respectively (Yang & Zhang, 2015, see text for details).

where Φ is the gravitational potential. Finally, taking the radial component of the previous equation, one has

$$\frac{{\rm d}P}{{\rm d}r} \simeq -\frac{GM_{\rm NS}\rho}{r^2}\left(1-\frac{R_{\rm s}}{r}\right)^{-1}\left[1+\frac{P+1.5P_{\rm p}+3P_{\rm r}+P_{\rm B}}{\rho c^2}\right]+F_{\rm B}\,, \tag{7.5}$$

with $R_{\rm s}$ the Schwarzschild radius and $F_{\rm B}$ the magnetic stress in the radial direction (i.e. the radial component of the last term in the left-hand side of equation 7.4).

Equation (7.4) is then supplemented by the temperature gradient equation

$$\frac{{\rm d}T}{{\rm d}r} = \frac{T}{P}\frac{{\rm d}P}{{\rm d}r}\frac{\ln T}{\ln P}\,, \tag{7.6}$$

where the ratio $\ln T/\ln P$ is determined by the energy transport equation[2]; and the optical depth equation

$$\frac{{\rm d}\tau}{{\rm d}r} = -\kappa_{\rm R}\rho\left(1-\frac{R_{\rm s}}{r}\right)^{-1/2}\,, \tag{7.7}$$

where $\kappa_{\rm R}$ is the Rosseland mean opacity (see below for further details).

The top panel of Figure 7.2 illustrates the behavior of the temperature in the outer layer of the fireball as a function of the radial distance from the bottom ($r - R_{\rm max,0}\sin^2\theta$), in the simplifying hypothesis that the energy transport inside this layer

[2]Since in strong magnetic fields convection is strongly suppressed (Rajagopal & Romani, 1996), only radiative transport needs to be considered.

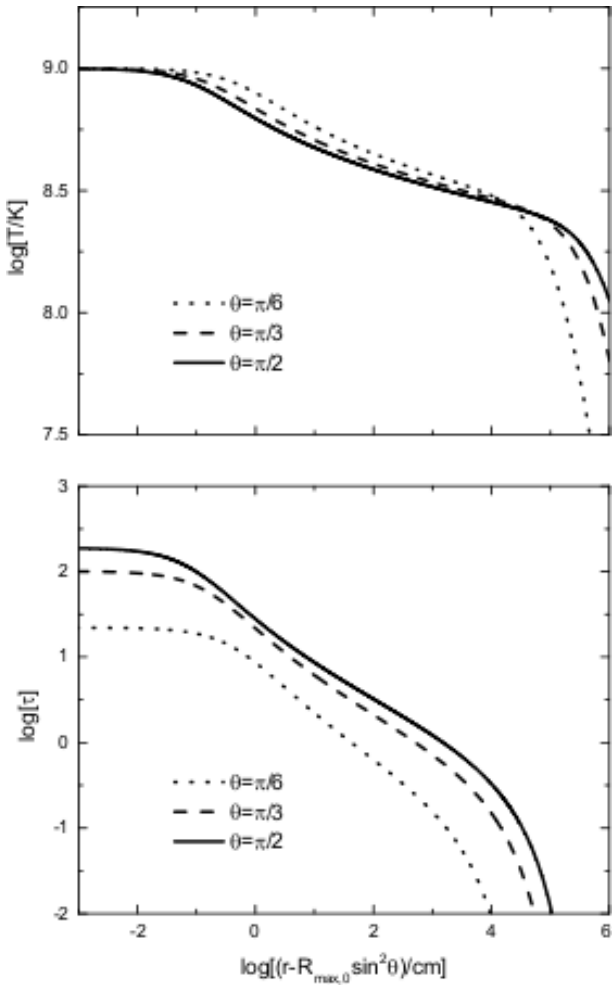

Figure 7.2: Temperature (top panel) and optical depth (bottom panel) plotted as functions of the radial distance from the bottom of the fireball outer layer, delimited by the closed field line with $R_{\rm max,0} = 2R_{\rm NS}$, for different values of the magnetic colatitude: $\theta = \pi/6$ (dotted lines), $\pi/3$ (dashed lines) and $\pi/2$ (solid lines). The magnetic field has been assumed as dipolar, with polar strength $B_{\rm pol} = 10^{15}$ G, while the maximum temperature (at the bottom of the layer) is $T_{\rm max} = 10^9$ K (Yang & Zhang, 2015).

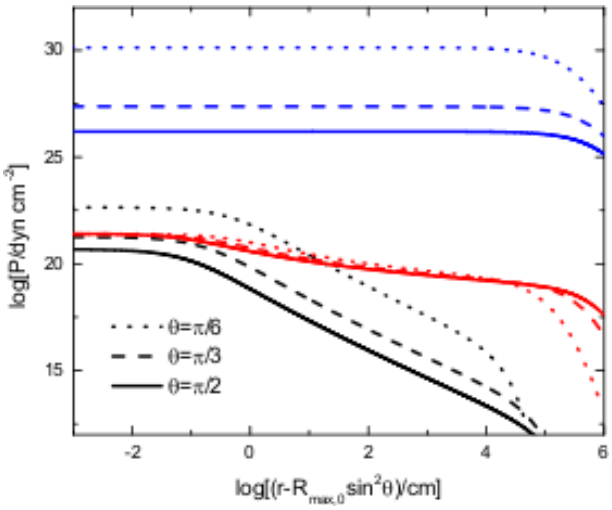

Figure 7.3: Magnetic (blue), radiation (red) and pair (black) pressures plotted as functions of the radial distance from the bottom of the fireball outer layer, for different values of the magnetic colatitude: $\theta = \pi/6$ (dotted lines), $\pi/3$ (dashed lines) and $\pi/2$ (solid lines). All the other parameters as in Figure 7.2 (Yang & Zhang, 2015).

is described in spherical symmetry (see Yang & Zhang, 2015, and references therein); the different curves correspond to different values of the magnetic colatitude θ (see Figure 7.1). The bottom panel shows, instead, the behavior of the optical depth in the same conditions. It can be seen, in particular, that the optical depth behavior is quite the same at all the magnetic colatitudes, approaching a value $\ll 1$ within $\sim 10^3$ cm. Also the temperature behavior is similar for different values of θ, slowly decreasing, up to $\sim 30\%$ of the value at the bottom of the layer ($T_{\rm max} = 10^9$ K), within 10^4 cm. The only exception is the case $\theta = \pi/6$ (near the magnetic pole), for which the temperature sensibly drops at distances $\gtrsim 10^5$ cm from the bottom.

Figure 7.3 illustrates the behavior of $P_{\rm p}$ (black), $P_{\rm r}$ (red) and $P_{\rm B}$ (blue), again as functions of the distance from the bottom of the layer and for different magnetic colatitudes. The fact that $P_{\rm B}$ is always greater than the pair and photon pressures confirms that the plasma is trapped in the magnetosphere, up to a distance of a few stellar radii from the star surface. On the other hand, the radiation pressure is normally higher than the pair one, except close to the northern magnetic pole (for $\theta = \pi/6$), where $P_{\rm p} > P_{\rm r}$ up to 10^2 cm, probably related to the temperature behavior for the same colatitude.

7.2 The SGR 1900+14 "burst forest"

In 2006 March, the SGR 1900+14, one of the three SGRs that exhibited a giant flare (see section 1.3.3), emitted a series of more than 40 bursts, seven of which classified as intermediate flares, observed by the SWIFT satellite within ~ 30 s (see Figure 1.4). This great number of events, the so-called "burst forest", provided enough statistics for the detailed study of burst/flare spectral properties, eventually confirming the pre-

dictions of the "trapped fireball" model. An accurate investigation was carried out by Israel et al. (2008), that tried to fit the observed spectra of such events in the $1-100$ keV energy range, using a set of single and multi-component models: optically-thin thermal bremsstrahlung (OTTB), power-law with an exponential cut-off (CutoffPL), disk blackbody (DiskBB) and different versions of comptonized spectra (CompST) among the former; double blackbody (BB+BB), OTTB plus a blackbody component at lower energies (OTTB+softBB) and a comptonization model with the addition of relativistic effects (CompTT) for the latter.

They found that no good results can be obtained by fitting the observed spectra with single component models; for example, in the case of the OTTB model the fit is good only restricting the entire energy range to $15-50$ keV, with a reduced chi-square $\chi^2_{\rm red} \approx 0.9$, while it clearly fails when the entire energy range is considered ($\chi^2_{\rm red} \approx 1.7$ in the range $E \sim 14-100$ keV). They verified that also the CutoffPL model, which could be considered as an extension of the simple OTTB, and the DiskBB one did not provide good fits. Albeit the addition of a BB component to the previous models seems to improve the fits, a satisfying level of accuracy could not be reached in any case. The best fitting model is BB+BB, with a value of $\chi^2_{\rm red}$ very close to unity[3]. In the case of the intermediate flares, for example, the two blackbody components are characterized by quite different values of average temperatures, $T_{\rm soft} = 4.8 \pm 0.3$ keV and $T_{\rm hard} = 9.0 \pm 0.3$ keV (errors at 1σ level), with corresponding average radiation radii $R_{\rm soft} = 30 \pm 2$ km and $R_{\rm hard} = 5.7 \pm 0.5$ km, respectively. The fact, in particular, that the radius inferred from softer component is a few times the stellar radius $R_{\rm NS}$ would confirm that the emission comes from an extended region in the magnetosphere, rather than from an hot spot on the surface.

Figure 7.4 shows the square of the radiation radius for the events observed by SWIFT during the entire 2006 March burst forest, plotted as a function of the corresponding blackbody temperature (see Israel et al., 2008). The red squares and green filled circles refer to the soft components, for luminosities respectively smaller and greater than 3×10^{40} erg s^{-1}, which is the threshold that separates the peaks from the inter burst/flare time intervals; the blue stars and the violet triangles refer instead to the hard components, still for luminosities below and above 3×10^{40} erg s^{-1}, respectively. The two populations of points corresponding to the softer and harder blackbodies are well separated, and both present a sort of cut-off, from which it is possible to estimate the typical size of the corresponding emitting regions: it results $R_{\rm BBs} \approx 30-200$ km for the soft components (with temperatures between 2 and 7 keV), while $R_{\rm BBh} \approx 3-30$ km for the harder ones (with $T_{\rm h} \sim 7-11$ km). This seems to suggest that photons come from two distinct regions, located in the surroundings of the star surface (higher in the magnetosphere) for more (less) energetic photons.

Points corresponding to $L < 3 \times 10^{40}$ erg s^{-1} in Figure 7.8 show a certain correlation between the square of the radiation radius and the temperature, following a power law $R^2 \propto T^{-3}$. This is different from what one would expect from blackbody components, i.e. $R^2 \propto T^{-4}$, for events with the same luminosity. The less steep behavior observed by SWIFT suggests that a constant number of photons is emitted per unit time. A

[3]According to the results of Israel et al. (2008), also the CompTT model can fit well the observed spectra, with $\chi_{\rm red} \simeq 0.99$.

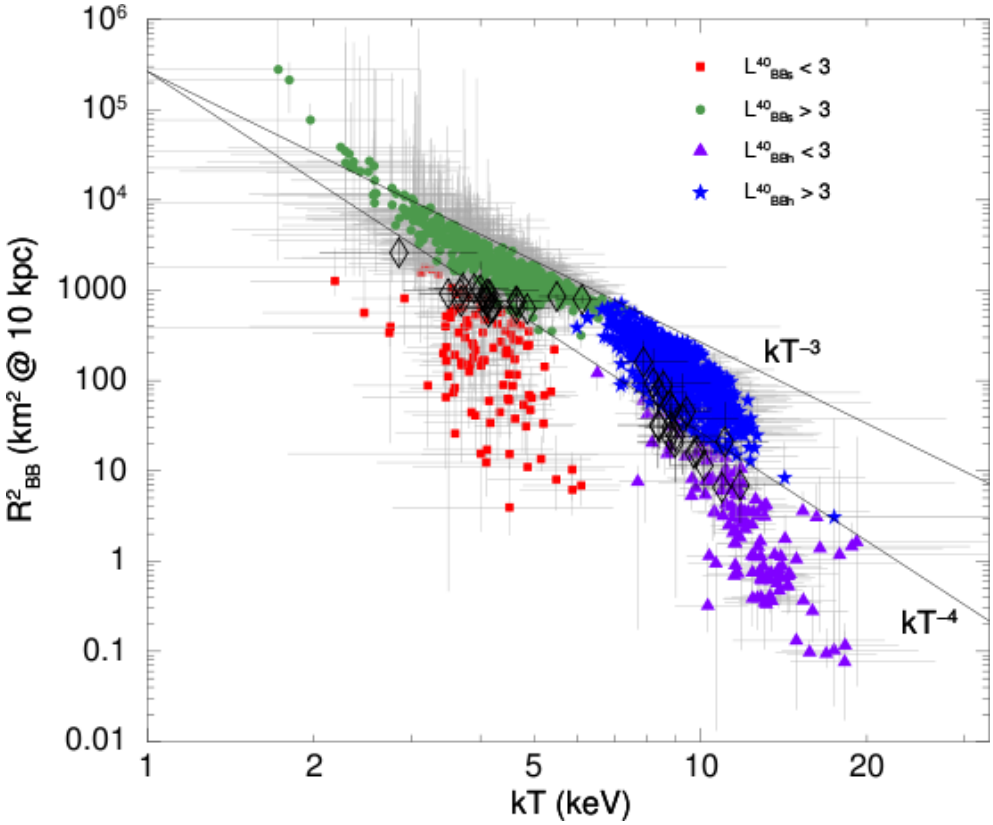

Figure 7.4: Square of the radiation radius as a function of the blackbody temperature for the events collected by SWIFT in 2006 March from SGR 1900+14 (a distance of 10 kpc is assumed). The red squares and green filled circles refer to the soft components, with luminosity lower and higher than 3×10^{40} erg s^{-1}, respectively; the same for the blue stars and the violet triangles, referring to the hard components. The black diamonds mark the measurements performed by HETE-2 (Olive et al., 2004) for the intermediate flares emitted by SGR 1900+14 in 2001. The power laws $R^2 \propto T^{-3}$ and $R^2 \propto T^{-4}$ are also shown (black solid lines) (Israel et al., 2008).

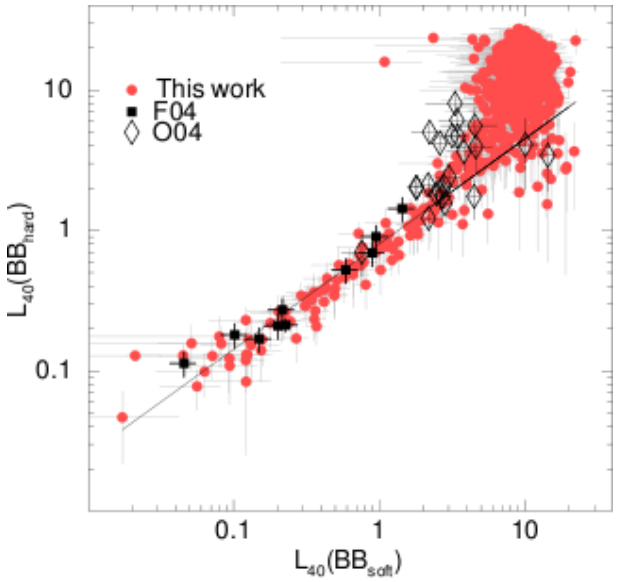

Figure 7.5: Time-resolved bolometric luminosities (in units of 10^{40} erg s^{-1}) of the harder blackbody components that fit the spectra of the events observed by SWIFT in 2006 March (red filled circles), plotted as functions of the luminosities of the softer components. The black diamond refer to the intermediate flares observed by HETE-2 in 2001 (Olive et al., 2004), while the black squares refer to the measurements performed by Feroci et al. (2004). The power law $L_{\rm soft} \propto (L_{\rm hard})^{\alpha}$, with $\alpha = 0.7 \pm 0.03$ (at 1σ level) is also shown (Israel et al., 2008).

strong correlation is also visible in Figure 7.5, where the (bolometric) luminosity of the hard blackbody components is plotted as a function of that of the softer ones. The correlation appears when both the luminosities are below $\sim 3 \times 10^{40}$ erg s^{-1}, with the points (the red filled circles correspond to the SWIFT measurements, see Israel et al., 2008) that follow a power-law distribution with photon index ~ 0.7. Moreover, also points corresponding to events detected by other instruments from the same source (see Olive et al., 2004; Feroci et al., 2004) are arranged along the same line. For higher luminosities, instead, the softer components saturate at a value around $7-14\times10^{40}$ erg s^{-1}, while the harder ones continue to increase up to a value $\sim 3 \times 10^{41}$ erg s^{-1}. This behavior suggests the occurrence of a saturation effect: in fact, for a magnetic field strength $B \simeq 8 \times 10^{14}$ G (that is the value inferred from the spin-down rate of SGR 1900+14) the maximum value attained by the harder component luminosity matches well the magnetic Eddington limit

$$L_{\rm Edd,B} \approx 2 \times 10^{40} \left(\frac{B}{B_{\rm Q}}\right)^{4/3} \left(\frac{r}{R_{\rm NS}}\right)^{2/3} \text{erg s}^{-1} \,. \tag{7.8}$$

This is in agreement with the statement by Thompson & Duncan (1995), according to which the luminosity emitted by a fireball trapped in the magnetosphere of a magnetar never exceeds the magnetic Eddington luminosity.

The origin of the two components in the spectra of magnetar bursts and intermediate flares has been explained by Israel et al. (2008) with the different ways ordinary and extraordinary photons propagate in the fireball medium. In fact, as photons pass through the fireball, they undergo (non resonant) magnetic Compton scattering with the electrons and positrons of the medium. The differential cross sections of this process, expressed in the particle rest frame, are given by (Harding & Daugherty, 1991, see also Herold 1979)

$$\left[\frac{\mathrm{d}^2\sigma}{\mathrm{d}\Omega'\mathrm{d}\varepsilon'}\right]_{\rm i-j} = \Sigma_{\rm i-j}\delta(\varepsilon'-\varepsilon)\,, \tag{7.9}$$

where $i, j = \mathrm{O}, \mathrm{X}$ are the polarization states of the incoming and outcoming photons, respectively, and

$$\begin{aligned}
\Sigma_{\rm O-O} &= \frac{3}{8\pi}\sigma_{\rm T}\sin^2\theta_{\rm Bk}\sin^2\theta'_{\rm Bk} \\
\Sigma_{\rm X-O} &= \frac{3}{8\pi}\sigma_{\rm T}\left(\frac{\varepsilon B_{\rm Q}}{B}\right)^2\cos^2\theta'_{\rm Bk}\cos^2\left(\phi_{\rm Bk}-\phi'_{\rm Bk}\right) \\
\Sigma_{\rm O-X} &= \frac{3}{8\pi}\sigma_{\rm T}\left(\frac{\varepsilon B_{\rm Q}}{B}\right)^2\cos^2\theta_{\rm Bk}\cos^2\left(\phi_{\rm Bk}-\phi'_{\rm Bk}\right) \\
\Sigma_{\rm X-X} &= \frac{3}{8\pi}\sigma_{\rm T}\left(\frac{\varepsilon B_{\rm Q}}{B}\right)^2\sin^2\left(\phi_{\rm Bk}-\phi'_{\rm Bk}\right)\,;
\end{aligned} \tag{7.10}$$

$\sigma_{\rm T}$ is the Thompson cross section, ε (ε') is the incoming (outcoming) photon energy in units of $m_{\rm e}c^2$ and $\theta_{\rm Bk}, \phi_{\rm Bk}$ ($\theta'_{\rm Bk}, \phi'_{\rm Bk}$) fix the propagation direction of the incoming (outcoming) photon with respect to the magnetic field $\boldsymbol{B}$, $\mathrm{d}\Omega' = \mathrm{d}\cos\theta'_{\rm Bk}\mathrm{d}\phi'_{\rm Bk}$. Equations

(7.10) show that the scattering cross section is different depending on the polarization mode of the incoming photons: in particular, a photon can change its original polarization mode upon scatterings. Moreover, all the cross sections that involve extraordinary photons are suppressed by a factor $(B/B_{\rm Q})^{-2}$; this means that the X-mode opacity inside the fireball is much reduced with respect to the O-mode one, due to the strong magnetic field of the star.

As a consequence, the photosphere of the extraordinary photons (i.e. the region were the optical depth $\tau_{\rm X} \sim 1$) will be located closer to the star surface than that of the ordinary ones, as it happens for the emitting regions of the harder and softer components of short bursts and intermediate flares spectra (see Figure 7.8). According to this scenario, Israel et al. (2008) proposed that the two thermal components are indeed generated from the X-mode and O-mode photon photospheres.

7.3 Numerical code and preliminary results

In order to simulate the spectra emitted in the typical magnetar short bursts or intermediate flares, I developed a FORTRAN code, based on the propagation of ordinary and extraordinary photons through the medium of a fireball trapped in the magnetosphere. Following the approach proposed by Yang & Zhang (2015), the code solves the radiative transfer equation in a geometrically thin layer, made by non-relativistic electrons and positrons. This slab is divided in a number of different patches, labelled by the angle $\theta_{\rm B}$ that the magnetic field direction at the patch centre makes with the slab normal; the spectral and polarization properties of the radiation coming from the entire slab will be reconstruct by summing the contributions of the different patches. However, as the code is still at a preliminary stage of development, I discuss in the following the results that can be obtained considering only one patch of the fireball slab (choosing as an input the value of $\theta_{\rm B}$).

7.3.1 Approximations

In the code a series of simplifying approximations have been assumed. First of all, the slab medium has been considered as plane-parallel (i.e. all the relevant quantities for the solution of the radiative transfer equation depend only on the height z with respect to the bottom of the slab); this is a good approximation only if the depth scale-height of the slab is much smaller than its extension, that is precisely the hypothesis of Yang & Zhang (2015).

The slab medium has been taken as a pure-scattering medium: this means that true absorption and emission have not been considered. Also processes which do not preserve the number of photons, as for example photon splitting or double-Compton scattering, have been neglected. These are, in fact, second-order processes, the contributions of which become important only at high energies (above 100 keV). However, all the calculations presented in the following are restricted in the $1 - 100$ keV energy range and the maximum temperature deviation from the maximum value at the bottom of the slab is $\sim 20\%$ (see below). Hence, since Compton scattering is the only radiative process taken into account, the total number of photons should be preserved

in all the simulations.

A more complete way to deal with the problem of radiative transfer in a magnetar trapped fireball should include magnetohydrodynamic equations, in order to understand how the electron-positron plasma and photons exchange energy. This, however, could be quite complicate, also in the light of the high computing times required for each simulation and the convergence problems, discussed in section 7.3.3. For all these reasons, the energy exchanges between the fireball charged particles and photons at this stage have been completely neglected.

7.3.2 Numerical integration

While scattering, as described by the cross sections (7.9), is conservative in the particle rest frame (i.e. the energy of the outcoming photon is the same as that of the incoming one), in the stellar frame scattering could be conservative or not. The code can indeed solve the radiative transfer equation in the fireball in both the limits of conservative and non-conservative scattering.

In the general case of electrons/positrons moving at speed β (in units of the speed of light c) with respect to the star, the expressions for the scattering cross sections in the stellar reference frame can be obtained from those in the particle rest frame (equations 7.10) through

$$\sigma_{\mathrm{i-j}}^{\mathrm{star}} = \frac{D}{D'}\sigma_{\mathrm{i-j}}\,, \tag{7.11}$$

where

$$D = 1 - \beta\mu_{\mathrm{Bk}} \qquad D' = 1 - \beta\mu'_{\mathrm{Bk}} \tag{7.12}$$

and μ_{Bk} (μ'_{Bk}) is the cosine of the angle between the incoming (outcoming) photon direction $\boldsymbol{k}$ and the magnetic field direction $\boldsymbol{B}$ in the star frame (Pomraning, 1973). In particular, using the angular aberration formula, one obtains

$$\begin{aligned} \cos\theta_{\mathrm{Bk}} &= \frac{\mu_{\mathrm{Bk}} - \beta}{D} \qquad \sin\theta_{\mathrm{Bk}} = \frac{\sqrt{1-\mu_{\mathrm{Bk}}^2}}{\gamma D} \\ \cos\theta'_{\mathrm{Bk}} &= \frac{\mu'_{\mathrm{Bk}} - \beta}{D'} \qquad \sin\theta'_{\mathrm{Bk}} = \frac{\sqrt{1-\mu'^2_{\mathrm{Bk}}}}{\gamma D'}\,, \end{aligned} \tag{7.13}$$

while, for the energy, it holds

$$\varepsilon = \gamma D\epsilon \qquad \varepsilon' = \gamma D'\epsilon'\,, \tag{7.14}$$

with ϵ (ϵ') the incoming (outcoming) photon energy in the stellar frame (in units of $m_{\mathrm{e}}c^2$) and γ the particle Lorentz factor.

Putting all together in equation (7.11) and integrating over the velocities of the scattering particles, one can obtain the Compton scattering kernel for the process in the stellar frame, that results

$$\sigma_{\mathrm{i-j}}^{\mathrm{star}}(\epsilon \to \epsilon', \Omega \to \Omega') = \int \mathrm{d}\beta f(\beta)\Sigma_{\mathrm{i-j}}\frac{n_{\mathrm{e}}}{\gamma}\frac{D}{D'}\delta(\gamma D'\epsilon' - \gamma D\epsilon)\,, \tag{7.15}$$

where $n_{\rm e}$ is the particle density and $f(\beta)$ is the one-dimensional particle velocity distribution,

$$f(\beta)\mathrm{d}\beta = \frac{\gamma^3 \mathrm{e}^{-(\gamma-1)/\Theta}\mathrm{d}\beta}{2\,\mathrm{e}^{1/\Theta}K_1(1/\Theta)}\,, \tag{7.16}$$

with $\Theta = kT/m_{\rm e}c^2$ and K_1 the modified Bessel function of the first kind[4]. Using equations (7.12), (7.14) and the properties of the Dirac-δ, equation (7.15) can be simplified in

$$\sigma^{\rm star}_{\rm i-j}(\epsilon \to \epsilon', \Omega \to \Omega') = n_{\rm e} x \frac{\Sigma_{\rm i-j}(\beta_0) f(\beta_0)}{\gamma_0^2\,|\mu_{\rm Bk}\epsilon - \mu'_{\rm Bk}\epsilon'|}\,, \tag{7.17}$$

where $x = \epsilon'/\epsilon$ and

$$\beta_0 = \frac{x-1}{\mu'_{\rm Bk}x - \mu_{\rm Bk}}\,. \tag{7.18}$$

Finally, using equations (7.10) and (7.13), and normalizing to $\sigma_{\rm T}$, one has

$$\begin{aligned}
\sigma_{\rm O-O}(\alpha \to \alpha') &= \frac{n_{\rm e}|\beta|\mathrm{e}^{-(\gamma-1)/\Theta}}{2\,\mathrm{e}^{1/\Theta}K_1(1/\Theta)} \frac{x(1-\mu_{\rm Bk}^2)}{\epsilon|x-1|} \frac{(1-\mu'^2_{\rm Bk})}{\gamma^3(1-\beta\mu_{\rm Bk})^2(1-\beta\mu'_{\rm Bk})^2} \\
\sigma_{\rm O-X}(\alpha \to \alpha') &= \frac{n_{\rm e}|\beta|\mathrm{e}^{-(\gamma-1)/\Theta}}{2\,\mathrm{e}^{1/\Theta}K_1(1/\Theta)} \frac{x(\mu_{\rm Bk}-\beta)^2}{\epsilon|x-1|} \left(\frac{\epsilon B_{\rm Q}}{B}\right)^2 \gamma^3 \cos^2\left(\phi_{\rm Bk} - \phi'_{\rm Bk}\right) \\
\sigma_{\rm X-O}(\alpha \to \alpha') &= \frac{n_{\rm e}|\beta|\mathrm{e}^{-(\gamma-1)/\Theta}}{2\,\mathrm{e}^{1/\Theta}K_1(1/\Theta)} \frac{x^3(\mu'_{\rm Bk}-\beta)^2}{\epsilon|x-1|} \left(\frac{\epsilon B_{\rm Q}}{B}\right)^2 \gamma^3 \cos^2\left(\phi_{\rm Bk} - \phi'_{\rm Bk}\right) \\
\sigma_{\rm X-X}(\alpha \to \alpha') &= \frac{n_{\rm e}|\beta|\mathrm{e}^{-(\gamma-1)/\Theta}}{2\,\mathrm{e}^{1/\Theta}K_1(1/\Theta)} \frac{x(1-\beta\mu_{\rm Bk})^2}{\epsilon|x-1|} \left(\frac{\epsilon B_{\rm Q}}{B}\right)^2 \gamma^3 \sin^2\left(\phi_{\rm Bk} - \phi'_{\rm Bk}\right)\,,
\end{aligned} \tag{7.19}$$

where the symbols α and α' label the pairs ϵ, Ω and ϵ', Ω', respectively. For the Compton scattering kernels obtained above, the detailed balance condition for a one-dimensional electron thermal distribution leads to (Mèszàros et al., 1989; Alexander et al., 1989)

$$\sigma_{\rm i-j}(\alpha' \to \alpha) = \left(\frac{\epsilon}{\epsilon'}\right)^2 \mathrm{e}^{(\epsilon'-\epsilon)/\Theta}\sigma_{\rm i-j}(\alpha \to \alpha')\,. \tag{7.20}$$

Before to enter in the main code, a specific routine integrates, over the outcoming photon energy and solid angle, equations (7.9) in the conservative case, and (7.19) in the non-conservative one, in order to have the total cross sections of the process. As an example, Figure 7.6 shows the behavior of the (normalized) cross sections (7.19), integrated over the solid angle Ω', as functions of the ratio $x = \epsilon'/\epsilon$, for different values of $\mu_{\rm Bk}$.

Actually, as it can be seen from equations (7.10) and (7.19), the cross sections depend on the polar angles that the photon propagation direction $\boldsymbol{k}$ makes with the magnetic field direction $\boldsymbol{B}$. Nevertheless the radiative transfer problem in a plane-parallel medium can be simplified considering the evolution of the photon intensity

[4]Although the distribution function (7.16) allows for the calculation in the case of relativistic particles, in the code the cross sections are derived in the non-relativistic limit, i.e. for $\beta \ll 1$ and $\gamma \simeq 1$.

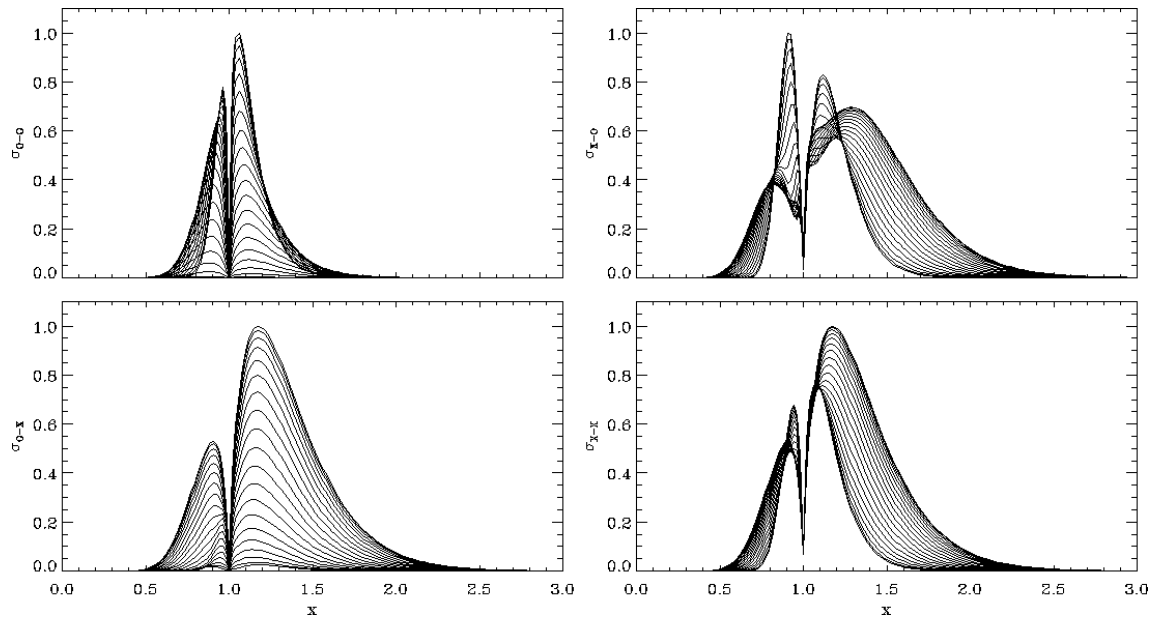

Figure 7.6: Normalized cross sections for the non-resonant, magnetic Compton scattering, integrated over the solid angle Ω' of the outcoming photons, plotted as functions of the ratio $x = \epsilon'/\epsilon$ of the outcoming and incoming photon energies. The different lines refer to different values of $\mu_{\rm Bk}$.

along the direction $\boldsymbol{z}$ of the patch normal, with respect to which $\boldsymbol{k}$ is identified by the polar angles $\theta_{\rm z}$ and $\phi_{\rm z}$. According to the geometry shown in Figure 7.7, one has

$$\begin{aligned} \mu_{\rm z} &= \mu_{\rm Bk}\mu_{\rm B} - \sqrt{1-\mu_{\rm Bk}^2}\sqrt{1-\mu_{\rm B}^2}\cos\phi_{\rm Bk} \\ \cos\phi_{\rm z} &= \frac{\mu_{\rm z}\mu_{\rm B} - \mu_{\rm Bk}}{\sqrt{1-\mu_{\rm z}^2}\sqrt{1-\mu_{\rm B}^2}}\,. \end{aligned} \tag{7.21}$$

In the assumptions discussed above, the radiative transfer equation takes the form

$$\mu_{\rm z}\frac{{\rm d}n^{\rm (O,X)}}{{\rm d}\bar{\tau}} = \left[\epsilon^2 + n^{\rm (O,X)}(\epsilon,\mu_{\rm Bk})\right]\int {\rm e}^{(\epsilon-\epsilon')/\Theta}H_{1,2}(\epsilon'){\rm d}\epsilon' - n^{\rm (O,X)}\int G_{1,2}(\epsilon'){\rm d}\epsilon'\,, \tag{7.22}$$

where stimulated scattering has been taken into account, $n^{\rm (O,X)} = \epsilon^2 f^{\rm (O,X)}$ is the O,X-mode number intensity ($f^{\rm (O,X)}$ is the corresponding occupation number) and all the angles and energies are expressed in the stellar frame. The height $\bar{\tau}$ (${\rm d}\bar{\tau} = n_{\rm e}\sigma_{\rm T}{\rm d}z$) is related to the optical depth τ of the slab: while the optical depth is maximum ($\tau = \tau_{\rm max}$) at the bottom of the slab and zero at the top, $\bar{\tau}$ is defined in such a way that $\bar{\tau} = 0$ at the bottom and $\bar{\tau} = \tau_{\rm max}$ at the top of the slab. $H_{1,2}$ and $G_{1,2}$ are the source functions, that contain the integrals of the cross sections over the angles of the

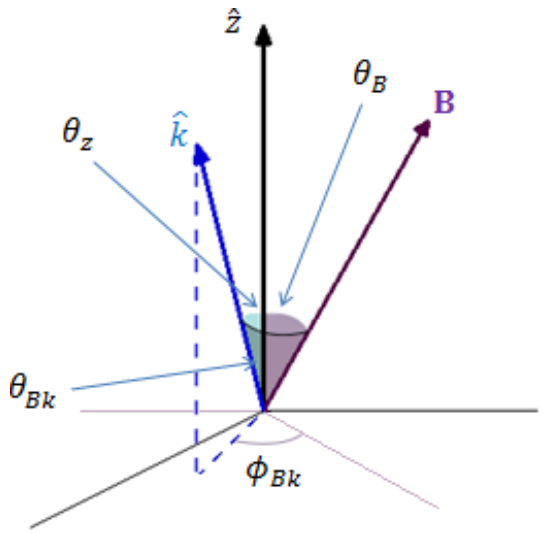

Figure 7.7: Geometry used in the code for the solution of the radiative transfer equation in a patch of the plane-parallel slab, characterized by the angle $\theta_{\rm B}$ between the patch normal $\boldsymbol{z}$ and the magnetic field direction $\boldsymbol{B}$ at the patch centre. The angle $\theta_{\rm z}$, $\theta_{\rm Bk}$ and $\phi_{\rm Bk}$ are also shown (see text for further details).

outcoming photons, referred to the patch normal $\boldsymbol{z}$; in particular

$$\begin{aligned} H_1(\epsilon') &= \int \left[\sigma_{\rm O-O} n^{(\rm O)} + \sigma_{\rm O-X} n^{(\rm X)}\right] {\rm d}\mu'_{\rm z} {\rm d}\phi'_{\rm z} \\ H_2(\epsilon') &= \int \left[\sigma_{\rm X-X} n^{(\rm X)} + \sigma_{\rm X-O} n^{(\rm O)}\right] {\rm d}\mu'_{\rm z} {\rm d}\phi'_{\rm z} \\ G_1(\epsilon') &= H_1(\epsilon') + \sigma_1(\epsilon') \\ G_2(\epsilon') &= H_2(\epsilon') + \sigma_2(\epsilon') \,, \end{aligned} \tag{7.23}$$

where

$$\sigma_1(\epsilon') = \int \left[\sigma_{\rm O-O} + \sigma_{\rm O-X}\right] {\rm d}\mu'_{\rm z} {\rm d}\phi'_{\rm z} \qquad \sigma_2(\epsilon') = \int \left[\sigma_{\rm X-X} + \sigma_{\rm X-O}\right] {\rm d}\mu'_{\rm z} {\rm d}\phi'_{\rm z} \,. \tag{7.24}$$

The code integrates numerically equation (7.22) using the $\Lambda-$iteration method, that is the most common way to solve the radiative transfer equation. Writing the radiative transfer equation in its general form,

$$\frac{{\rm d}I_\nu}{{\rm d}\tau} = I_\nu - S_\nu \,, \tag{7.25}$$

with I_ν the specific (monochromatic) intensity and S_ν the source function (given by the ratio between the emission and absorption coefficients of the medium), and solving for I_ν, one can define the operator $\boldsymbol{\Lambda}$ as

$$I_\nu = \int_0^{\tau_{\rm max}} {\rm e}^{-\tau} S_\nu(\tau) {\rm d}\tau \equiv \boldsymbol{\Lambda}_{\Omega,\nu} \left[S_\nu(\boldsymbol{x})\right] \,. \tag{7.26}$$

The code starts with an initial guess for the source function, S_ν^0; the successive iterations give

$$S_\nu^{n+1} = \mathbf{\Lambda}[S_\nu^n]\,, \tag{7.27}$$

until the condition $S_\nu^{n+1} \simeq S_\nu^n$ at the desired degree of accuracy is reached. In each iteration, the integration is performed using a Runge-Kutta, fourth order method, choosing, as boundary conditions, a blackbody distribution for both the ordinary and the extraordinary photons at the bottom of the slab, and no incoming flux at the top of the slab, i.e. $n^{(\mathrm{O,X})} = 0$ for $-1 \leq \mu_\mathrm{z} \leq 0$ (Sommerfield radiation condition).

The outputs of each run are the arrays of the intensities $n^{(\mathrm{O,X})}$, as functions of the height $\bar{\tau}$ in the slab, the photon energy ϵ and the polar angles θ_Bk and ϕ_Bk that the photon direction $\boldsymbol{k}$ makes with the magnetic field direction. It is also possible to resume the integration using as starting point the outputs of the code after a certain number of iterations; in this way one can suitably control when convergence has been reached.

7.3.3 Preliminary results and open problems

As mentioned before, the following results refer to only one patch of the fireball slab, characterized by an angle $\theta_\mathrm{B} = 45°$ between the magnetic field direction and the patch normal (see Figure 7.7). Unless explicitly stated otherwise, it has been taken $\bar{\tau}_\mathrm{max} = 100$ and the temperature of the initial blackbodies at the bottom of the slab is set at $T_\mathrm{max} =$ 10 keV. Since a too large temperature gradient may result in numerical instabilities, the code has been tested (at a preliminary stage) using a mild temperature gradient:

$$T(\bar{\tau}) = T_\mathrm{max}\left[1 - 0.2\left(\frac{\bar{\tau}}{\bar{\tau}_\mathrm{max}}\right)\right]\,; \tag{7.28}$$

in this way, the temperature T_ext at the top of the slab is only 20% smaller than that at the bottom. The code outputs are loaded into an IDL script, in order to obtain the plots of the (number) total flux and spectrum for both the ordinary and the extraordinary photons, as well as the angular distributions for the photon intensities $n^{(\mathrm{O})}$ and $n^{(\mathrm{X})}$.

Figure 7.8 shows the frequency-integrated number flux plotted as a function of the height $\bar{\tau}$ in the conservative (left-hand column) and non-conservative (right-hand column) cases, after 100 iterations. The top row illustrates the behavior of the total flux (black), outward flux (red) and inward flux (blue), obtained by summing the contributions of both the ordinary and the extraordinary photons; in the bottom row, instead, the outward (red) and inward (blue) fluxes are drawn individually for O-mode (solid lines) and X-mode (dashed lines) photons. Since, as said in section 7.3.1, (magnetic) Compton scattering conserves the total photon number, the total flux (black line in the top panels) is expected to be constant in $\bar{\tau}$. This seems to be the case for the conservative scattering, for which, after 100 iterations, the total flux is nearly constant, a part from a little deviation that reaches its maximum value ($\sim 5\%$) at $\bar{\tau} \simeq 50$. In the case of non-conservative scattering, instead, the total flux tends to increase with $\bar{\tau}$; moreover, I found that the deviation gets worse as the iteration number increases, implying a convergence problem. Looking at the plots of the bottom-right panel, it can be seen that the increase of the total flux can be associated to a flattening of

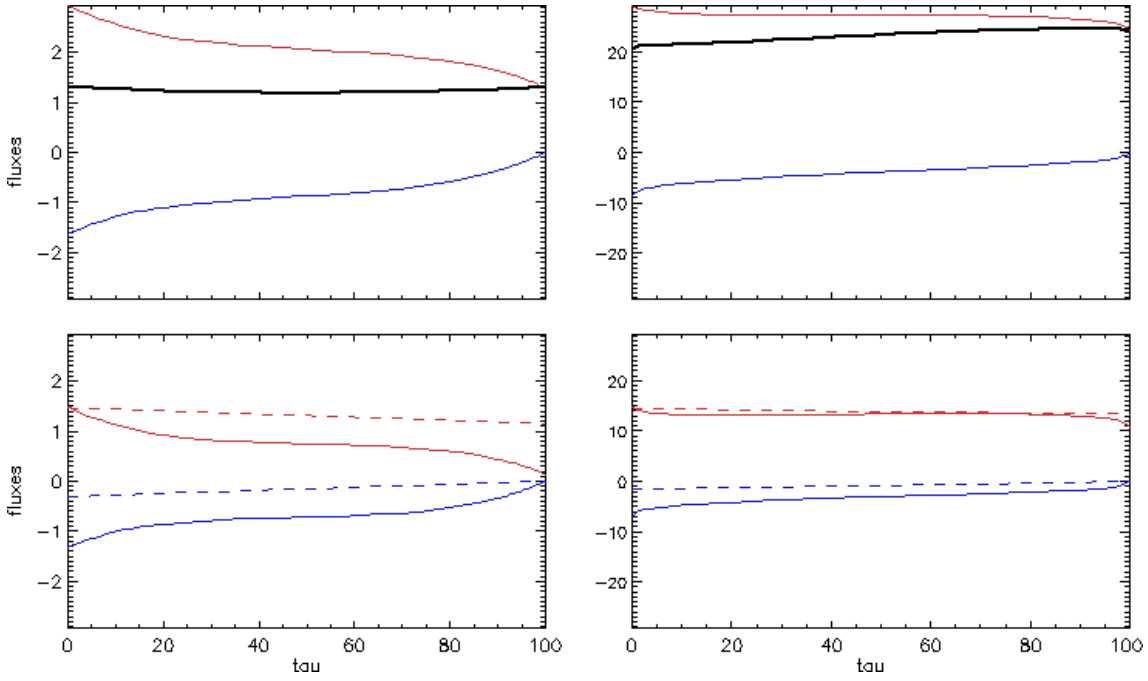

Figure 7.8: Number fluxes (in arbitrary units) as functions of $\bar{\tau}$ in the conservative (left-hand column) and non-conservative (right-hand column) cases after 100 iterations. Top row: total flux (black), outward flux (red) and inward flux (blue) obtained by summing the contributions of both the ordinary and the extraordinary photons. Bottom row: outward fluxes (red) and inward fluxes (blue) for ordinary (solid lines) and extraordinary (dashed lines) photons singularly.

the ordinary photon outward flux (red-solid line), contrary of what happens in the conservative case, where the ordinary outward flux decreases monotonically with $\bar{\tau}$.

Figure 7.9 shows the emerging (number) spectra (n, in arbitrary units, as a function of ϵ for $\bar{\tau} = 100$) in the case of ordinary photons (top row), extraordinary photons (middle row) and the total spectrum (bottom row), for both the conservative (left-hand column) and non-conservative (right-hand column) cases, obtained after 100 iterations. The blackbody at the external temperature ($T_{\rm ext} = 8$ keV, according to equation 7.28) is also shown (dashed/dotted lines) in all the panels. While in the conservative case the emerging spectrum of the ordinary photons is well below the blackbody at the external temperature, for non-conservative scattering it is much harder, and approaches the blackbody at $T_{\rm ext}$ as the number of iterations increases. On the contrary, the extraordinary photon spectra are quite similar in the two limits, and it can be checked that the spectral shape remains substantially unchanged also increasing the iteration number. Consequently, the total emerging spectrum results very similar to that of the extraordinary photon in the conservative limit, while it is partially influenced by the addition of the ordinary photon contribution (especially at high energies) in the non-conservative case.

What Figures 7.8 and 7.9 show, for the case of conservative scattering, indeed reflects what one can expect looking at the expressions of the scattering cross sections

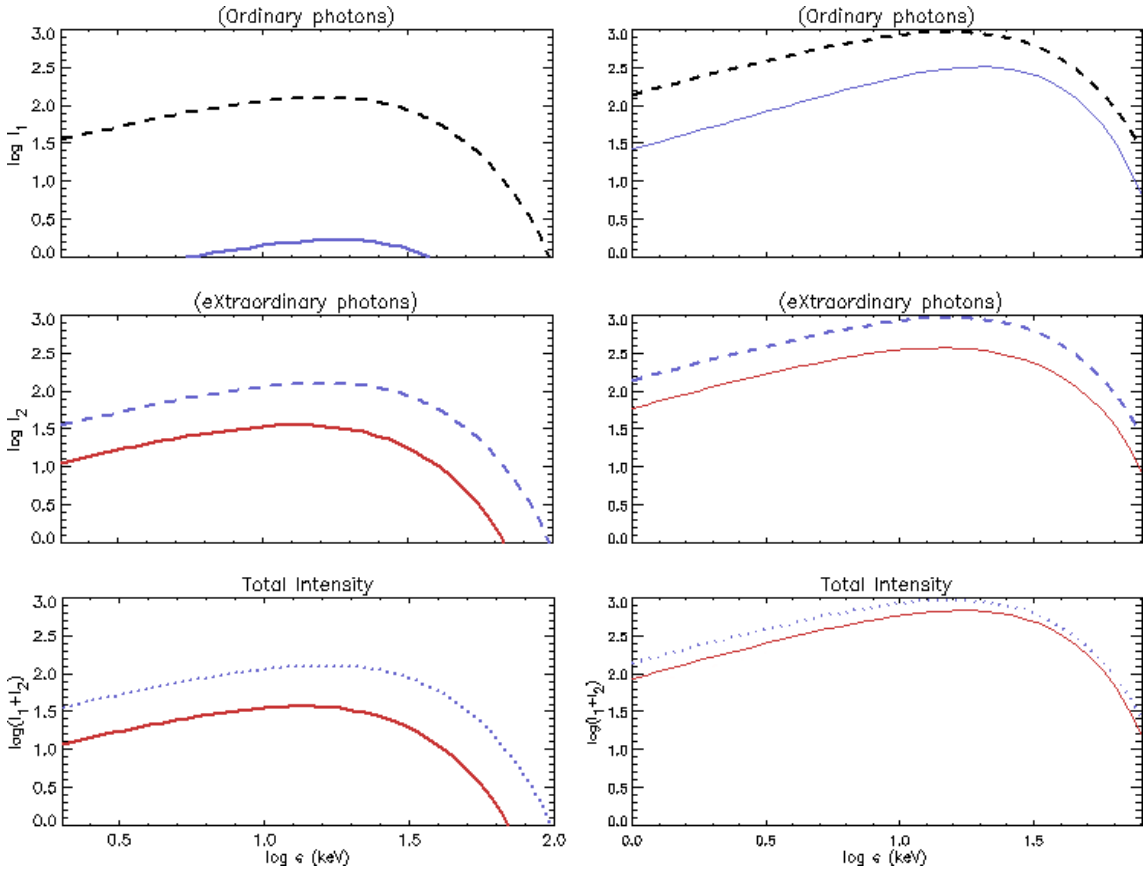

Figure 7.9: Emerging spectra (at $\bar{\tau} = 100$) for ordinary (top row) and extraordinary (middle row) photons, and total emerging spectrum (bottom row) in the case of conservative scattering (left-hand column) and non-conservative scattering (right-hand column), after 100 iterations. The blackbodies at the external temperature $T_{\rm ext} = 8$ keV are also shown (dashed/dotted lines).

(equations 7.10): since the opacity for the X-mode photons is suppressed with respect to that of the O-mode photons by a factor $(B/B_{\rm Q})^{-2}$, the emergent radiation should be formed mainly by extraordinary photons, which escape the fireball very soon, while ordinary ones remain trapped in the magnetosphere by the scatterings onto the fireball particles. In the case of non-conservative scattering, however, while the code seems to reach convergence already after ~ 100 iterations for the extraordinary photons, for the ordinary ones it is not so. This is essentially connected to the poor convergence properties of the $\Lambda-$iteration method. In fact, at each step of the integration process, the code follows the photon over only one mean free path

$$\lambda = \frac{1}{n_{\rm e}\sigma_{\rm T}} \sim \frac{1}{\tau}\,. \tag{7.29}$$

The number of iterations needed to reach the full convergence has to be equal at least to the number of scatterings each photon does on average before leaving the slab; in the assumed hypothesis that $\tau_{\rm max} = 100 \gg 1$, one has

$$N_{\rm iter} \gtrsim N_{\rm scatt} \approx \tau_{\rm max}^2 \simeq 10^4\,. \tag{7.30}$$

Since each iteration takes about 10^3 s (on an Intel Core i7 processor machine), ~ 115 days would be needed to the code, at the present stage of development, to reach the full convergence.

Different solutions have then been tried in order to solve this problem, starting from the different accelerated methods developed to improve the original $\Lambda-$iteration, as for example the "accelerated $\Lambda-$iteration" (Cannon, 1973, see also Varga 1962). This method makes sure to find a suitable approximation of the $\mathbf{\Lambda}$ operator with an easily-invertible matrix $\mathbf{\Lambda}^*$; however, it requires that $\mathbf{\Lambda}$ is simply representable with a matrix, that is not the case of the code at this stage. Another method is the so-called "Ng-acceleration" (Ng, 1974; Buchler & Auer, 1983), that consists in finding an analytical approximation of the solution. This method can be applied only to linear converging problems, while in the case at hand some non-linear terms (such as the stimulated scattering terms) appear in the radiative transfer equation. On a multi-core processor machine, it could also be possible to distribute the single iterations to each core, through suited parallelization utilities, in such a way to reduce the computing time of the entire run[5]. The downside of this method is that parallelized codes should avoid sums (due to the inability of ordinary parallelization utilities to sinchronize the outputs coming from different cores); since the radiative transfer calculations contain several integrals (over the energy and over the angles), a correct parallelization of the code appears not trivial, and the possible gain in computational time would be likely quite modest.

The last tested approach, quite promising in solving the convergence problems of the present version of the code, is considering simulations with a lower optical depth $\tau_{\rm max}$. In fact, in the cases shown above, it is clear that ordinary photons do too many scatterings in the slab with $\tau_{\rm max} = 100$; this would require fine angular and energy grids, that eventually translate in too long computational times, to avoid instabilities.

[5]Normal fortran compilers, in fact, usually work on only one core also in a multi-core processor machine.

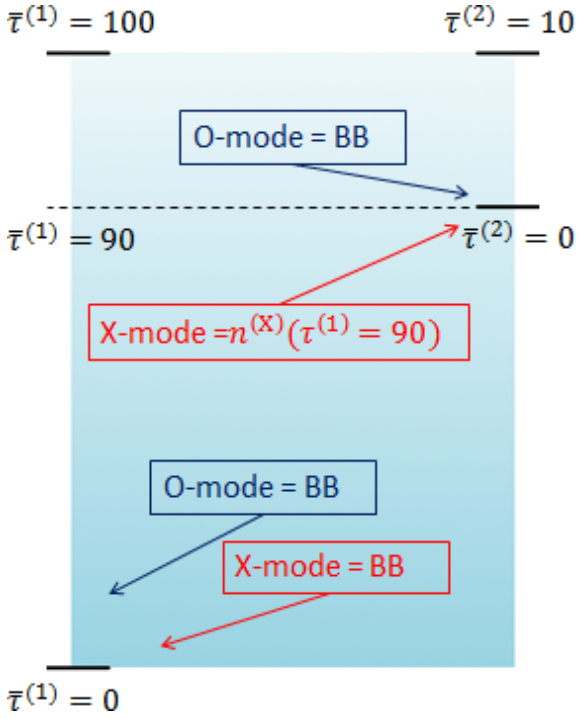

Figure 7.10: Sketch of the "double-run method": as initial conditions, in the first run both $n^{(O)}$ and $n^{(X)}$ have been taken as blackbodies, while in the second run $n^{(X)}$ is set at the value given in output by the first run at $\bar{\tau}^{(1)} = 90$; $n^{(O)}$ is taken as a blackbody also in the second run (see text for details).

On the other hand, if a smaller optical depth is the optimal solution for the O-mode photons, it could be an issue for the X-mode photons, that escape the fireball much earlier than the O-mode ones. For these reasons, the method envisages two successive runs, characterized by $\bar{\tau}^{(1)}_{\rm max} = 100$ and $\bar{\tau}^{(2)}_{\rm max} = 10$, respectively. While the initial conditions for the first run are the same as discussed above, the second run is started taking the output of the first run at $\bar{\tau}^{(1)} = 90$ (corresponding to $\bar{\tau}^{(2)} = 0$) for X-mode photons, and a blackbody for the O-mode ones. This is equivalent to say that ordinary photons are still thermalized at $\bar{\tau}^{(2)} = 0$; the first run output for the O-mode photons is rejected and their evolution is considered only in the second run (for $\bar{\tau}^{(2)} = 0 - 10$), whereas the X-mode photons continue to evolve from the output obtained at the end of the first run. In order to correctly connect the results of the two runs, the temperature has to be adequately re-binned, in such a way that its values at the boundaries of the two integration domains match; after some calculations it results

$$T^{(2)} = T^{(1)}_{\rm max}\left[1 - \frac{\Delta T}{T^{(1)}_{\rm max}}\left(1 - \frac{\bar{\tau}^{(2)}_{\rm max}}{\bar{\tau}^{(1)}_{\rm max}}\right)\right]\left[1 - \frac{\Delta T \bar{\tau}^{(2)}}{T^{(1)}_{\rm max}\bar{\tau}^{(1)}_{\rm max} - \Delta T(\bar{\tau}_{\rm max} - \bar{\tau}_{\rm min})}\right], \qquad (7.31)$$

with $\Delta T = T^{(1)}_{\rm max} - T^{(1)}_{\rm ext}$.

Figure 7.11 shows the behaviors of the fluxes (left-hand column) and the emerging spectra (right-hand column) for non-conservative scattering at the end of the two runs, after 100 iterations of both. It can be clearly seen that reducing the optical depth

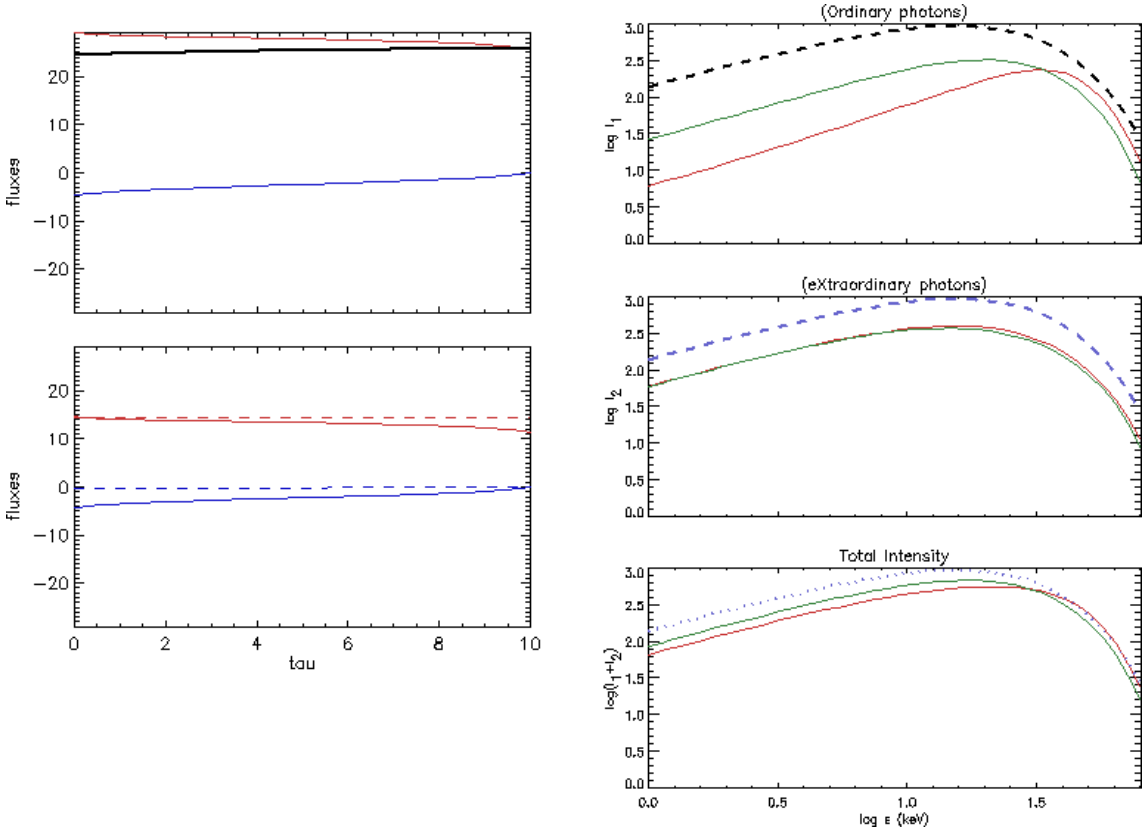

Figure 7.11: Fluxes as functions of the height $\bar{\tau}$ (left-hand column) and emerging spectra (right-hand column) for non-conservative scattering after 100 iterations for both the first ($\bar{\tau}^{(1)}_{\rm max} = 100$) and the second run ($\bar{\tau}^{(2)}_{\rm max} = 10$). In the left-hand column the line style and colors have the same meaning as in Figure 7.8. In the right-hand column the green lines represent the results at the end of the first run, while the red lines those at the end of both the runs; the dashed/dotted lines are the blackbody at the external temperature $T_{\rm ext} = 8$ keV.

remarkably improves the convergence for the ordinary photons. In fact, the total flux (black line in the top-left panel) is nearly constant, with a maximum deviation of $\sim 5\%$ at the higher values of $\bar{\tau}$, and the outward flux for the ordinary photons only (red-solid line in the bottom-left panel) is not anymore flat, at variance with the result shown above (see Figure 7.9). On the other hand, the O-mode photon emerging spectrum (top-right panel) at the end of the two runs (red line) is substantially softer than that at the end of the first run (green line) at lower energies, although it remains anyway too hard at the higher energies; this means that there are still some problems in the integration of the radiative transfer equation for ordinary photons. The fluxes and the spectra for the extraordinary photons are, instead, quite unchanged with respect to the result obtained at the end of the first run only, confirming that the code converges, for X-mode photons, also after the first run. Much in the same way as in the conservative scattering case (shown in the left-hand column of Figure 7.9), the total emerging spectrum (bottom-right panel) is now quite similar to that for the X-mode photons, at least for low energies, whereas it is affected by the excess shown by the O-mode photon emerging spectrum at high energies.

Despite these problems, to be addressed in future developments, these preliminary results allow to exclude, also at this first stage, the possibility that the total emerging spectrum is given by the sum of the O-mode and the X-mode components, as proposed by Israel et al. (2008). Looking at the conservative scattering case (that seems to be not affected by the convergence problems of the non-conservative one), it is more likely that the total spectrum is dominated by X-mode photons only, due to the fact that their opacity is much smaller than that of O-mode photons.

Chapter 8

Conclusions

In this thesis I studied the polarization properties of the emission coming from strongly magnetized, isolated neutron stars. I focused in particular on the persistent and bursting emission from magnetars and radiation emitted from XDINSs, considering the processes that occur in the magnetosphere of the former and the different surface emission models (magnetized atmosphere or a condensed surface) for the latter.

I first dealt with the connection between the intrinsic polarization pattern, i.e. that at the photon emission point predicted by theoretical models, and the polarization signal that one expect to observe at infinity, using a ray-tracing code to derive the polarization observables at different viewing angles χ and ξ (see chapter 3). The effects of geometry, i.e. the rotation of the Stokes parameters which is required when the magnetic field is not constant across the emitting region (see section 2.3.2), and QED (the "vacuum polarization") have been accounted for. In order to make a full exploration of the parameter space possible, I considered the simple case of 100% polarized, blackbody radiation, emitted from a NS with a purely dipolar magnetic field. Also the effects of QED have been treated in a simplified way: only the adiabatic region (where the photon polarization modes are held fixed by the strong stellar magnetic field) and the external region (where the photon electric field is frozen) have been considered, ignoring the transition between the two regimes predicted by the equations governing the evolution of the Stokes parameters. This simplified approach allowed a considerable gain in computational time, without losing significant physical accuracy. On the other hand, I verified that the deviation with respect to the full treatment can be accurately predicted and, in any case, it is not particularly important (see §4.2.2).

The results presented in section 3.3 showed that the observed polarization pattern can be quite different from the intrinsic one; for particular viewing geometries, photons emitted from the star polarized in a certain mode can even be observed as polarized in the other (see e.g. Figure 3.6). The polarization fraction can reduce to zero when the observer LOS is nearly aligned to the magnetic axis (i.e. $\chi \simeq \xi$, see Figure 3.3), as an effect of the maximum non-uniformity of the stellar magnetic field close to the magnetic poles. Moreover, the linear polarization degree strongly depends on the photon energy and the magnetic field intensity: it is larger for high photon energies and magnetic field strength (see Figures 3.3 and 3.5). This is a consequence of the vacuum polarization effects: since the adiabatic radius $r_{\rm a}$ depends on $E^{1/5}B_{\rm pol}^{2/5}$ (see equation 2.23), high photon energies and strong magnetic fields result in wider adiabatic regions; hence,

larger polarization degrees will be observed the more point-like the star appears at an ideal observer set at the adiabatic radius $r_{\rm a}$. On the contrary, the polarization angle shows an oscillating behavior as a function of the star rotational phase which does not depend on the photon energy and magnetic field strength, but it changes only as the viewing angles vary. This can in principle allow to understand when radiation that is observed to be unpolarized, has been actually emitted as polarized at the surface (see Figures 3.3 and 3.5). The oscillation mean value depends on the polarization state of the majority of the collected photons: ordinary and extraordinary seed photons produce distributions oscillating around two different mean values, shifted by 90° (see Figure 3.4). However, the mean values depend also on the orientation of the polarimeter axes in the plane orthogonal to the LOS; as a consequence, a measurement of the polarization angle alone fails in telling which is the prevailing polarization mode, since a certain observed configuration can in principle refer to both extraordinary photons or ordinary photons with the polarimeter frame rotated by 90°. Removing the degeneracy would be feasible only if the angle ψ between the reference axis u of the polarimeter and the projection of the star spin axis in the plane orthogonal to the LOS (the X-axis in Figure 3.1a) is known. On the other hand, the oscillation amplitude of the polarization angle behavior is related to the viewing geometry (see Figure 3.3 and Figure 3.6, top-right panel): $\chi_{\rm p}$ sweeps the entire range $[0°, 180°]$ when the region close to the magnetic pole is always in view, while the swing gets smaller for values of χ and ξ such that the polar region enters into view only at certain rotational phases. Finally, the polarization angle is also sensitive to the topology of the stellar magnetic field; in fact the introduction of a global twist introduces an asymmetry in the behavior as a function of the rotational phase, that is more pronounced the larger the twist angle (see Fernàndez & Davis, 2011; Taverna et al., 2015); the twist shows, instead, very little effects on the polarization fraction (see Figure 3.8).

I then investigated the polarization of X-ray persistent radiation from magnetars (see chapter 4), within the framework of the twisted magnetosphere model (see §1.4.2), which has been successfully applied to reproduce the soft X-ray spectra of several magnetar candidates (see Nobili, Turolla & Zane, 2008a; Zane et al., 2009). While retaining some simplifications (globally twisted magnetosphere and unidirectional flow of charged particles along the closed field lines), the Monte Carlo code developed to simulate the observed polarization response properly accounts for the effects of QED, RCS and Stokes parameter rotation. Due to the ultra-strong magnetic fields inferred in magnetars, also in this case the emitted radiation has been assumed 100% polarized in the extraordinary mode; nevertheless, the code can deal with arbitrary polarization patterns, as for example considering larger fractions of ordinary photons from the regions heated by the returning currents (Beloborodov & Thompson, 2007). Unlike the calculation carried out in chapter 3, QED effects are fully taken into account integrating equations (2.38); anyway, the simplified approach used in chapter 3 can be implemented also in this code, not including the module that contains the numerical integration of the Stokes parameters.

Results show that the expected linear degree of polarization is very high in an extended range of energies, making magnetars the ideal candidates for X-ray polarization measumrements. On the other hand, circular polarization fraction (that in case of highly magnetized INSs can originate only due to vacuum polarization effects) is

absolutely negligible, the only significant contribution ($\lesssim 3\%$) arising because of the unidirectional flow approximation (see Figure 4.3). Both phase-averaged and phase-resolved simulations confirm that the polarization observables are very sensitive to the magnetospheric parameters (i.e. the twist angle $\Delta\phi_{\mathrm{N-S}}$ and the electron bulk velocity β_{b}). Spectral analysis alone can not give a complete information, due to an inherent degeneracy in the RCS model: different parameter values can produce, in fact, the same spectrum (see Figure 4.4, left-hand column). In these cases, studying the behavior of the polarization observables can indeed remove the ambiguity, allowing to discriminate between the different cases. The validity of the simplifying approximation for computing vacuum polarization effects (i.e. considering only the adiabatic and the external regions) has been also investigated, proving that minimal deviations affect the polarization observables when the integration of the equation system (2.38) is turned off, provided that the adiabatic radius r_{a} is not too close to the star surface (see Figure 4.5).

Polarization measurements promise to be crucial also in investigating the surface radiation from thermal emitting, highly magnetized INSs like XDINSs, as pointed out in chapter 5 for the particular case of RX J1856.5-3754. The magnetized atmosphere and the condensed surface emission models produce quite different intrinsic polarization patterns, so that it is reasonable to expect large differences also in the signal observed at infinity (after the addition of the geometrical and QED effects). Restricting to values of χ and ξ that are compatible with the measured X-ray pulsed fraction ($\sim 1\%$, Tiengo & Mereghetti, 2007), Figure 5.5 shows that the expected phase-averaged degree of polarization is normally quite large (close to 100%) in the case of the magnetized atmosphere, while it is much reduced for the condensed surface (both in the free-ions and fixed-ions limits), where the value attained is $\sim 40\%$. The situation changes if the LOS and the star rotation axis are nearly aligned (i.e. $\chi \simeq 0^{\circ}$), when the average over the rotational phase of the polarization fraction produces very low values for all the emission models. From the plots in Figure 5.5 it can be also seen that polarization of optical radiation coming from XDINSs can be considerable; however, while in the case of atmospheric emission the polarization in the optical band is expected to be lower than that in the X-rays, the contrary happens for condensed surface emission. Also the behavior of the observed phase-averaged polarization angle is different between the two emission models. A combined measurement of the polarization observables (in the optical and in the X-rays) can be crucial in disambiguating whether the observed radiation comes from a gaseous atmopshere or a condensed surface.

Due to the recent developments in X-ray polarimetric techniques, and since the observed polarization degree is expected to be larger at higher photon energies, I discussed the feasibility of X-ray polarization measurements, simulating, through a suitable Monte Carlo code, a 1 Ms observation in the $2-6$ keV energy range of the bright AXP 1 RXS J170849.0-400910 with XIPE, a medium X-ray polarimetry mission recently selected for phase A of the ESA M4 program (see chapter 6). Results shown in Figures 6.3 and 6.5 (see also Table 6.1) confirm that X-ray polarization measurements allow to extract the values of physical and geometrical parameters at high confidence level. This has been possible by fitting simultaneously the simulated observations for the polarization observables and the light curve with a large set of theoretical models, stored in a specific archive. Moreover, this more in-depth analysis also allows to

distinguish between different configurations in which photon spectra are very similar (see Figure 6.4), therefore removing possible degeneracies. Polarization measurements have been also proven to be rather sensitive to the position of the adiabatic radius $r_{\rm a}$, through specific simulations in which the "observed" data have been obtained from theoretical models in which equations (2.38) were integrated or not (see Figure 6.6). Since, once the energy band is fixed, the adiabatic radius depend only on the magnetic field strength (see equation 2.23), this means that X-ray polarimetry could be employed to indirectly probe the presence of strong magnetic fields around magnetars.

Finally, in chapter 7 I reported my preliminary work about the modeling of magnetar burst emission, based on the trapped fireball model and on the propagation of ordinary and extraordinary photons through a magnetized plasma. Although the FORTRAN code still has some numerical problems, to be addressed in future developments, the results obtained so far suggest that the spectrum of the radiation emitted in these events is made mainly by the extraordinary photons; as a consequence magnetar burst emission should have indeed a strong degree of polarization. In any case, reconstructing the polarization pattern of magnetar burst emission could corroborate the current theoretical model and help in understanding the underlying emission mechanisms, as well as the magnetosphere structure. Short bursts and intermediate flares, however, are unfortunately quite sporadic and extremely short, and it is rather unlikely that an instrument like XIPE is pointed towards a burst emitting source at the time in which the burst appears. The hope is, then, to observe batches of these events, as in the case of the "burst forest" emitted by SGR 1900+14 in 2006 March; in this way the increase in collected counts can compensate for the short durations.

This work further demonstrates that polarization measurements, ideally complementing spectral and timing measures, can indeed provide invaluable insight on the physics of highly magnetized isolated neutron stars. This is of particular relevance in relation to the recent X-ray polarimetry mission proposals, the sensitivity of which appears today perfectly adequate to successfully investigate physical processes in the presence of strong magnetic fields.

Bibliography

Adler S. L., 1971, Ann. Phys., 67, 599

Albano A., Turolla R., Israel G. L., Zane S., Nobili L., Stella L., 2010, ApJ, 722, 788

Alexander S., Mèszàros P., Bussard R., 1989, ApJ, 342, 928

Baade W., Zwicky F., 1934, Proc. Nat. Acad. Sci., 20, 254

Bellazzini R. et al., 2006, Nucl. Instrum. Methods Phys. Res. A, 566, 552

Bellazzini R. et al., 2007, Nucl. Instrum. Methods Phys. Res. A, 579, 853

Bellazzini R., Costa E., Matt G., Tagliaferri G., 2010, in Bellazzini R., Costa E., Matt G., Tagliaferri G., eds, X-ray Polarimetry: A New Window in Astrophysics. Cambridge Univ. Press, Cambridge

Bellazzini R., Muleri F., 2010, Nucl. Instrum. Methods Phys. Res. A, 623, 766

Bellazzini R., Spandre G., 2010, in Bellazzini R., Costa E., Matt G., Tagliaferri G., eds, X-ray Polarimetry: A New Window in Astrophysics. Cambridge Univ. Press, Cambridge, p. 19

Bellazzini R. et al., 2013, Nucl. Instrum. Methods Phys. Res. A, 720, 173

Beloborodov A. M., 2009, ApJ, 703, 1044

Beloborodov A. M., Thompson C., 2007, ApJ, 657, 967

Beloborodov A. M., 2013, ApJ, 762, 13

Black J. K., Baker R. G., Deines-Jones P., Hill J. E., Jahoda K., 2007, Nucl. Instrum. Methods Phys. Res. A, 581, 755

Bogomazov A. I., Popov S. B., 2009, MNRAS, 53, 325

Borghese A., Rea N., Coti Zelati F., Tiengo A., Turolla R., 2015, ApJ, 807, L20

Braithwaite J., 2009, MNRAS, 397, 763

Brinkmann W., 1980, A&A, 82, 352

Brown E. F., Bildsten L., Rutledge R. E., 1998, ApJ, 504, L95

Buchler J., Auer L., 1983, Proceedings of the 2nd International Conference and Workshop on the Radiative Properties of Hot Dense Matter, (ed. J. Davis). World Scientific, Singapore

Burwitz V., Zavlin V. E., Neuhäuser R., Predehl P., Trümper J., Brinkman A. C., 2001, A&A, 379, L35

Burwitz V., Haberl F., Neuhäuser R., Predehl P., Trümper J., Zavlin V. E., 2003, A&A, 399, 1109

Camero-Arranz A. et al., 2013, MNRAS, 429, 2493

Camilo F., Ransom F. M., Halpern J. P. et al., 2006, Nature, 442, 892

Campana S., Rea N., Israel G. L., Turolla R., Zane S., 2007, A&A, 463, 1047

Cannon C., 1973, J.Q.S.R.T., 13, 627

Clark J. S., Ritchie B. W., Najarro F., Langer N., Negueruela I., 2014, A&A, 565, A90

Connors P. A., Stark, R. F., 1977, Nature, 269, 128

Costa E., Soffitta P., Bellazzini R., Brez A., Lumb N., Spandre G., 2001, Nature, 411, 662

Costa E. et al., 2010, Exp. Astron., 28, 137

Dean A. J. et al., 2008, Science, 321, 1183

de Luca A., 2008, Vol. 983 of AIP Conf. Proc. pp 311-319

Dovčiak M., Muleri F., Goosmann R. W., Karas V., Matt G., 2011, ApJ, 731, 75

Duncan R. C., Thompson C., 1992, ApJ, 392, L9

Durant M., van Kerkwijk M. H., 2006, ApJ, 650, 1070

Fabiani S., Campana R., Costa E., Del Monte E., Muleri F., Rubini A., Soffitta P., 2013, Astroparticle Physics, 44, 91

Fernàndez R., Davis S. W., 2011, ApJ, 730, 131

Fernàndez R., Thompson C., 2007, ApJ, 660, 615

Feroci M., Caliandro G. A., Massaro E., Mereghetti S., Woods P. M., 2004, ApJ, 612, 408

Ferrario L., Wickramasinghe D., 2008, MNRAS, 389, L66

Flowers E., Ruderman M. A., 1977, ApJ, 215, 302

Ginzburg V. L., 1970, The propagation of Electromagnetic Waves in Plasmas (2nd ed.). Pergamomn, London

Gnedin Yu. N., Pavlov G. G., 1974, Soviet Phys.-JETP Lett., 38, 903

Goldreich P., Julian W. H., 1969, MNRAS, 389, 157

Gonzàlez Caniulef D., Zane S., Taverna R., Turolla R., Wu K., 2016, MNRAS, submitted

Götz D., Mereghetti S., Mirabel I. F., Hurley K., 2004, A&A, 417, L45

Götz D., Mereghetti S., Tiengo A., Esposito P., 2006, A&A, 449, L31

Haberl F., 2007, Ap&SS, 308, 181

Halpern J. P., Gotthelf E. V., 2010, ApJ, 709, 436

Harding A. K., 2013, Front. Phys., 8, 679

Harding A. K., Daugherty J. K., 1991, ApJ, 374, 687

Harding A. K., Lai D., 2006, Rep. Prog. Phys., 69, 2631

Heisenberg W., 1936, Zeitschrift für Physik, 101, 533

Helfand D. J. et al., 2007, ApJ, 662, 1198

Herold H., 1979, Phys. Rev. D, 19, 2868

Hewish A., Bell S. J., Pilkington J. D. H., Scott P. F., Collins R. A., 1968, Nature, 217, 709

Heyl J. S., Shaviv N. J., 2002, Phys. Rev. D, 66, 023002

Heyl J. S., Shaviv N. J., Lloyd D., 2003, MNRAS, 342, 134

Ho W. C. G., 2011, MNRAS, 414, 2567

Ho W. C. G., Chang P., Kaplan D. L., Mori K., Potekhin A., van Adelsbserg M., 2007, Advances in Space Research, 2007, 1432

Ho W. C. G., Henike C. O., 2009, Nature, 62, 71

Ho W. C. G., Lai D., 2003, MNRAS, 338, 233

Ho W. C. G., Lai D., 2004, ApJ, 607, 420

Ho W. C. G., Potekhin A. Y., Chabrier G., 2008, ApJS, 178, 102

Hughes J. P., Long K. S., Novick R., 1984, ApJ, 280, 255

Hulleman F., van Kerkwijk M. H., Kulkarni S. R., 2000, Nature, 408, 689

Hulleman F., van Kerkwijk M. H., Kulkarni S. R., 2004, A&A, 416, 1037

Hurley K. et al., 1999, Nature, 397, 41

Hurley K. et al., 2005, Nature, 434, 1098

Ishihara H., Takahashi M., Tomimatsu A., 1988, Phys. Rev. D., 38, 472

Israel G. L. et al., 2005, A&A, 438, L1

Israel G. L. et al., 2008, ApJ, 685, 1114

Jahoda K. M., Kouveliotou C., Kallman T. R. and the PRAXyS collaboration, 2015, in AAS Meeting, #225, #338.40

Kaplan D. L., Kamble A., van Kerkwijk M. H., Ho W. C. G., 2011, ApJ, 736, 117

Kaplan D. L., van Kerkwijk M. H., 2006, American Astronomical Society, HEAD meeting #9, #4.02. Bulletin of the American Astronomical Society, 38, 346

Kaspi V. M., 2010, PNAS, 107, 7147

Keane E. F., McLaughlin M. A., 2011, Bull. Astr. Soc. India, 39, 1-20

Klein J. J., Nigam B. P., 1964, Phys. Rev., 135, 1279

Kojima Y., Kato Y. E., ApJ, 728, 75

Kondratiev V. I., McLaughlin M. A., Lorimer D. R., Burgay M., Possenti A., Turolla R., Popov S. B., Zane S., 2009, ApJ, 702, 692

Lai D., 2001, Rev. Mod. Phys., 73, 629

Lai D., Ho W. C. G., van Adelsberg M., Wang C., Heyl J. S., 2010, X-ray Polarimetry: A New Window in Astrophysics. Cambridge Univ. Press, Cambridge

Lai D., Salpeter E. E., 1997, ApJ, 491, 270

Landau L. D., 1930, Z. Phys., 64, 629

Lloyd D. A., 2003, arXiv:astro-ph/0303561

Lloyd D. A., Hernquist L., Heyl J. S., 2003, ApJ, 593, 1024

Lyne A. G., Manchester R. N., 1988, MNRAS, 234, 477

Manchester R. N., Taylor, J. H., 1977, Pulsars. Freeman, San Francisco

Mazets E. P., Golenetskii S. V., Ilinskii V. N., Aptekar R. L., Guryan I. A., 1979, Nature, 282, 587

Mazets E. P., Golenetskii S. V., Guryan I. A., Ilinskii V. N., 1982, Ap&SS, 84, 173

McLaughlin M. A. et al., 2007, ApJ, 670, 1307

Medin Z., Lai D., 2006, Phys. Rev. A., 74, 062508

Medin Z., Lai D., 2007, MNRAS, 382, 1833

Mereghetti S., 2008, A&A Rev., 15, 225

Mereghetti S., 2010, in Astrophysics and Space Science Proceedings (pp 345-363). Springer, Berlin, Heidelberg

Mèszàros P., 1992, High-Energy Radiation from Magnetized Neutron Stars. University of Chicago Press, Chicago, IL

Mèszàros P., Pavlov G. G., Shibanov Y. A., 1989, ApJ, 337, 1989

Miller J., McLaughlin M., Rea N., Keane E., Lyne A., Kramer M., Manchester R., Lazaridis K., 2011, AIP Conf. Proc., 1357, 161

Motch C., Zavlin V. E., Haberl F., 2003, A&A 408, 323

Muleri F. et al., 2008, Nucl. Instrum. Methods Phys. Res. A, 584, 149

Muleri F. et al., 2010, Nucl. Instrum. Methods Phys. Res. A, 620, 285

Muleri F. et al., 2012, Proc. of SPIE, Vol. 8443, 84430L-3

Muleri F., 2014, ApJ, 782, 28

Muno M. P., Clark J. S., Crowther P. A., 2006, ApJ, 636, L41

Ng K., 1974, J. Chem. Phys., 61, 2680

Nobili L., Turolla R., Zane S., 2008a, MNRAS, 386, 1527

Nobili L., Turolla R., Zane S., 2008b, MNRAS, 389, 989

Nobili L., Turolla R., Zane S., 2011, Advances in Space Research, 2011, 1035

Olive J. F. et al., 2004, ApJ, 616, 1148

Pacini F., 1968, Nature, 219, 145

Paczynski B., 1992, Acta Astronomica, 42, 145

Paerels F. et al., 2001, A&A, 365, L298

Page D., 1995, ApJ, 442, 273

Page D., Sarmiento A., 1996, ApJ, 473, 1067

Pavan L., Turolla R., Zane S., Nobili L., 2009, MNRAS, 395, 753

Pavlov G. G., Zavlin V. E., 2000, ApJ, 529, 1011

Pèrez-Azorìn J. F., Miralles J. A., Pons J. A., 2005, A&A, 433, 275

Perna R., Hernquist H., Narayan R., 2000, ApJ, 541, 344

Pomraning G. C., 1973, The equations of radiation hydrodynamics, Dover publications inc. Mineola, New York

Popov S. B., Colpi M., Prokhorov M. E., Treves A., Turolla R., 2003, A&A, 406, 111

Popov S. B., Prokhorov M. E., 2006, MNRAS, 367, 732

Posselt B., Popov S. B., Haberl F., Trümper J., Turolla R., Neuhäuser R., 2008, A&A, 482, 617

Potekhin A. Y., 2014, Physics Uspekhi, 57, 735

Potekhin A. Y., Chabrier G., 2004, ApJ, 600, 317

Potekhin A. Y., Lai D., Chabrier G., Ho W. C. G., 2004, ApJ, 612, 1034

Potekhin A. Y., Suleimanov V. F., van Adelsberg M., Werner K., 2012, A&A 546, A121

Rajagopal M., Romani R. W., 1996, ApJ, 461, 327

Rea N., Oosterbroek T., Zane S., Turolla R., Méndez M., Israel G. L., Stella L., Haberl F., 2005, MNRAS, 361, 710

Rea N. et al., 2009, ApJ, 703, L41

Rea N., Esposito P., 2011, in Torres D. F., Rea N., eds, Astrophysics and Space Science Proc., High-Energy Emission from Pulsars and Their Systems. Springer-Verlag, Berlin, p. 247

Rea N., Pons J. A., Torres D. F., Turolla R., 2012, ApJ, 748, L12

Reisenegger A., Goldreich P., 1992, ApJ, 395, 240

Rybicki, G. B., Lightman, A. P., 2004, Radiative Processes in Astrophysics (2nd ed.; Weinheim: Wiley)

Sartore N., Tiengo A., Mereghetti S., De Luca A., Turolla R., Haberl F., 2012, A&A 541, A66

Soffitta P. et al., 2013, Nucl. Instrum. Methods Phys. Res. A, 700, 99

Stark R. F., Connors, P. A., 1977, Nature, 266, 429

Suleimanov V., Potekhin A. Y., Werner K., 2009, A&A, 500, 891

Tagliaferri G., Hornstrup A., Huovelin J., Reglero V., Romaine S., Rozanska A., Santangelo A., Stewart G., 2012, Exp. Astron., 34, 463

Taverna R., Muleri F., Turolla R., Soffitta P., Fabiani S., Nobili L., 2014, MNRAS, 438, 1686

Taverna R., Turolla R., Gonzalez Caniulef D., Zane S., Muleri F., Soffitta P., 2015, MNRAS, 454, 3254

Tayler R. J., 1973, MNRAS, 161, 365

Tendulkar S. P. et al., 2015, ApJ, 808, 32

Thompson C., Beloborodov A., 2005, ApJ, 634, 565

Thompson C., Duncan R. C., 1993, ApJ, 408, 194

Thompson C., Duncan R. C., 1995, MNRAS, 275, 255

Thompson C., Duncan R. C., 2001, ApJ, 561, 980

Thompson C., Lyutikov M., Kulkarni S. R., 2002, ApJ, 574, 332

Tiengo A., Esposito P., Mereghetti S., Turolla R., Nobili L., Gastaldello F., Götz D., Israel G. L., Rea N., Stella L., Zane S., Bignami G. F., 2013, Nature, 500, 312

Tiengo A., Mereghetti S., 2007, ApJ, 657, L101

Torres-Forné A., Cerdá-Durán P., Pons J. A., Font J. A., 2015, arXiv:1511.03823

Turolla R., 2009, in Astrophysics and Space Science Library, Neutron Stars and Pulsars, Vol. 357., W. Becker ed., Springer, Berlin, p. 141

Turolla R., Zane S., Drake J. J., 2004, ApJ, 603, 265

Turolla R., Zane S., Watts A. L., 2015, Rep. Prog. Phys., 78, 11

Turolla R., Esposito P., 2013, Int. J. Mod. Phys. D, 22, 133024

van Adelsberg M., Lai D., 2006, MNRAS, 373, 1495

van Adelsberg M., Lai D., Potekhin A. Y., Arras P., 2005, ApJ, 628, 902

van Assche W., Tayler R. J., Goossens M., 1981, A&A, 109, 166

van Kerkwijk M. H., Kaplan D. L., 2008, ApJ, 673, L163

van Kerkwijk M. H., Kulkarni S. R., 2001, A&A, 378, 986

Varga R. S., 1962, 'Matrix iterative analysis'. In Prentice Hall Series in Automatic Computations, Englewood Cliffs: Prentice-Hall

Viganò D., Pons J. A., 2012, MNRAS, 425, 2487

Vink J., Kuiper L., 2006, MNRAS, 370, L14

Vink J., 2008, AdSR, 41, 503

Wagner S. J., Seifert W., 2000, in Kramer M., Wex N., Wielebinski R., eds, ASP Conference Series, Vol. 202, Pulsar Astronomy – 2000 and Beyond Astron. Soc. Pac., San Francisco, 315

Walker M., Penrose R., 1970, Commun. Math. Phys., 18, 265

Weisskopf M. C., Silver E. H., Kastenbaum K. S., Long K. S., Novick R., Wolff R. S., 1978, ApJ, 220, L117

Weisskopf M. C. et al., 2013, Proc. SPIE, 8859, 885908

Wolfson R., 1995, ApJ, 443, 810

Yang Y. P., Zhang B., 2015, ApJ, 815, 45

Zane S., Turolla R., Stella A., Treves A., 2001, ApJ, 560, 384

Zane S., Haberl F., Cropper M., Zavlin V. E., Lumb D., Sembay S., Motch C., 2002, MNRAS, 334, 345

Zane S., Turolla R., Drake J. J., 2002, in High resolution X-ray spectroscopy with XMM-Newton and Chandra, MSSL, ed. G. Branduardi-Raymont (University College London, Holmbury St. Mary, Dorking, Surrey, UK), #51

Zane S., Rea N., Turolla R., Nobili L., 2009, MNRAS, 398, 1403

Zane S., Turolla R., 2006, MNRAS, 366, 727

Zavlin V. E., 2009, in Astrophysics and Space Science Library, Neutron Stars and Pulsars, Vol. 357., W. Becker ed., Springer, Berlin, p. 181